HZB Helmholtz Zentrum Berlin

SCHRIFTENREIHE DES HZB · EXAMENSARBEITEN

Clustering and Precipitation in Al-Mg-Si Alloys

Zeqin Liang

Dissertation

Institut für Angewandte Materialforschung

November 2012

HZB–B 38

ISSN 1868-5781

doi: http://dx.doi.org/10.5442/d0032

Helmholtz-Zentrum Berlin für Materialien und Energie · Hahn-Meitner-Platz 1 · D-14109 Berlin · Telefon +49 30 8062 0 · Telefax +49 30 8062 42181 · www.helmholtz-berlin.de

Clustering and Precipitation in Al-Mg-Si Alloys

vorgelegt von

Master of Engineering

Zeqin Liang

aus Zhaoqing, V.R. China

von der Fakultät III − Prozesswissenschaften
der Technischen Universität Berlin
zur Erlangung des akademischen Grades

Doktor der Ingenieurwissenschaften

-Dr.-Ing.-

genehmigte Dissertation

angefertigt am Helmholtz-Zentrum Berlin für Materialien und Energie

Institut für Angewandte Materialforschung

Promotionsausschuss:

Vorsitzender: Prof. Dr. Walter Reimers
Gutachter: Prof. Dr. John Banhart
Gutachter: Prof. Dr. Günter Gottstein

Tag der wissenschaftlichen Aussprache: 1. 11. 2012

Berlin, 2012

D83

献给我挚爱的爸爸妈妈

Abstract

The influence of temperature history on clustering and precipitation is studied. Al-0.4 wt.% Mg-1.0 wt.% Si alloy with a very low level of impurities and Al-0.4 wt.% Mg-1.0 wt.% Si with 0.25 wt.% Fe and 0.08 wt.% Mn are the main alloys in order to understand the mechanism and kinetics of clustering and precipitation and the influence of intermetallics. Other alloys with additions of 0.01 wt.% Cr or 0.04 wt.% Cu are also used to elucidate the role of small additional elements on clustering and precipitation.

The main findings of this work are:

Two main processes occur during clustering at room temperature. During the first, small clusters form by diffusion of quenched-in vacancy and solute atoms. As the solute concentration in the matrix is reduced, vacancies are then trapped by the clusters. During the second process, coagulation of existing clusters occurs and big clusters form.

Upon natural ageing, the number density of the precipitates formed during AA decreases while their size increases. The main reason causing a negative effect on subsequent artificial ageing is the formation of smaller clusters which lower the solute concentration in the matrix and capture vacancies.

The presence of intermetallics stimulates recrystallisation and finer grains can be obtained after solutionising. However, the Fe-rich intermetallics do not completely dissolve during solutionising, and lower the Si concentration in the matrix, thus reducing the volume fraction of both clusters and precipitates.

Cr addition has no direct influence on clustering and precipitation, but Cu hinders the first clustering process and therefore the negative strength response by natural ageing is reduced. Cu also influences the precipitation sequence because more kinds of precipitates are formed.

This page intentionally left blank

Declaration

Ich erkläre an Eides Statt, dass die vorliegende Dissertation in allen Teilen von mir selbständig angefertigt wurde und die benutzten Hilfsmittel vollständig angegeben worden sind.

This page intentionally left blank

Acknowledgements

I would like to thank Prof. John Banhart for giving me this opportunity to pursue my PhD in Helmholtz Centre Berlin and his valuable suggestions on this work. In particular, I would like to thank his teaching on how to keep a logical and scientific way to analyse all the experimental and simulation results. I am grateful to Dr. Cynthia Chang. She has given me supports in experiments, discussion and thesis writing during my PhD. I would also like to thank her training me to keep persistence to the goal that I am seeking.

I would like to give my many thanks to Dr. Nelia Wanderka and Dr. Markus Wollgarten for their training on the TEM and its analysis. My many thanks come to Holger Kropf for his help on the SEM section and his great suggestion on using BSE and SE at the same time to show different contrasts which can identify the different phases easily. The helping hands from Claudia Leistner and Christiane Förster guarantees the quality of the samples before all microstructure measurements, which I am very grateful to. I would also like to thank Dr Christian Abromeit. Without his support and suggestions, the simulation part in this work is impossible to be achieved. I would also like to thank Dr. Nicolai Lazarev for his suggestions on the statistic approach for the simulation. For the simulation part, I would like also to thank my friend Yucheng Wang for giving me suggestion on using link list for cluster identification. Special thank is due to the help on Positron Lifetime Measurement done by Dr. Matthew Lay. His suggestion and discussion on the lifetime analysis is very helpful to this work. I would also like to thank Julian Kühn, Meng Liu, Eric Schmidt and Yong Yan as friends and teammates on this project. We have had a wonderful time together, doing experiments, writing program, discussing, doing sports and dancing and so on and so on! Thanks to Christiane Ciceron for helping me with all the paper work and organization. Also thanks to Jörg Bajorat for solving all my computer problems.

I greatly acknowledge Hydro Aluminium Bonn for their financial support for my PhD and their effort to run this project. I give my special thanks to Prof. Jürgen Hirsch for his supervision from the industrial site. His great effort on bringing the scientific knowledge to the industry shows an excellent example to me! I owe my many thanks also to Dr. Henk-Jan Brinkman for his management on this project. Moreover, I would like to thank Dr. Carmen Schäfer and Prof. Olaf Engler for their scientific discussion and also help on grain size measurement and micro probe test.

Last but not least, I would like to show my gratitude to my parents Xingguang Liang and Xiuqiu Li and also my wife Ying Liang. All of their supports in my life are priceless. 爸爸，妈妈，妻子，我爱你们，你们是我的全部！

List of Abbreviations

AA	Artificial Ageing
BF	Bright-Field
BIW	Body-In-White
BSE	Backscattered Electron
DFZ	Dispersoid-Free Zone
DSC	Differential Scanning Calormetry
EELS	Electron Energy Loss Spectroscopy
EDX	Energy Dispersive X-ray spectrometry
EHT	Electron High Tension
FWHM	Full Width at Half Maximum
HRTEM	High Resolution Transmission Electron Microscopy
JMAK	Johnson–Mehl–Avrami–Kolmogorov
KMC	Kinetic Monte Carlo
LS	Longitudinal Section
MCS	Monte Carlo Step
NA	Natural Ageing
ND	Normal Direction
NNB	Nearest Neighbour
OES	Optical Emission Spectrometry
PA	Pre Ageing
PALS	Position Annihilation Lifetime Spectrum
PB	Paint Baking
PFZ	Precipitate-Free Zone
PSN	Particle Stimulated Nucleation
RD	Rolling Direction
RT	Room Temperature
SE	Secondary Electrons
SEM	Scanning Electron Microscopy
SHT	Solution Heat Treatment
SSSS	Super-Saturated Solid Solution
TAP	Tomographic Atom Probe
TEM	Transmission Electron Microscopy

This page intentionally left blank

Content

1. Introduction

6xxx series Al-Mg-Si alloys are widely used as body panels for the substitution of steel in the automotive industry in order to reduce the weight of cars and their energy consumption. In practice, alloys are stored at room temperature (RT) or are naturally aged (NA) between annealing and paint baking (PB). In most cases, alloys after NA have slower hardening response and reach a lower strength after PB, which is called the negative strength response. This is due to clusters formed during NA. Understanding the mechanism of clustering and the reason causing the negative strength response is essential. The study of clustering is difficult, as the contrast from clusters is too low to be observed by conventional microscopy techniques. Also, recent investigations using various experimental techniques shows that the clustering process is fast and goes through different stages already within the first few hours of NA. On the other hand, additional alloying elements apart from Mg and Si are often present in commercial alloys, either as impurities or added intentionally such as grain and intermetallics refiners. Whether these additional alloying elements influence the clustering and the precipitation behaviour is still not fully understood.

In this work, high purity ternary Al-Mg-Si alloys and alloys with different additional elements (Fe, Mn, Cu and Cr) are studied. The aim is (1) to understand the mechanism of clustering and its influence on further precipitation and (2) to investigate the effect of additional elements on the recrystallisation, intermetallics formation, clustering and precipitation. Different clustering stages during NA are observed by using a variety of experimental methods. Kinetic Monte Carlo simulation (KMC) based on with the vacancy diffusion model is performed to study the mechanism of the clustering process. After understanding the mechanism, the kinetic model is then applied to obtain kinetic parameters for different processes involved in clustering. Using such kinetic parameters the evolution of the volume fraction of clustering at different temperatures and time can be fully described. The kinetic model is further applied to the formation of precipitate in alloys with and without prior NA. A difference in the kinetic parameters is found. The evolution of the volume fraction simulated by using the parameters agrees with the experimental results. The negative effect caused by clustering during NA is explained.

2. Literature Survey

2.1. Aluminium Alloys

Aluminium is the third most common element on earth and possesses a face centred cubic (fcc) structure when it is in metal form [1]. Though Al is abundant it does not exist in the pure form but most of the time binds with other elements forming compounds. The separation method of Al with its compounds was first introduced in 1825 by the Danish scientist Oersted [2]. First aluminium chloride was treated with potassium amalgam, followed by the removal of mercury by distillation [2]. The first time producing Al on an industrial scale was in 1854 by reducing Al-chloride with sodium by Henri Etienne Sainte-Claire Deville [2]. The high price of sodium makes the cost of Al production extremely high and Al hence at that time was a precious metal. In 1886, Hall and Heroult developed a new method for producing Al by electrolysis of molten alumina in the United States and in France. In 1889, Bayer paved a way to modern industrial production by extracting pure alumina from bauxite [2].

Table 2.1. Designation system for aluminium alloys [3].

Wrought alloys		Casting alloys	
Designation	Principal alloying elements	Designation	Principal alloying elements
1xxx	99.000% Minimum Aluminium	1xx.x	99.000% minimum Aluminum
2xxx	Cu	2xx.x	Cu
3xxx	Mn	3xx.x	Si + Cu or Si + Mg
4xxx	Si	4xx.x	Si
5xxx	Mg	5xx.x	Mg
6xxx	Mg + Si	6xx.x	not used
7xxx	Zn + Mg	7xx.x	Mg + Zn
8xxx	Other elements	8xx.x	Sn
		9xx.x	Other elements

Aluminium in its pure form is used in a variety of applications such as conductors or packaging materials because it is soft and light as well as having very good electrical conductivity (63 % of copper) [1]. The application of Al expands to other fields by addition of small amount of other elements, thus forming alloys. Differing in the processing routes, Al alloys are first sorted into casting and wrought alloys, and according to their alloying elements, into different series. The designation system for aluminium alloys is given in Table 2.1. By adding different elements, Al alloys can have different mechanical properties fulfilling the specific requirements. For example, 2xxx and 7xxx alloys are now widely used as trains and aircraft bodies due to their high strength.

2.2. 6xxx Series Alloys used in Automotive Industry

Aluminium alloys are increasingly used as car bodies substituting heavier metals based on economic and political pressure which calls for the reduction of fuel consumption and CO_2 emission [4]. In Europe, the automotive industry increases the average usage of Al alloys in passenger cars during the last decades [5]. Because of body-in-white (BIW) design, more Al sheet alloys, e.g. the 5xxx and 6xxx series alloys are used as panels [4]. The 6xxx series alloys can provide reasonable strength and formability as well as good corrosion resistance. It is heat treatable, i.e. can be bake-hardened. Nowadays, the most frequently used 6xxx alloys in automotive industry are AA6009, AA6010, AA6016 and AA6111 [5]. The performance of the alloys depends heavily on the design of the thermo-mechanical processing route, e.g. the formability depends on the rolling schedule and annealing temperature while the final strength depends on the annealing and quenching conditions coupled with the successive pre-ageing and paint baking treatments.

2.3. Ageing Response in 6xxx Series Alloys

During the production of car body panels, the Al alloy sheets undergo hot, warm and cold rolling followed by annealing at a high temperature (~540-560 °C) [5]. This annealing procedure serves as two purposes, (1) annealing out of dislocations which have been formed during rolling or recrystallisation which is necessary for further press forming (2) solution heat treatment (SHT) dissolving solutes back to solution for further paint-baking. The temperature region for this annealing (or SHT) is between the melting point and the solvus temperature. Then, a fast cooling (quenching) of the alloy from the SHT temperature to ‘room temperature’ (RT) is performed. The

aim is to preserve solutes in the Al matrix as much as possible: The alloy is now in the supersaturated solid solution (SSSS) state. At the same time, a certain amount of quenched-in vacancies are retained.

After SHT, the Al alloy sheets are stored at RT and transported to the car manufacturers. The alloy is then further press-formed to the required shape and then paint bake. During paint baking, which is equivalent to artificial ageing (AA) at ~180 °C for 30 min or ~205 °C for 20 min, the strength of the sheets increases due to the formation of strengthening precipitates, β'' [5]. A problem arises due to RT storage or natural ageing (NA) prior to baking because the alloy has then a slower hardening response and lower hardness after successive AA than the alloys without NA [6]. This phenomenon is so called 'negative strength response' and is considered to be caused by clusters formed during NA [6]. Since NA is unavoidable and in order to prevent the negative strength response, additional pre-ageing (PA) treatment is often performed directly after SHT [7]. During PA, the strength of the alloys increases, and the alloy shows very weak NA response afterwards [7, 8, 9]. It is believed that the metastable precipitates formed during PA can either act as nucleation sites for β'' [10], or directly transform to β'' [11] during subsequent AA, and therefore promote precipitation and increasing the rate of the hardening response [12, 13]. Precipitation in 6xxx series alloys is complicated as it will be influenced by many factors e.g. temperature, alloying elements etc. In order to further study negative strength response, an understanding of the precipitation sequence is required.

2.3.1. Precipitation Sequence in 6xxx Series Alloys

The basic precipitation sequence for ternary Al-Mg-Si alloys is regarded as [14, 15, 16, 17]:

SSSS→ Clusters → GP zones → β'' → β' → β,

where clusters refer to solute segregating together without specific structures. The composition of clusters found in the literatures will be discussed in more detail in the next section. In the fast years more phases have been found which lead to more complicated precipitation sequences, see below.

Two types of GP zones are described in the literature: (1) Plate like GP zones found by Matsuda [18]. During PA at the temperatures from 70 – 150 ^{o}C, mono layer or multi-layer GP zones are formed which have a positive effect on the successive AA [18]. (2) solute-rich spherical

GP zones with 1-3 in diameters are found by Mairoara [19]. Such zones are defined as disordered solute collections which have the same lattice parameters as the Al matrix.

β" is the dominant precipitate before the alloy reaches its peak-aged condition [19]. It is a needle–like coherent precipitate growing along a <100> direction of the Al matrix [20]. The structure of β" was first determined as monoclinic [19, 21, 22, 23] with lattice parameters of a=0.77 nm, b=0.67 nm and c=0.405 nm and an angle between a and c of 75^o [21]. Using high resolution transmission electron microscopy (HRTEM) and comparing experimental and simulated electron diffraction patterns, Andersen et al. have proposed another set of lattice parameters of a=1.516 nm, b=0.405 nm and c=0.674 nm with β=105.3^o [20]. In his model, the structure is assumed to be two unit cell containing units of Mg_5Si_6 [20]. However, using atom probe tomography (ATP), Serizawa and De Geuser found Al atoms inside β" and the Mg/Si ratio can be greater than 1 [11, 24]. Hasting has calculated the enthalpy for all possible compositions of β" [25] and proposed that a cell composition of $Mg_5Si_4Al_2$ is in a better agreement with the ATP experimental results.

Similar to the morphology of β", β' is rod-shaped and also grows along one of the <100> directions of the Al matrix. It has hexagonal structure with a=0.705 nm and c=0.405 nm [23, 26]. β' forms later than β" and is expected to be thermally more stable than β". From TEM analysis, β' can grow larger in size compare to β", with a length of ~500 nm [27].

It has to be noted that ambiguities in naming the phases are often found, especially for clusters and GP zones. For example, Maruyama and Matsuda used GP(I) to describe cluster formation [28, 29], while GP(I) and GP(II) also correspond to clusters and β" [30] respectively.

The clustering and precipitation sequence in 6xxx alloys varies with the presence of the other elements [31, 32, 33]. For example, if Cu is added as major alloying elements, then the precipitation sequence becomes [34, 35, 36, 37]:

SSSS→ Clusters → GP zone → β"→ β' → Q' → Q + Si.

Q' is the precursor of the equilibrium Q phase. Q' is having the lattice parameters a=1.04 nm and c=0.405 nm and γ=120^o [38]. However, these are only the main sequences in Al-Mg-Si(Cu) alloys. Other metastable phases, such as B′, U1, U2, L, S, C, have also been reported [38, 39]. L, C and S are all coherent precipitates growing along <100> of aluminium matrix [38, 39]. L has a

disordered rod or lath morphology and C is reported to be plate-liked having monoclinic unit cells [38].

Banhart summarized the sequence of phases found during age hardening [40], as shown in Figure 2.1. After the formation of co-clusters, various phases are possible to form according to different heat treatments and composition of the alloys.

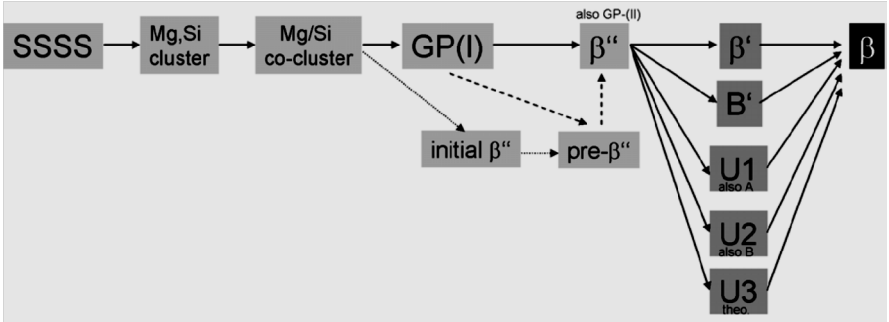

Figure 2.1. Sequence of phases found during age hardening of Al-Mg-Si alloys[40].It shows that after the formation of co-clusters, the precipitation sequence becomes complicated that many different kinds of phases can formed during the age hardening. Ambiguous use of phase designations complicates the discussion.

2.3.2. Early Stages of Clustering

Since the negative strength response is caused by clusters formed during NA, a lot of research has been carried out to investigate the clustering mechanism and the resulting structures. As it has already been mentioned in the previous section that ambiguous definitions of clusters and GP zones can be found, it is defined here that clusters are solute atoms aggregated together without a definite structures, whereas GP zones refer to the metastable phases that are found by Matsuda and Zandbergen [18, 19] and that possess a definite structure.

2.3.2.1. Stages of Clustering in 6xxx Series Alloys and Its Mechanism

Røyset observed that clustering can take place even at -40 ^{o}C [41], indicating that the process is activated at low temperatures. Indeed, during NA, several stages are observed by indirect experimental methods directly after quenching. For example, from resistivity measurement, it is found that the resistivity increases with NA time in different stages [42, 43]. Banhart et al. [40] have shown by in-situ resistivity measurement that the first transition stage could happen after ~5 min of NA, while in the 2nd stage; a fast increase in the resistivity is

observed. The transition from the 2nd stage to the 3rd stage takes place at ~85 min, after which the increase of resistivity slows down.

From isochronal Differential Scanning Calorimetry (DSC), two overlapping peaks associated to clustering are found [11, 14, 44, 45]; C1 situated at ~50 °C and C2 at ~90 °C. When carrying out NA before the DSC experiment starts, it is found that C1 disappears after ~1 hour NA while C2 is even not completed after 1 week of NA [14, 44]. Gupta and Lloyd [14] regarded C1 as Si-rich co-clusters while C2 as Mg-rich co-clusters [14]. They have also shown that no clustering peak is observed in high content Al-Si and Al-Mg alloy and therefore Si or Mg clusters do not form [14].

In-situ Positron Annihilation Lifetime Spectroscopy (PALS) was also performed and this type of measurement is sensitive to vacancy-related defects [46]. This is because positrons prefer to be trapped by defects with lower electron density and have a longer 'surviving time' there [46]. As cluster formation is expected to be closely related to the diffusion of quenched-in vacancies, the average positron lifetime would bring useful information on the clustering process [47, 48]. Though the average lifetime is a mixture of contributions from different annihilation types, the trends of the average lifetime changes during NA show the changes of the general configuration for the vacancy and its environments. The change of the average positron lifetime varies with Mg and Si content and is shown in Figure 2.2 [48], which shows similar features of the lifetime changes. At least 4 clustering stages are identified; (I) a transient regime of stable lifetime in some alloys (II) first significant decrease in lifetime up to ~100 min (III) increase of lifetime up to ~1000 min and (IV) re-decrease of lifetime. It is speculated that Stage (II) is related to the diffusion of Si by the help of vacancy, because higher composition of Si next to a vacancy yields a shorter positron lifetime. Stage (III) is related to Mg diffusion due to the fact that alloys with very low Mg concentration (< 0.1 %) shows no increase in lifetime in in-situ experiment at RT. For stage (IV), ordering of clusters could be a possible reason for the decrease of the lifetime again.

It can be seen from above that integral, non-imaging methods especially in-situ experiments are useful for investigating the different stages of clustering in Al-Mg-Si alloys as the transition between clustering stages is fast (can happen within few minutes of NA) and little sample

preparation is required before starting of the experiment. However, signals cannot easily be relate to the fraction, size and composition of the clusters.

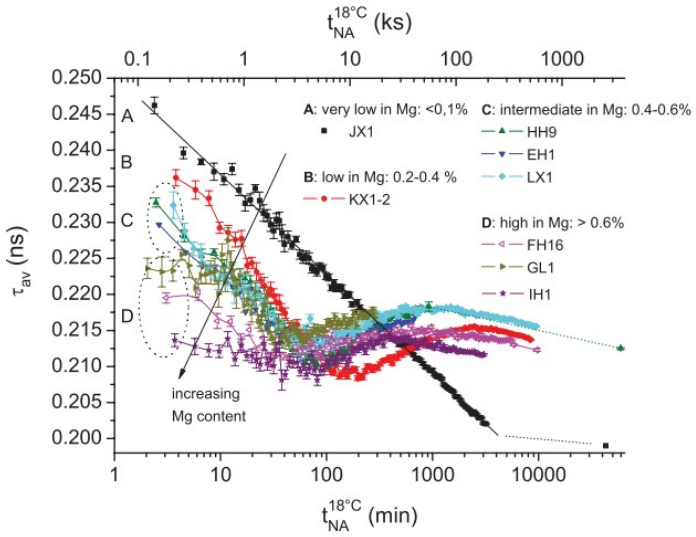

Figure 2.2. Average positron lifetimes during NA after SHT for alloys with different composition of Mg and Si. Similar trends of the average lifetime profile are observed for all alloys expect the one with very low Mg content < 0.1 % [48].

2.3.2.2. Composition of Clusters by Tomographic Atom Probe

The first atom probe study of clusters during NA was done by Murayama et al. [10]. The experiments were performed using a 1-D atom probe and using samples which were NA for more than 70 days. Both Si or Mg clusters and Mg-Si co-clusters with different Mg/Si ratios were detected by analysing integrated concentration depth profiles. They claimed that the size of these clusters is less than 10 detected atoms, although the clusters are hardly identified due to the noise from the background.

With the devolvement of the 3-D atom probe, little statistics could be obtained and visualisation of clusters became possible by 3-D reconstruction of signals from 2-D detectors and different kinds of clusters identification techniques. Using maximum separation methods, Serizawa et al. [11] has investigated an Al-Mg-Si alloy after NA for 7 days to 2.5 years. The size and Mg/Si ratios of the clusters detected covered a wide range. However, they do not change with NA time. A Norwegian group has further refined their parameters used in the maximum separation methods and investigated alloys either with low or high Si content [51]. They have

found that by setting d_{max}=0.6 nm, N_{min} = 8 for high Si alloy and d_{max}=0.7 nm, N_{min}=8 for low Si alloy, clusters with the average measured size of 10 solute atoms and the Mg/Si ~1 are found in both alloys.

The clusters found during NA can only be detected by atom probe. HRTEM shows insignificant contrast [10]. However, when alloys with excess Si are PA at 70 °C for 16 h, contrast from meta-stable phases can be observed. Murayama and Hono classified such phases as coherent GP zones with sizes of ~2 nm, however the structure is difficult to identify. Torsæter et al [12] also found similar results when an alloy with excess Si was PA at 100 ^{o}C for 16 h. The morphology of these clusters (although they do not have well defined structures) is slightly needle-shaped. From TAP studies it is found that the Mg:Si ratio of these 'high temperature' clusters is close to 1 [12, 11, 37]. Apart from the Mg/Si ratio, Mg and Si are more closely packed in these high temperature clusters compare to the clusters formed during NA.

The investigation of the composition of the clusters formed in Al-Mg-Si alloys is based on atom probe. However, it should be noted that there are still some drawbacks when using this technique. First of all, compared to indirect experimental methods, much time is required to prepare atom probe samples in the order of hours [40]. Second, the detection efficiency is ~50 % of the total atoms, meaning that 50 % of the atom is lost during detection [49]. The detection efficiency depends on the detector and type of TAP [49]. Third, experimental parameters, such as the chamber temperature, pulse fraction, etc will influence the content of different kinds of element detected, leading to a 'wrong' value for the clusters' composition [49, 50].

2.3.3. Clusters and Negative Strength Response

Clusters formed during NA influence the number density and size of β" phases formed during AA, causing negative strength response [6]. Pashley et al. [7] have first proposed a theoretical model to explain the negative strength response by considering a lower solute concentration due to the presence of clusters and the dissolution of the clusters which have a smaller radius compared to the critical radius that can survive as the nuclei for β". Their model was based purely on TEM investigations after AA. The understanding of the negative strength response further improved when researchers compared the clusters found during NA and PA by using TAP. Since the clusters formed during NA have a wide range of Mg/Si ratios, Serizawa et al. [11] proposed that these cluster would not dissolve during successive AA treatment but lower

the concentration of solutes available for β" formation. On the other hand, the clusters formed during PA at 100 ^{o}C have a Mg/Si ratio close to that of β" and are much larger, and therefore these clusters are thought to transform to β" during successive AA treatment [11]. Torsæter et al [12] have compared the clusters of samples which were PA with and without prior NA. They have found that the sample which was directly PA has clusters which are more closely packed and have more solutes inside the clusters, while a significant fraction of clusters with more extreme compositions (Mg-rich clusters in Mg rich alloy, Si-rich clusters in Si rich alloys) are found [12] in samples that have been NA before PA, which seems to support the findings of Serizawa et al. [11].

From what was mentioned above, the negative strength response appears to be fully explained by recent TAP results. However, negative strength response already develops right after a short NA time [44, 51, 52, 53], which means that the clusters formed during early stages play the most important role. The clusters that could be detected by TAP are already at Stage 3 of resistivity [40], C2 of DSC [44] and Stage IV of PALS [48]. Also, due to the detector efficiency and cluster identification technique, the clusters shown by TAP are all larger than 10 solute atoms, and cannot represent the whole picture.

2.4. Kinetics of Clustering by Thermal Analysis and Simulations

The transformation kinetics of a reaction can be described by obtaining a set of kinetic parameters, i.e. volume fraction α related function $f(\alpha)$, constant K_0 and effective activation energy Q [54], which are referred to Chapter 6. The most common way to obtain the kinetic parameters is by thermal analysis, for example Differential Scanning Calormetry (DSC). Only Gupta and Lloyd [14] have made an attempt to obtain the complete set of kinetic parameters for the formation of clusters in 6xxx series alloys. Their DSC results are shown in Figure 2.3 and the kinetic parameters are shown in Table 2.1. The overlapping peaks in the figure are C1 and C2 as mentioned in previous section. After obtaining the kinetic parameters, Gupta and Lloyd concluded that C1 is expected to form rapidly while C2 forms relatively slow.

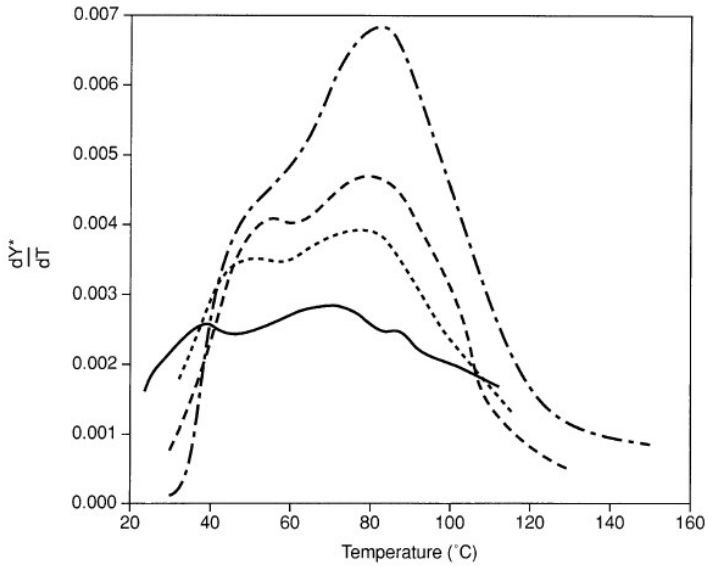

Figure 2.3. DSC curves of clustering process measured at different heating rates [14]. Two overlapping peaks are shown, indicating two kinds of processes occurring during clustering.

Table 2.1. Kinetic parameters [14] associated with the doublet of clustering reactions and heat effect of NA. Sub-peaks 1 and 2 refer to C1 and C2 mentioned in previous section.

Aging time, h	Total heat effect, J/g	$f(\alpha)$	K_0, /s	Q, kJ/mol
0	5.62	$(1-\alpha)$	70	24.9 subpeak 1
1	3.87	$(1-\alpha)$	3×10^4	44.4 subpeak 2
3	2.79	$(1-\alpha)$	2.5×10^7	66
24	1.49	$(1-\alpha)$	8×10^7	71

Other kinetic studies are more focused on only obtaining the activation energy Q. To certain extent, the value of Q signifies whether a reaction is easy to stimulate or not at a certain temperature. For example, in [55], C1 and C2 were first separated from the overlapping peaks by using Gaussians functions and the Qs for C1 and C2 are discussed according to the volume fraction transformed. Alloys with different Mg/Si ratio were investigated and the values for Q for both clusters lie in the same range from 45 to 90 kJ/mol. Gaber et al [35] also found similar Q values by using only the peak position. Besides Q obtained by DSC, Q has also been obtained by

isothermal experiments e.g. from in-situ PALS [48]. This was done by locating the transition from stage II to III at different experimental temperatures. Q found to be 74 kJ/mol, which also lies in the range of what is obtained from DSC.

Simulation is helpful to study many reactions on the atomic scale. By using simulation approaches, the kinetics of clustering in binary alloy systems has been studied [56, 57]. For example, from simulation, the general clustering stages in binary alloy system are found to be: 1) formation of small clusters; 2) formation of large clusters following a Fokker-Planck equation for the concentration; 3) coagulation of large clusters [56]. Moreover, kinetic parameters for these different stages can be well defined [56, 57, 58]. Recently, a diffusion model based on vacancy migration has been incorporated into a Kinetic Monte Carlo (KMC) simulation [59]. This approach has been proved to be useful to describe the mechanism of nanocluster formation in ternary alloy systems or even ternary alloy system with other additional elements [60, 61, 62]. Up to now, no attempt has been made to simulate the clustering reaction in 6xxx alloys. Therefore, KMC simulation would possibly provide more information when it is used to study the clustering in 6xxx series alloys in parallel to experimental methods.

2.5. Kinetics of Precipitation

Similar to the study of clustering, Q is also extensively discussed for β" and β'. Interestingly, Doan and co-workers [63] who studied all the exothermic reactions observed in isochronal DSC runs for 6061 obtain a higher Q for β" (105.4 kJ/mol) than β' (93.1 kJ/mol). The lower Q value for β' is difficult to understand, since in general, the phase forming at higher temperature is more difficult to activate [54]. A comparison of Q in different precipitates between Al-Mg-Si alloy with and without Cu is given by Gaber et al. [64]. They found Q values for β" formation is of 76.2 kJ/mol or 66.2 kJ/mol in alloys with or without Cu, respectively [64]. On the other hand, the corresponding Qs for β' are 116.6 and 105.6 kJ/mol [35]. Both the calculated Qs for β" and β' for Cu-containing alloys are lower than that obtained in nonCu-containing alloy, indicating that Cu promotes precipitate formation [64]. Other similar Q values for β" and β' are obtained in different Al-Mg-Si or Al-Mg-Si(Cu) alloys [64, 65, 66]. Afify makes a comparison of the Q in alloys with a fixed Mg concentration but a varied concentration of Si, and found that Q for the formation of β"and β' varies with Si concentration but a defined trend [67].

Dutta and Borrego used kinetic modelling to compare the difference in the formation kinetics of β" and β' in bulk and Al-Mg-Si composite materials, [68, 69, 70, 71]. These models are based on Johnson–Mehl–Avrami–Kolmogorov (JMAK) kinetics. Using a fitting model, the kinetic parameters for the formation of β" and β' for the based alloy 6061 are obtained. The Qs agree with those of other studies and range from 70 to 120 kJ/mol [53, 63, 64].

3. Methods

3.1. Materials

All the materials studied in this thesis are provided by Hydro Aluminium Rolled Products GmbH Bonn, Germany. The compositions of the alloys are shown in Table 3.1, obtained by Optical Emission Spectrometry (OES). All the samples can be classified into two groups, i.e. 4-10 and 4-10X groups, which differ in Fe and Mn content. The aim of having these two groups of materials is that 1) the 4-10 group can provide information on clustering or precipitation according to the designed amount and ratio of Mg and Si, and also the small amount of additional elements; 2) the 4-10X group reflects a the similar environment as commercial alloys where Fe-rich intermetallics are always present. After casting, the samples first undergo homogenization at 560°C for 12 hours, are then hot extruded at ~400 °C to a cross section of 3×20 mm. Finally, the samples were cold rolled to the final thickness of 1 mm.

Table 3.1. Actual composition of the alloys used.

Alloy	Compositions (wt%)							
	Mg	Si	Fe	Mn	Cu	Cr	Ti	Al
4-10	0.40	1.01	<0.001	<0.0005	<0.0005	<0.0005	<0.0002	99.21
4-10Cu	0.37	1.00	<0.001	<0.0005	0.04	<0.0005	<0.0002	98.64
4-10Cr	0.38	1.01	<0.001	<0.0005	<0.0005	0.01	<0.0002	98.65
4-10X	0.37	1.02	0.26	0.08	<0.0005	<0.0005	<0.0002	98.28
4-10XCu	0.39	1.01	0.26	0.07	0.04	0.0018	<0.0002	98.32
4-10XCr	0.37	1.02	0.26	0.07	<0.0005	0.01	<0.0002	98.28

3.2. Experimental Setup

3.2.1. Heat Treatments

3.2.1.1. Solution Heat Treatment (SHT) and Quenching

SHTs were performed in a vertical's aligned quenching furnace at 540 ± 5 °C. These samples which are solutionsied for 1 h, are performed under argon atmosphere after repeated purging in

order to prevent the samples from oxidation. For the rest samples which are used to study the evolution of microstructures during SHT, they are solutionised without argon protection because gas purging and argon filling requires a lot of time, more than the designed time for SHT. All samples are quenched into ice-water in order to achieve reproducible and fast quenching rate.

3.2.1.2. Natural Ageing (NA), Artificial Ageing (AA) and NA+AA

NA is performed by storing of the samples at RT. Temperature fluctuations of ±3 °C with a mean value of 22 °C are accepted for NA treatment. For AA or NA+AA treatment, samples are put into an oil bath after quenching with minimizing delay (less than 1 min) or with a specific delay at RT. The temperature of the oil bath is set to 180 °C and the actual temperature is 180 ±1 °C.

3.2.2. Microhardness

Microhardeness is used in this work to study the hardening behavior during NA and AA. It is normally expressed as the ratio of the load to the contact area of the indentation. Vicker's test was performed in which a diamond pyramid was pressed against the specimen with uniformly increasing load. By measuring the diagonals d_1 and d_2, as shown in Figure 3.1, the hardness of the specimen can be obtained from the following equation

$$H_V = \frac{2F\sin\frac{\gamma}{2}}{\bar{d}^2} \tag{3.1}$$

where F is the load, γ=136° is the angle between the two facets of the Vicker's pyramid, and d average value of the measured d_1 and d_2.

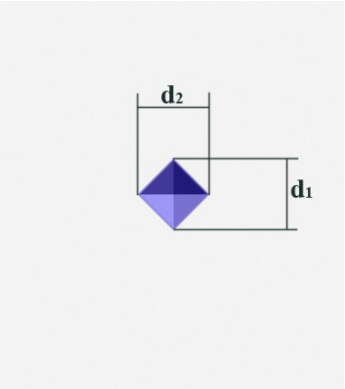

Figure 3.1. Schematic illustration of the indentation mark and its diagonals measurement.

$F = 100\,p$ $(0.981\,N)$ is applied on the sample with a strain rate/velocity of 10 p/s. 10 indentations are performed on the same sample and the average value of them is obtained. Only when the earlier evolution of hardness during NA is traced, microhardness is taken continuously up to 1000 min of NA and the measurements were not averaged. After 1000 min, the same approach as for the AA samples is chosen.

3.2.3. Differential Scanning Calorimetry (DSC)

All the DSC measurements were performed in Netzsch DSC 204 F1 Phoenix, which belongs to the heat flux type DSCs. As shown in Fig 3.2, the sample inside one pure aluminum crucible and another empty crucible are put into one single furnace which is made of silver. During measurement, the temperature and the heat flux between sample and empty reference crucible is measured directly. In order to obtain the "real heat flow" of the reaction in the sample, the heat flux should be calibrated before the measurements. This is done by performing calibration runs with several standard materials in which the heat evolution is well known, e.g. melting reactions of In, Zn, Al and Au.

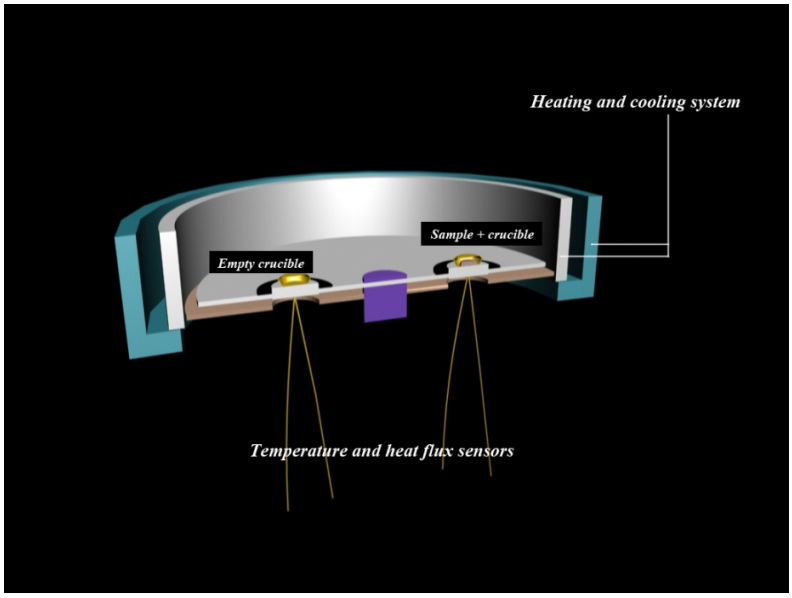

Figure 3.2. The schematic drawing of the heat flux DSC. Sample and referenced empty crucible are placed in one furnace and their temperature and heat flux difference during the DSC run is detected.

The samples for DSC measurement are cut and grounded to a disc shape (~Φ5 mm×1.2 mm). The mass of the samples is 64 ± 1 g. This preparation is done before the heat treatment in order to

guarantee that no dislocation would be introduced before the DSC measurement which can possibly provide sites for heterogeneous nucleation. Aluminium reference samples with 99.999% purity by the same preparation procedure are used to obtain the baseline correction for each measurement.

During the DSC measurement, nitrogen protective gas is used as flowing inside the furnace. The starting temperature is set as 0 °C for isochronal DSC measurements, and the temperature is reached by using cold gas nitrogen. Sample is put inside a crucible with a small hole on its lid before it is taken into the chamber of the DSC. After the sample is transferred to the chamber of the DSC, 3 min isothermal run is first undertaken in order to stabilize the system. Then the DSC is heated up with a constant heating rate (5, 10, 15 or 20 K/min), till the temperature reaches 600 °C.

3.2.4. Position Annihilation Lifetime Spectrum (PALS)

3.2.4.1. Experimental Setup and Procedure

The schematic of the PALS setup is shown in Figure 3.3. The PALS measurements are performed at CSIRO, Australia with a fast-fast coincidence system using Bicron scintillators. The detectors are vertically aligned and operated at “room temperature”. A pair of samples after quenching is immediately dried and stacked with the positron source in between to form a sandwich structure, see Figure 3.3. Then it is placed between the two detectors. After mounting the samples, in situ measurement is carried out to obtain the spectra during NA. The resolution function of the spectrometer is characterized by its full width at half maximum (FWHM) and is 0.234 ns. Na22 folded by Ti foil is used as the positron source which can provide an initial ~50 ± 10 μCi activity. The time interval between each spectrum is set as 1 min from the beginning to 370 min then changed to 3 min for the rest of the measurement.

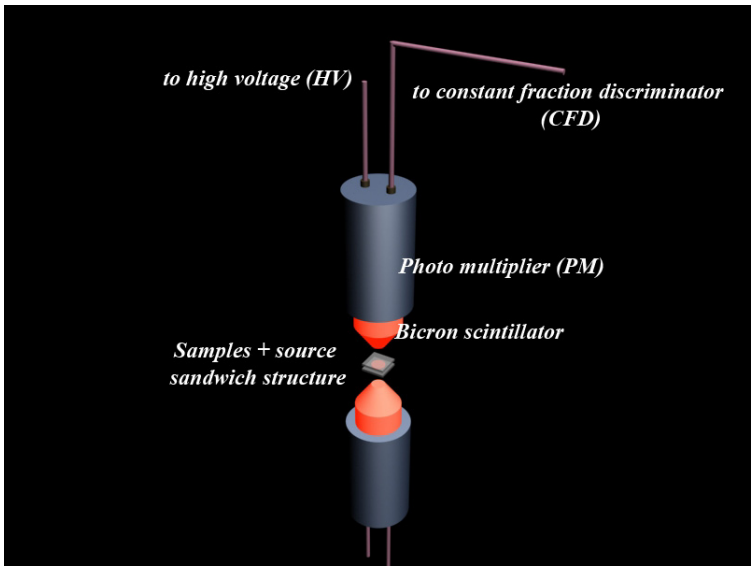

Figure 3.3. Schematic drawing of the arrangement of samples and detector in PALS measurement.

3.2.4.2. Data Analysis

Pure aluminum (99.999%) is used for source corrections. The spectra are processed by the program LT9 [72]. The spectrum is decomposed into three lifetime components corresponding to Al bulk, source material and "whiff". The fitted results are shown in Table 3.2. The lifetime of Al bulk is fixed to 0.16 ns. According to the fitting, the lifetime and intensity from the positron source are 0.37 ns and 0.4126 % respectively, while the contribution from the "whiff" is only less than 1 % with a lifetime of 2 ns.

Table 3.2. Fitting parameters in the pure Al sample as the source correction.

component	lifetime (ns)	intensity (%)
Al bulk	0.16	95.53
source	0.37	4.13
"whiff"	2.00	0.34

During fitting of the spectra of the alloys, the intensity of "whiff" is not fixed and allowed to fluctuate with an intensity below 1 %, while the lifetime of the "whiff" and the intensity and lifetime of the source are fixed according to Table 3.1. After subtracting source corrections and

the background from the spectra and deconvoluting the signal with the spectrometer resolution function (single Gaussian), the remaining data can be fitted by a single exponential by

$$N(t) = \frac{I}{\tau}\exp\left(-\frac{t}{\tau}\right) \quad (3.2)$$

where $N(t)$ is the count at a specific time t channel, I is the average intensity from the sample, τ the lifetime. Since it is expected that in reality a range of different lifetimes contributes to the PALS signal that cannot be separated, we call this lifetime τ_{av}.

3.2.5. Scanning Electron Microscopy (SEM)

SEM is used mainly for the characterization of the intermetallics and phase transformations during SHT. For SEM analysis, the longitudinal section (LS) of the samples is first mechanically polished, then electro polished using a solution of 70 % methanol and 30 % nitric acid at a voltage of 8-10 V at -30 °C. The SEM used in this work is Zeiss FIB-SEM CrossBeam 1540ESB. The working Electron High Tension (EHT) voltage is 5 kV and the working distance is set to be 5 mm. Both the inlens backscattered electron (BSE) and inlens secondary electrons (SE) detectors are used to obtain composition/phase and topological contrast. Energy Dispersive X-ray spectrometry (EDX) is also used in this work to obtain the composition of the intermetallics spectroscopy.

3.2.6. Transmission Electron Microscopy (TEM)

TEM is applied for the characterization of microstructures such as small intermetallics (less than 0.5 μm) and precipitates formed during AA. TEM samples are firstly ground and mechanically polished to a foil with less than 100 μm thickness. Then they are thinned by using twin-jet electro-polishing in a Tenupol cell with a solution of 30 % nitric acid and 70 % methanol at -30 °C with 15-17 V applied voltage.

TEM investigation is performed in a FEI CM30 or Zeiss Libra 200. The bright field (BF) images are used for observing the morphology of intermetallics or precipitates, measuring the length and the number density of the precipitates. Electron energy loss spectroscopy (EELS) mapping is applied to obtain the local thickness of the studied area. The thickness of the investigated area is calculated by the following equation [73]:

$$h = \lambda \log\left(\frac{I_0}{I_1}\right) \quad (3.3)$$

where h is the thickness of the sample, λ the mean free path the electron passing through the sample before it generates a Plasmon, I_1 is the intensity of the low loss area and I_0 the intensity of the zero loss peak.

After obtaining the thickness, the number density of the precipitate in one certain condition can be calculated by the following equation [19, 74]:

$$\rho = \frac{3N}{A(h+l)} \tag{3.4}$$

where A is the area of the measured area, l is the average length of the precipitates, N the number of the end-on precipitates and factor 3 comes from the fact that precipitates grow along $[100]_{Al}$ and the end-on precipitates present the direction which is perpendicular to the image.

3.2.7. Other Methods

In this work, light microscopy for the measurement of grain size and micro-probe for the measurement of composition of intermetallics are done in Hydro Aluminium Rolled Products GmbH Bonn, Germany.

3.3. Simulation

3.3.1. Simulation Setup and Parameters

The simulation is based on the assumption that, at low temperature, clusters do not modify the crystal structure of the base alloy, i.e. the solute atoms belonging to a cluster are still located on positions of the fcc aluminium lattice and the lattice constant is only marginally changed. A simulation box of 25×25×25 unit cells (62500 atoms) is built up and periodic boundary conditions are applied in all the directions. In this simulation box, all sites are occupied by atoms (Al, Mg or Si) according to the composition of 4-10. A single vacancy is generated and placed randomly at any site of the simulation box. This vacancy is conserved throughout the simulation. It is thermally activated and can jump to nearest neighbour (NNB) sites. The jump frequency of the vacancy towards each of its 12 NNBs is [75]

$$w_i = v_i \exp\left(-\frac{E_i^{act}}{k_B T}\right), \qquad (i = 1,2,3 \dots 12), \tag{3.5}$$

where v_i is the jump attempt frequency, E_i^{act} is the activation energy of a jump, k_B is Boltzmann's constant and T the temperature. One part of E_i^{act} is the migration energy of the vacancy into a site i (i = Al, Mg, Si) and can be determined by using the theoretical diffusion activation energy E_i^d and subtracting from this the formation energy of the vacancy E_V^f , both given in Table 3.3 [76]. The vacancy is assumed to have formed during quenching and is preserved after. E_i^{act} further contains the difference of the interaction energies of the vacancy with its nearest neighbourhood before and after the vacancy jumps. Therefore, the activation energy E_i^{act} required for the vacancy to move from its initial position j to the atom position i of its NNB atom i is expressed as [75],

$$E_i^{act} = E_i^d - E_V^f - (\sum_{k\in NNB_j} \varepsilon_{kV_{(j)}} + \sum_{k\in NNB_i} \varepsilon_{ki_{(i)}}) + (\sum_{k\in NNB_i} \varepsilon_{kV_{(i)}} + \sum_{k\in NNB_j} \varepsilon_{ki_{(j)}}) \quad (3.6)$$

NNB_j denotes all the nearest neighbours of site j. ε_{kV} and ε_{ki} are the interaction energies of a vacancy or atom with their NNB. Eq. 3.6 is an approximation, since we sum up pair interaction energies and therefore neglect any interaction between such pairs. The published (calculated) values of v_i, E_i^d, E_V^f, ε_{kV} and ε_{ki} [76, 77, 78] are listed in Tables 3.3 and 3.4 and serve as input parameters for our calculation. It should be mentioned that the interaction energies are calculated by subtracting pairs of reference configurations. This choice implies that $\varepsilon_{Al-Al}, \varepsilon_{Al-V}, \varepsilon_{Al-Si}$ and ε_{Al-Mg} are zero [79].

A Monte Carlo Step (MCS) number can be converted to a physical time Δt by the following equation [75, 80]:

$$\Delta t = \frac{1}{N C_v \sum_{i=1}^{12} w_i}, \quad (3.7)$$

where C_V is vacancy concentration and N is the number of atoms in the simulated box. C_V is calculated by

$$C_V = \exp\left(-\frac{G_V^f}{k_B T}\right), \quad (3.8)$$

where G_V^f is the Gibbs free energy of formation. Since $G_V^f = H_V^f - TS_V^f$, by taking H_V^f = 0.67 eV and $S_V^f = 0.7k_B$, [81, 82] a value C_V=1.41×10^{-4} can be obtained and is applied for our simulation. The NA temperature is 20°C (293.15 K). 10 simulation runs are performed and averaged.

Table 3.3. Kinetic parameters taken from Ref. 76.

v_{Al}	1.66×10^{13} s^{-1}
v_{Mg}	1.86×10^{13} s^{-1}
v_{Si}	1.57×10^{13} s^{-1}
E_{Al}^{d}	1.29 eV
E_{Mg}^{d}	1.27 eV
E_{Si}^{d}	1.15 eV
E_{V}^{f}	0.63 eV

Table 3.4. Chemical interaction energies (eV + favoured; - repulsive) taken from Refs 77, 78, 79.

ε_{Al-V}	0
ε_{Mg-V}	+0.015
ε_{Si-V}	+0.025
ε_{Al-V}	0
ε_{Al-Al}	0
ε_{Al-Si}	0
ε_{Al-Mg}	0
ε_{Mg-Si}	+0.04
ε_{Mg-Mg}	-0.04
ε_{Si-Si}	-0.03

3.3.2. Description of Flowchart

Before the program starts, the initial environment is set as following:

0a: Set the time t=0, T=293.15K, and set the step number $Step_{iter}$=0 and the total step number $Step_{max}$=93,750,000, which is equal to 1500 Monte Carlo Step (MCS);

0b: Set the initial position of all solutes and their types $type_i$ (i=1 Si; i =2 Mg) according to the composition of the alloy, e.g. in 4-10, 600 Si solutes and 278 Mg solutes respectively. The initial position of each solute is determined by the random number generator from Mersenne Twister [83] multiply each dimension of the simulated box (× 25);

0c: Set the initial position of a single vacancy with the same approach as for solute.

During the simulation, steps are as following:

1. Calculate the jump frequency w_i for the 12 NNBs of the vacancy;
2. Calculate the cumulative function R_j, used Eq. 3.7:

$$R_j = \sum_{i=1}^{j} w_i \tag{3.9}$$

where j=1,….12 and set $R_0 = 0$;

3. Obtain a random number m from Mersenne Twister, which $\in [0,1]$.
4. Search a NNB k, which fulfils:

$$R_{k-1} < mR_{12} \leq R_k \tag{3.10}$$

where k =1,….12;

5. Perform the position exchange with the vacancy and the k^{th} NNB;
6. Update the time t by

$$t = t + \Delta t \tag{3.11}$$

7. Set $Step_{iter}$= $Step_{iter}$+1;
8. If $Step_{iter}$< $Step_{max}$, return to step 1;
9. Analyse the printed results.

4. Experimental Results

4.1. Recrystallisation and Dissolution during SHT

4.1.1. Development of Microstructures during SHT

4.1.1.1. Grain Morphology

Figure 4.1 shows the evolution of grain morphology along the longitudinal section (LS) in alloy 4-10 during SHT. After cold rolling, the deformed grains are elongated along the rolling direction (RD) and grain fragmentations are observed, see Figure. 4.1a. The thickness of the grains is ~48 µm. After SHT for 2 min, recrystallisation has started but not completed, see Figure 4.1b. Recrystallisation has started on the surface of the sample, and smaller grains are found near the surface.

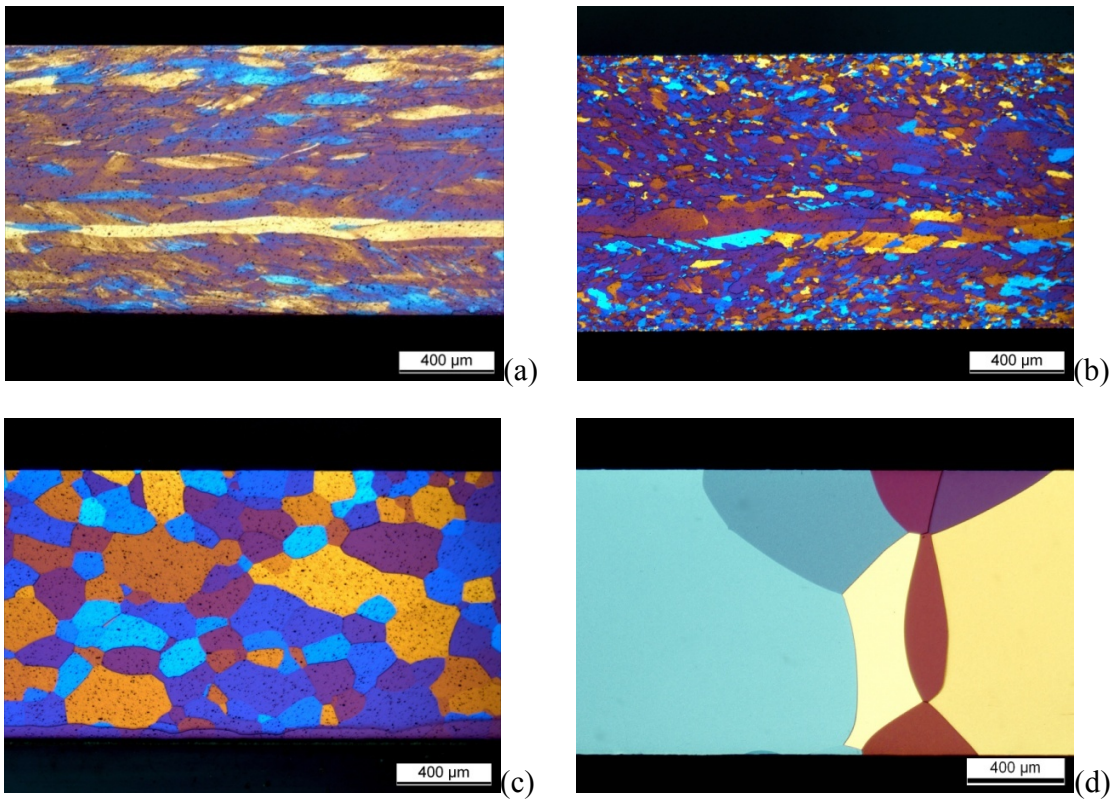

Figure 4.1. Light microscopy images of LS showing evolution of the grain morphology of alloy 4-10 at different stages: (a) cold rolled, (b) SHT for 2 min, (c) SHT for 5 min, (d) SHT for 60 min. Recrystallisation is found when the sample is SHT for 2 min. After SHT for 5 min, abnormal grain growth occurs.

After SHT for 5 min, the sample has completely recrystallised and the measured average grain size is ~160 µm along the RD and 104 µm along the normal direction (ND), see Figure 4.1c. Therefore, the aspect ratio of the grains is found to be close to 1, showing that the recrystallised grains are equi-axed. Extensive grain growth is found in alloy 4-10 after SHT for 60 min, as shown in Figure 4.1d.

For comparison, the evolution of the grain morphology along LS in 4-10X during SHT is shown in Figure 4.2.

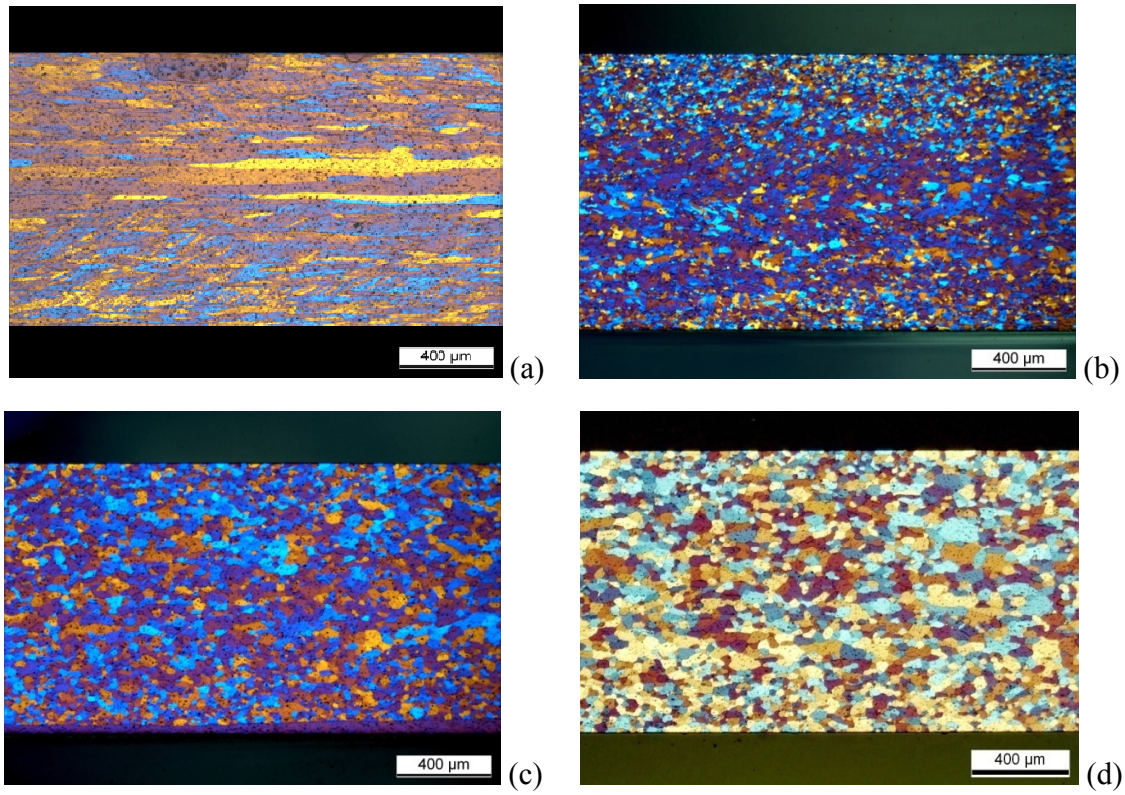

Figure 4.2. Light microscopy on the longitudinal section of 4-10X at different stages showing evolution of the grain morphology during SHT: (a) cold rolled (b) SHT for 2 min (c) SHT for 5 min, (d) SHT for 60 min. Recrystallisation is found in the sample after SHT for 2 min and grain growth is not prominent after SHT for 60 min.

The rolling microstructure is slightly finer as shown in Figure 4.2a. Most of the grains have recrystallised after SHT for 2 min which is faster than in 4-10 with the same SHT time, see Figure 4.2b. Slower grain growth is found in 4-10X after SHT for 5 min with the measured average grain size of ~46 µm along RD and ~35 µm along ND as shown in Figure 4.2c. When compared with SHT for 2 min, there is no significant difference of the grain size. The grains continuously grow

after SHT for 5 min and are found to have the measured average grain size of ~49 μm along RD and ~37 μm along ND, see Figure 4.2d. Therefore, recrystallisation starts earlier in 4-10X. The reason could be particle stimulated nucleation with the presence of intermetallics. Because more recrystallisation events, grain growth is then much slower.

4.1.1.2. Intermetallics

Figure 4.3a and b show the morphology of intermetallics after cold-rolling along the LS taken from the same area in 4-10 with different detectors. There are several bright areas in the SE image while the corresponding positions are hardly identified in the BSE images as shown in Figure 4.3a and b. The SE detector provides more information on the surface. Since the sample has been electro-polished, the bright area corresponds to certain phases which were not polished away as much as the Al matrix and more secondary electrons can escape from those positions. Contrast from the BSE mode depends mainly on the atomic number of the element. A similar contrast as the Al matrix in the corresponding positions shows that these phases have elements which are close to Al in the periodic table. EDX results for the particles indicated as 1 and 2 are given in Table 4.1. The particles contain 96 at.% and 95 at.% Si respectively. Therefore, the particle with the bright contrast in the SE image but no significant contrast in BSE is a Si-rich intermetallics. Similar Si-rich intermetallics are also found in 4-10X after cold rolling, see Figure 4.2c. 4-10X have more fine nm-scale Si-rich intermetallics compared to 4-10, see Figure 4.3a and c. Besides Si-rich intermetallics, there is another kind of intermetallics which gives rise to weak contrast in the SE image but to bright contrast in the BSE image, as indicated by arrows in Figure 4.3d. EDX results in Table 4.1 show that these intermetallics have similar Fe content, with more than 15 wt%, but they differ in the concentration of Si and Mn. According to the Fe/Si ratio and the concentration of Mn, the other Fe-rich intermetallics in 4-10X are identified as α-AlFeSi and α-Al(Fe, Mn)Si [84, 85, 86]. Concerning the shape of the intermetallics, because the samples have been cold rolled, the larger Si- and Fe-rich intermetallics are aligned along the RD. Also, some of the particles are pressed against each other during rolling, as shown in Figure 4.3d, indicated by a circle. Fragmentation of particles is also observed.

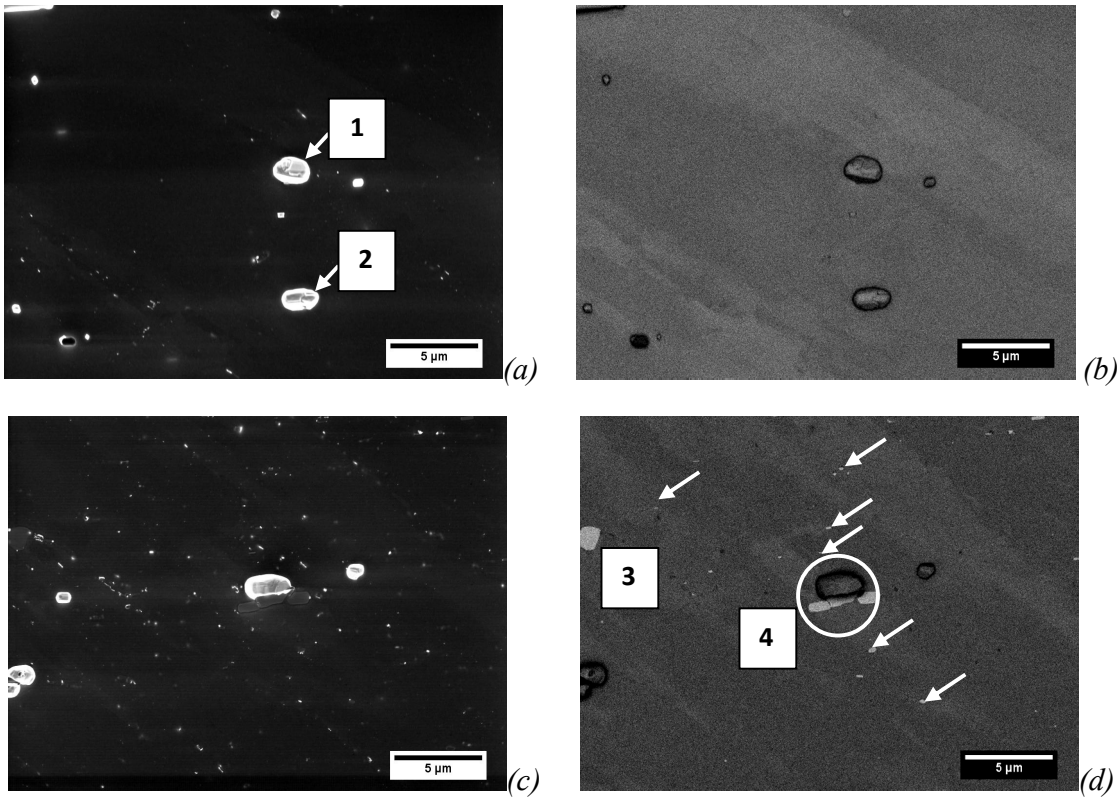

Figure 4.3. SEM images taken from the LS showing intermetallics in 4-10 and 4-10X after cold rolling. The Si and Fe-rich intermetallics are analysed by using different detectors (Fe-rich intermetallics are α phases: α− AlFeSi and α− Al(Fe, Mn)Si: (a) SE and (b) BSE images for 4-10, (c) SE and (d) BSE images for 4-10X.

Table 4.1. EDX Composition analysis in at.% at the position marked in Figure 4.3 showing two different kinds of intermetallics (Si-rich intermetallics and Fe-rich intermetallics).

Position	Mg	Al	Si	Mn	Fe
1	0.08	bal.	96.53	0.00	0.00
2	0.26	bal	95.35	0.00	0.00
3	0.08	bal.	15.92	0.51	12.72
4	0.07	bal.	9.11	4.05	11.92

Figure 4.4 shows the SE images of alloys 4-10 and 4-10X after SHT for 2 min. A high population of fine Si precipitates is observed in both alloys, which are spherical and have a

diameter of ~40 nm. It shows that the number density of these Si-rich precipitates is higher in the 4-10 than in 4-10X. From the above results, it is evidenced that rapid precipitation occurs during SHT. Therefore, after cold rolling, solutes could be retained in the Al matrix sufficiently enough for precipitation during SHT.

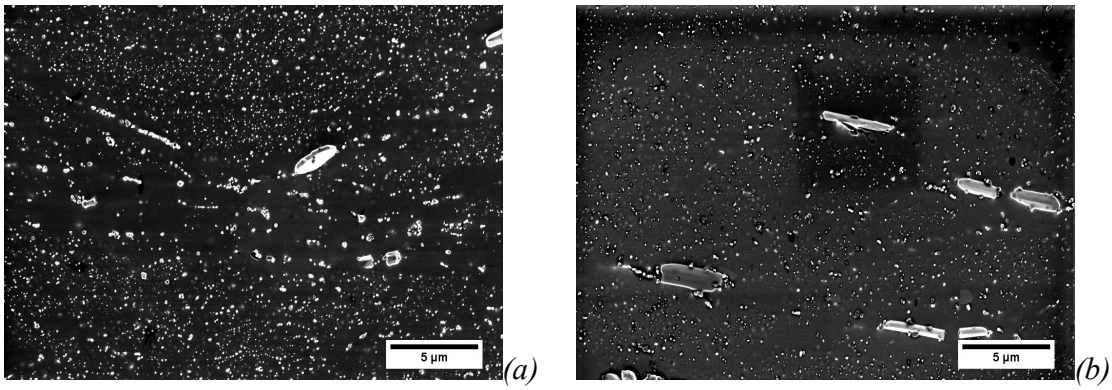

(a) *(b)*

Figure 4.4. SE images of (a) 4-10 and (b) 4-10X features Si-rich precipitates formed after SHT for 2 min and showing that during SHT for 2 min, secondary precipitation of Si-rich precipitates occurs in both 4-10 and 4-10X.

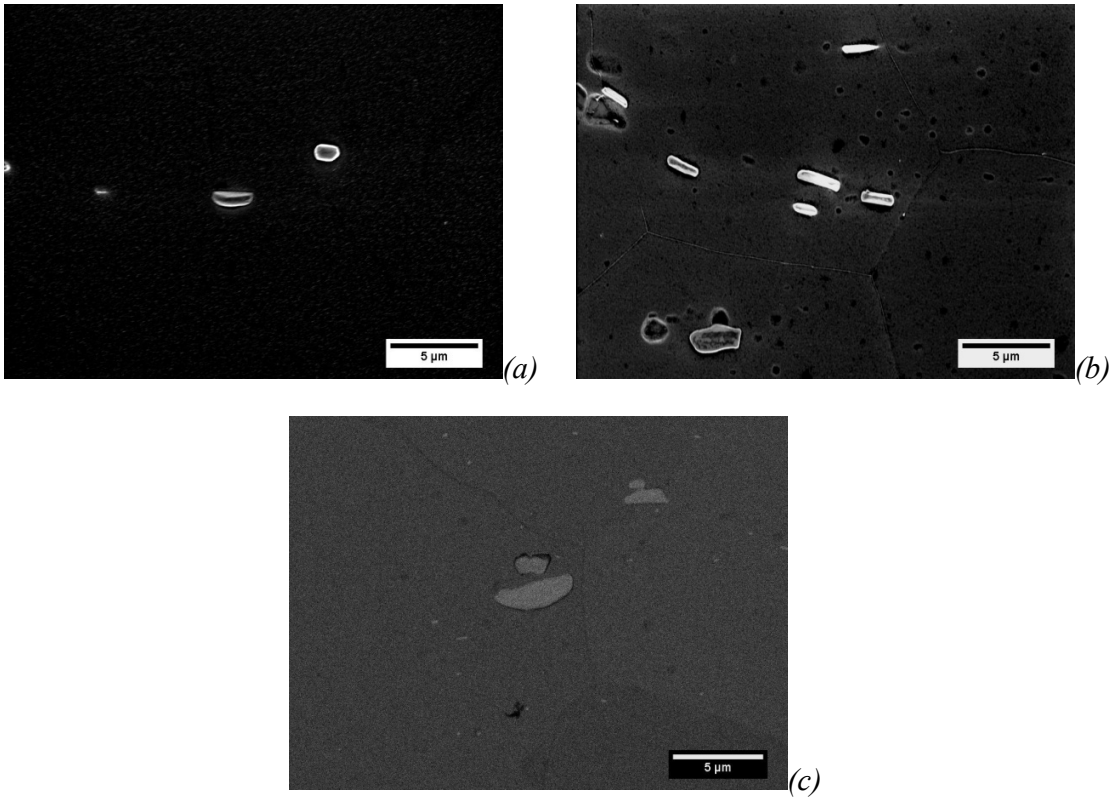

(a) *(b)*

(c)

Figure 4.5. SE images for (a) alloy 4-10 and (b) 4-10X and BSE image for (c) 4-10X showing the intermetallics after SHT for 5 min.

Figure 4.5 displays the morphology of intermetallics in alloy 4-10 and 4-10X after SHT for 5 min. The secondary Si-rich precipitates formed after SHT for 2 min and the fine Si intermetallics are no longer found. In 4-10, only big Si-rich intermetallics are observed as shown in Figure 4.5a. In 4-10X, both big Si-rich intermetallics and all the Fe-rich intermetallics are still present, which is seen in Figure 4.5b and c.

In summary, recrystallisation starts together with the precipitation of Si-rich precipitates during the first 2 min of SHT at 540°C in both alloys 4-10 and 4-10X. After 5 min, the formed Si-rich precipitates and the smaller Si-rich intermetallics are dissolved again. Rapid growth of grains is found in 4-10 after recrystallisation.

4.1.2. The Influence of SHT on the Successive Age Hardening Precipitation

If the sample has been sufficiently solutionised, e.g. for 60 min, then a supersaturated solid solution (SSSS) state can be achieved. The different exothermic reactions occurring during isochronal DSC runs for alloys 4-10 and 4-10X in this state are shown in Figure 4.6. The reactions corresponding to the exothermic peaks are listed in Table 4.2.

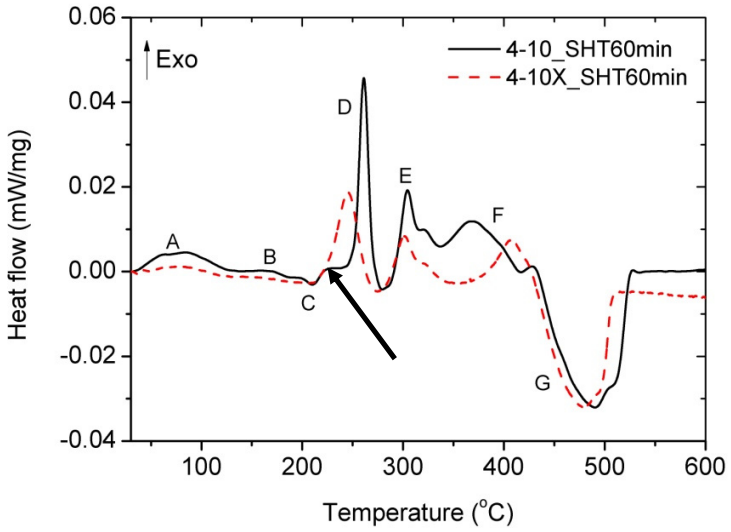

Figure 4.6. Isochronal DSC curves of alloys after SHT for 60 min with a heating rate of 10 K/min, showing different exothermic and endothermic reactions occurring in the temperature range from 30 to 600 °C. The corresponding reactions are listed in Table 4.2.

Table 4.2. Reactions corresponding to the heat absorbed or released in DSC, see in Figure 4.6.

Mark	Temperature range (°C)	Exo. (↑) or End. (↓)	Corresponding reaction
A	30-120	↑	Clustering
B	120-180	↑	GP zones formation
C	180-225	↓	Dissolution of the previously formed clusters or GP zones
D	225-275	↑	β"
E	275-340	↑	β'
F	350-450	↑	β
G	450-550	↓	Dissolution of the previously formed phases

In the low temperature range of 30 – 120 °C, several overlapping peaks are observed which correspond to clustering reaction. The exothermic reaction peak from 225-275 °C corresponds to the strengthening precipitates β" which are formed before the peak-aged condition. Different shapes of the β" formation peaks are found in alloys 4-10 and 4-10X. There is a shoulder in 4-10 as marked by an arrow in Figure 4.6. The β" peak in 4-10 is higher in magnitude but narrower than in 4-10X, with the peak position also ~25 K higher. The formation peaks of β locating in the temperature range from 350- 450 °C are also different in 4-10 and 4-10X. The β peak in alloy 4-10 is much bigger and its onset temperature is ~50 K lower than in 4-10X.

Figure 4.7 shows the isochronal DSC signals of alloy 4-10 and 4-10X after cold rolling and after different SHT times at a constant heating rate of 10 K/min.

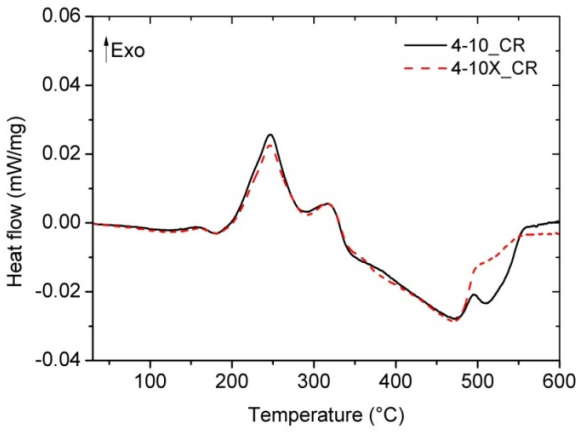

(a)

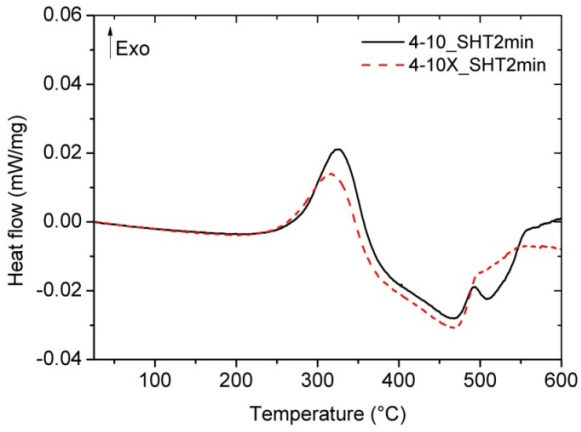

(b)

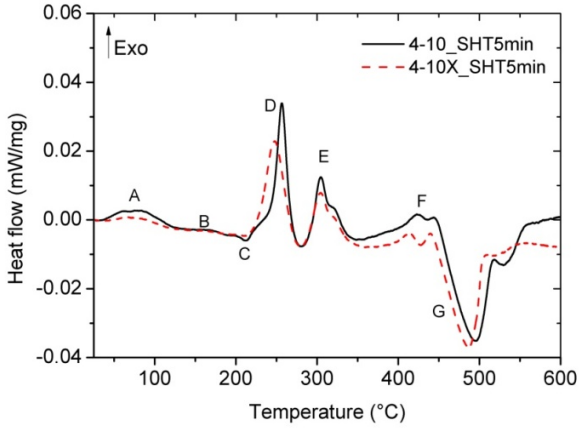

(c)

Figure 4.7. Isochronal DSC of alloys in the (a) as-received cold-rolled stage or after different SHT times (b) SHT for 2 min and (c) 5 min, showing that the main precipitation reaction located from 200-400 ^{o}C changes after different SHT times. After SHT for 5 min, the DSC curve is similar as after SHT for 60 min.

From Figure 4.7a it can be seen that during the DSC run, alloy 4-10 and 4-10X possess identical precipitation behaviour after cold rolling and no notable difference is found below 500 °C. Two main exothermic reaction peaks are located in the temperature range from 180 to 350 °C. The temperature of the highest exothermic reaction peak is ~240 °C, which is in the same temperature range as the formation peak of β'', see also Figure 4.6. The endothermic reaction starts at ~350 °C, 100 K earlier than the sample in the SSSS state. 4-10 and 4-10X again shows similar behaviour in the DSC signal after SHT for 2 min, see Figure 4.7b. The first exothermic reaction peak in Figure 4.7a is not observed while the precipitation peak located in the temperature range from 250 to 350 ^{o}C appears more pronounced. Similar results as the sample in SSSS state are found in the sample after SHT for 5 min, see Figure 4.6 and 4.7c. The corresponding reaction peaks with the identical labels are shown.

In summary, different exothermic reaction peaks are found by DSC in the samples after cold rolling or SHT for different times. This indicates that precipitation occurs in all samples during successive AA. The shift of the main exothermic reaction to higher temperature and the decrease of the heat effect for the exothermic reactions correlate with the Si-rich precipitate formed during SHT for 2 min. This indicates that the depletion of the solute in the matrix caused by the formation of the Si-rich precipitates significantly influences the successive ageing process. After 5 min, dissolution of the Si-rich precipitates formed and some of the fine Si-rich intermetallics has occurred; then the SSSS state can be reached. This indicates that the SHT performed at 540°C has to be at least 5 min. In the following study, samples are all SHT for 60 min although a short time could be sufficient.

4.2. Clustering and Precipitation in 4-10 and 4-10X

4.2.1. Stages during Clustering at RT Detected by Different Experimental Approaches

4.2.1.1. Hardness

Figure 4.8 shows the evolution of hardness for alloy 4-10 and 4-10X stored at RT (22 ± 3 ^{o}C) after SHT as a function of time.

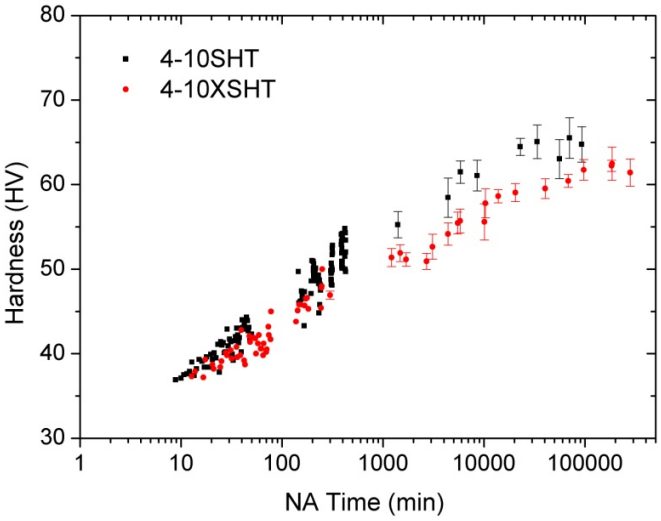

Figure 4.8. Evolution of hardness as a function of NA time after SHT showing the increase in hardness caused by clustering during NA. This effect ends at NA for ~20,000 min.

There is a gap without any hardness measured between quenching and the first recorded hardness caused by the time required for mechanical polishing of the samples after quenching. The initial values for 4-10 and 4-10X are similar, i.e. ~37 HV. As NA proceeds, the hardness for 4-10 increases faster than for 4-10X and after NA for 20,000 min the hardness of 4-10 and 4-10X are 65 and 60 HV respectively. After 20,000 min, no notable further increase of hardness is observed for both alloys. Therefore by hardness measurement, 2 stages in the evolution of hardness are found during NA: 1) monotonic increase up to ~20,000 min; 2) after ~20,000 min, further hardening effect is not notable.

4.2.1.2. Positron Lifetime

Figure 4.9 shows the evolution of average positron lifetime as a function of time during NA. Similar trends are observed in both alloys. Different stages are obtained: 1) The first two individual measurements in both alloys show that the initial average lifetime starts with a value between 0.225 to 0.230 ns, appearing as a short initial constant stage; 2) After the first stage, the average lifetime for both alloys continuously decreases till it reaches a minimum value (~0.215 ns) at around 70 min. 3) After the average lifetime passes through a minimum, it increases again till ~400 min, where it finds its maximum value of ~0.222 ns. 4) Finally the average lifetime in both alloys becomes stable or slightly decreases with an average value of 0.220 ns. From Stage 1 to

Stage 2, the average lifetime for 4-10X is slightly higher than 4-10, while in Stage 3, the average lifetime in 4-10 shows a faster increase than in 4-10X.

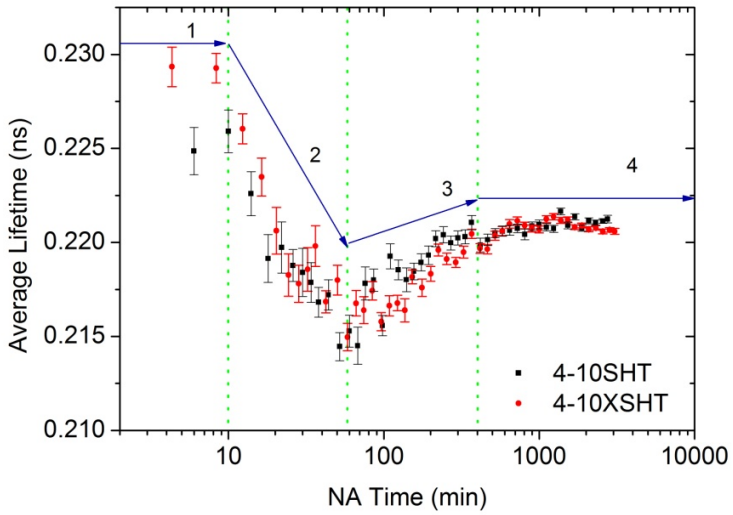

Figure 4.9. Evolution of average lifetime in PALS as a function of natural ageing time indicating stages of the average lifetime for positron annihilated at T = 18 ^{o}C: fast decrease in the first 70 min, slow increase from 70 to 400 min and constant lifetime after 400 min.

4.2.1.3. DSC

Figure 4.10 shows the DSC curves for 4-10 and 4-10X after SHT in the temperature range from 30 to 150 ^{o}C, which corresponds to clustering during NA as the range marked “A” in Figure 4.6.

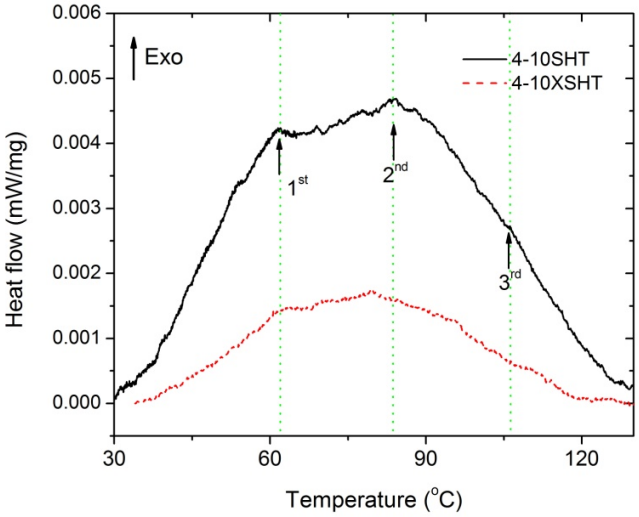

Figure 4.10. DSC after SHT in the temperature range from 30-180 °C at a constant heating rate of 10 K/min showing overlapping peaks for the formation of cluster in 4-10 and 4-10X in the same temperature range.

Two main overlapping peaks are observed in both alloys. They are located at ~60 and 85 ^{o}C. 4-10 has much bigger clustering peaks with a maximum heat flow of ~0.0042 and 0.0046 mW/mg for peak 1 and 2, respectively. Besides the first two clustering reaction peaks, a third peak situated at ~105 ^{o}C is found. In 4-10X, the 1st clustering peak overlaps with the 2nd clustering peak and appears as a shoulder.

Figure 4.11 shows the DSC curves corresponding to the clustering process in 4-10 and 4-10X after different NA times at a constant heating rate of 10 K/min.

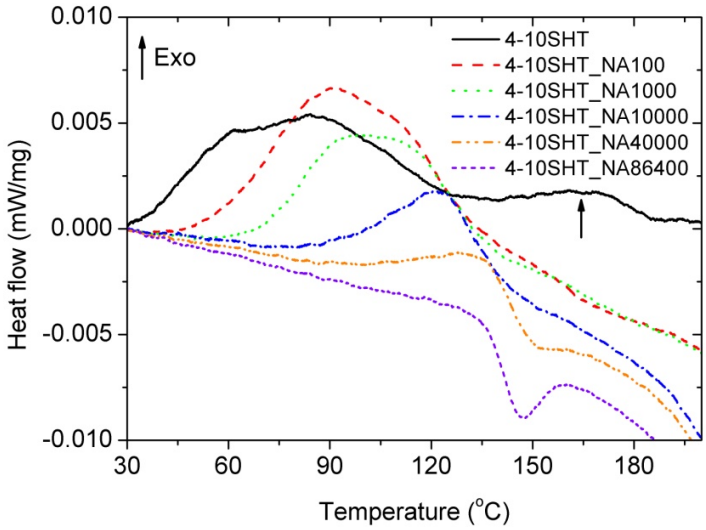

(a)

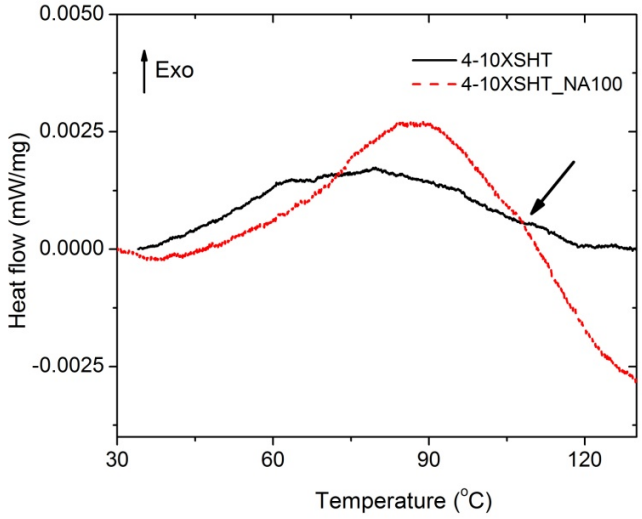

(b)

Figure 4.11. DSC curves corresponding to the clustering reaction in 4-10 and 4-10X after different NA times at a constant heating rate of 10 K/min. In (a), it is seen that in 4-10 after NA for 100 min, the 1st clustering process is hardly observed while the 2nd and 3rd clustering peaks appear more significantly. After longer NA time, the clustering peaks become weaker and the DSC curves shows a continuous dissolution reaction. In (b), 4-10X shows a similar trend. After NA for 100 min, the 1st clustering process is hardly observed but the 2nd and 3rd peaks are more pronounced.

In alloy 4-10, the 1st reaction peak has become very small and is hardly observed in the DSC curve after NA for 100 min, see Figure 4.11a. However, the 2nd and 3rd clustering peaks become larger. After 130 °C, a clear continuous endothermic reaction is observed. After NA for 1000 min,

the heat effect of the 2nd and 3rd clustering reaction peaks become smaller. As NA time proceeds, only the 3rd clustering reaction peak is observed and its peak position is shifted to a higher temperature with longer NA time. The bigger slope for the endothermic reaction in the longer NA time shows that the continuous dissolution reaction becomes more significant. After NA for 100 min in 4-10X, the 1st clustering process is hardly observed but the peaks for the 2nd and 3rd clustering process become more significant. The 3rd clustering peak is not visible in 4-10X without NA but becomes notable after NA for 100 min, as indicated by an arrow in Figure 4.11b.

In summary, the formed clusters which correspond to the 1st clustering process promote the later clusters' formation as a bigger clustering heat effect of the 2nd and 3rd is found in the sample after NA for 100 min. The clustering reactions which correspond to the 2nd and 3rd reactions are slow at 'room temperature' as the formation reaction heat is still easy to be identified after 10,000 min of NA. The clusters formed during NA are the clusters that would be dissolved at elevated temperatures, as an endothermic dissolution reaction is observed in the sample with prior NA. Distinguished by the formation rates, clusters during NA measured by the DSC can be defined as two stages: 1) fast clustering reaction within 100 min (1st clustering peak) 2) slow clustering reaction (2nd and 3rd peaks).

4.2.2. Precipitation during Isothermal AA

4.2.2.1. The Evolution of Hardness

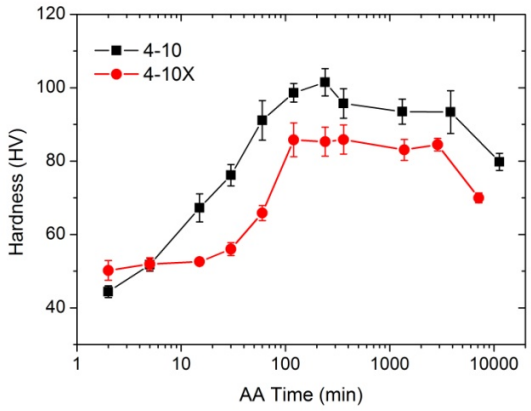

Figure 4.12. Evolution of hardness during AA in alloys 4-10 and 4-10X after SHT and quenching. During AA, both alloys show typical ageing response, where the periods of under-aged, peak-aged and over-aged are found. 4-10 shows faster hardening response and higher peak hardness than 4-10X.

Figure 4.12 shows the evolution of hardness for alloys 4-10 and 4-10X during AA at 180 ^{o}C as a function of time. An increase of hardness from the under-aged to the peak-aged condition is found for both alloys. The rate of increase in the under-aged condition is faster in 4-10 than in 4-10X, but the time to reach the peak-aged condition in 4-10X is shorter than in 4-10. The peak hardness in 4-10 is ~10 HV higher than in 4-10X.

4.2.2.2. TEM

Figure 4.13 shows bright-field (BF) images of alloys 4-10 and 4-10X for different AA times (20, 60 and 240 min) after SHT.

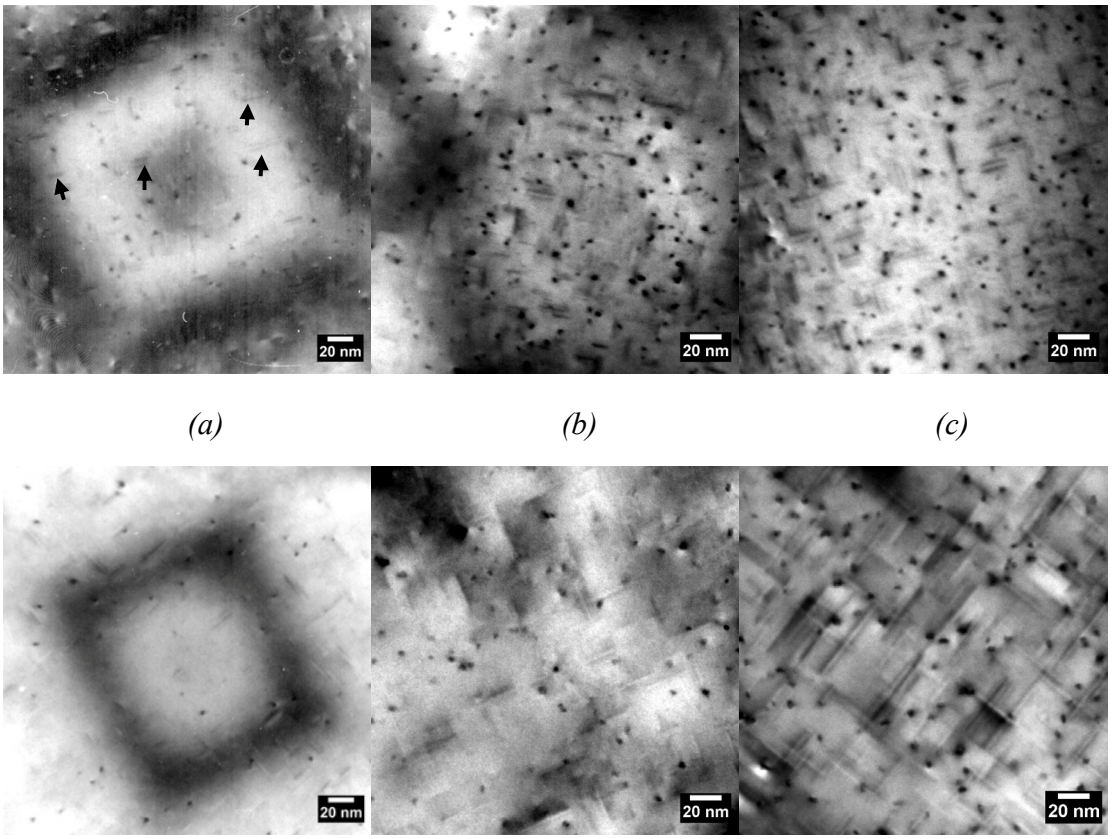

Figure 4.13. BF images of alloy 4-10 AA for (a) 20 min, (b) 60 min and (c) 240min, and alloy 4-10X AA for (d) 20 min, (e) 60 min and (f) 240 min. In both alloys with longer AA time, both the number density and size of the needle-shaped precipitates increases. Comparing the same AA time, 4-10 has a higher number density but smaller size of the precipitates than 4-10X.

The images are obtained by tilting the sample so that the electron beam is parallel to one of the <100> directions of the Al matrix and the precipitates are aligned along the <100> direction of the matrix. The end-on precipitates which are aligned along the electron beam appear as dot. The edge-on precipitates which are aligned perpendicularly to the electron beam show needle-like shapes, visible by the strain contrast around them. An increase of the number density and size of the precipitates is found in both alloys with increasing AA time.

In 4-10, contrast from fine precipitates is observed in Fig 4.13a. Though some of these precipitates already show needle shape, as indicated by arrows, the shape of most of them is hardly defined due to their small sizes. When the sample is after AA for 60 min, the needle shape of the precipitates is clearly identified by their strain field contrast, see Figure 4.13b. The precipitates are finely distributed in the Al matrix and the length of the precipitates ranges from 5 -10 nm. After AA for 240 min, no notable changes of the shape and size of the precipitates is found, when compared with sample AA for 60 min, see Figure 4.13b and c.

In 4-10X, after AA for 20 min, fewer precipitates than in 4-10 after the same AA time are observed, see Figure 13d and a. However, the needle shape of the precipitates is more clearly identified. Figure 4.13e shows that no notable increase of the number of the precipitates is found after AA for 60 min, but the precipitates are longer than in 4-10. After AA for 240 min, the precipitates have grown to a large extent, see Figure 4.13f.

A quantitative analysis on the number density, size and volume fraction of the precipitates has been done for samples of 4-10 and 4-10X AA for 240 min and is listed in Table 4.3.

Table 4.3. Quantitative analysis on the precipitates for the samples of 4-10 and 4-10X AA for 240 min. The number density of the precipitates in 4-10 is higher than 4-10X, while the length is shorter, leading to a higher total volume fraction of the precipitates.

Alloy	Number density ($\times 10^{22}/m^3$)	Length (nm)	Diameter (nm)	Volume fraction($\times 10^{-2}$)
4-10	7.8	13.9 ± 2.6	1.9 ± 0.5	0.31
4-10X	3.0	24.3 ± 8.5	2.3 ± 0.4	0.23

Twice as many precipitates are found in 4-10 than in 4-10X, but with a smaller length and diameter. The length of the precipitates in 4-10X scatters a lot, representing a larger range of growth rates of the precipitates in 4-10X. 4-10 has a higher volume fraction of the precipitates than 4-10X with a ratio of ~1.3.

Figure 4.14 visualises the morphology of the precipitates around the Fe-rich intermetallics in 4-10X after AA for 60 and 240 min.

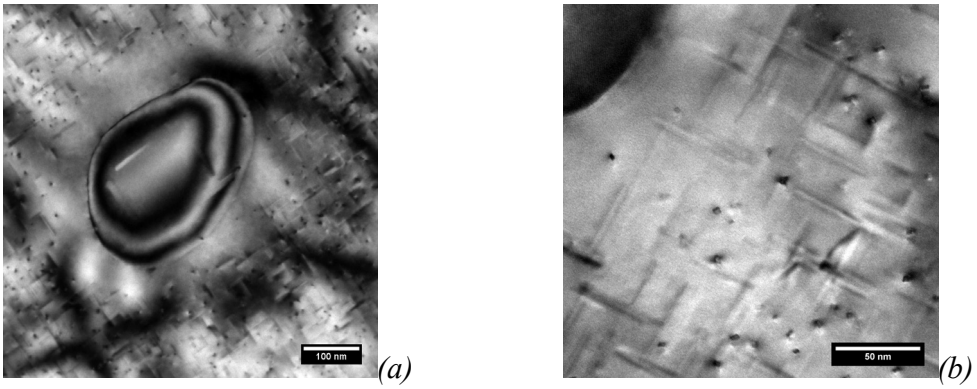

(a) *(b)*

Figure 4.14. BF images of 4-10X after AA for (a) 60 min and (b) 240 min showing precipitate-free zone(PFZ) around the intermetallics with its width of ~50 nm.

It is found that there is a region around the intermetallics where no precipitates are present i.e. this area can be regarded as precipitate-free zone (PFZ), see Figure 4.14a. The width of this zone is ~50 nm. Outside the PFZ, precipitates are present and have a morphology similar to what is found in the Al matrix. A similar PFZ is also found in the sample after AA for 240 min, see Figure 4.14b.

4.2.3. Relationship between NA and AA (Negative Strength Response)

4.2.3.1. Hardness

Figure 4.15 shows the evolution of hardness for alloy 4-10 and 4-10X during AA after different NA times.

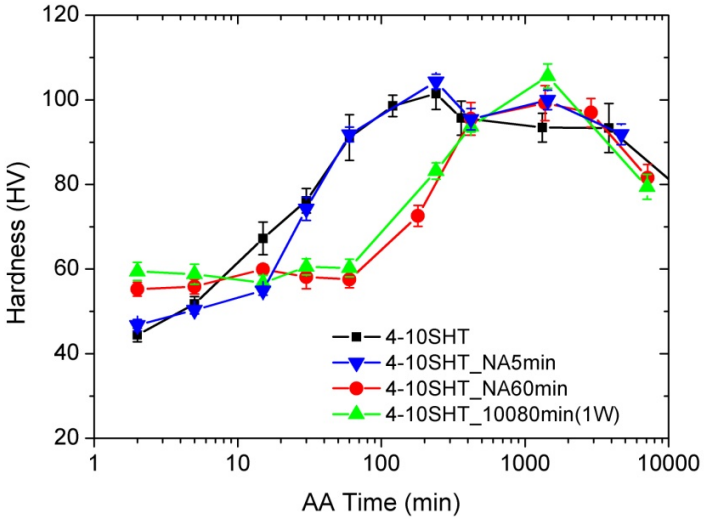

(a)

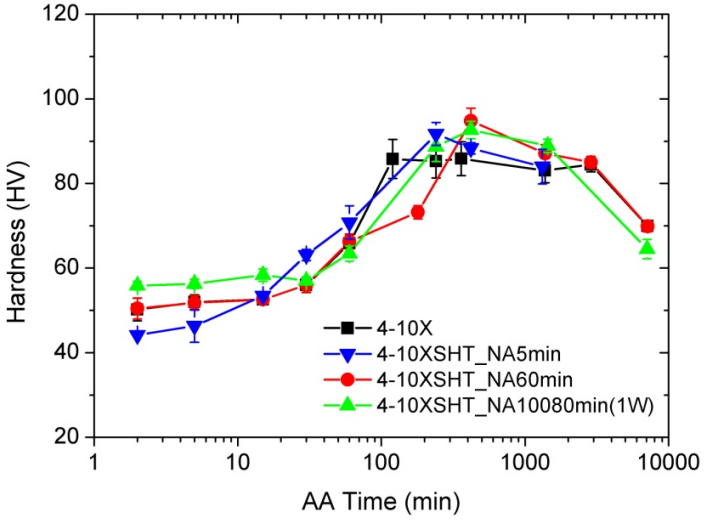

(b)

Figure 4.15. Evolution of hardness during AA after different NA times for (a) 4-10 and (b) 4-10X. NA for 5 min brings negligible negative effect on the successive AA, while NA for 60 and 10080 min brings significant and similar negative effect on the successive AA. The negative effect is more pronounced in 4-10 than in 4-10X.

An increase in the initial hardness values (after AA for 2 min) with NA time is found in both alloys after NA. By the extent of negative effect, two groups are categorised: Group I) Samples with NA time shorter or equal to 5 min. Group II) Samples with NA time longer than 60 min. In Group I, the sample NA for 5 min shows a similar hardening behaviour compared to the sample without delay except a slightly sluggish response of the increase of hardness for AA time < 30

min. In Group II, a similar hardening is observed in both samples: First, an incubation period is observed with nearly no increase or even a slight decrease in hardness for AA time < 60 min. Then, the hardness starts to increase up to the peak aged condition after AA for 60 min. Peak hardness is reached after AA for 1440 min, i.e. compared to the samples of Group I, more time is needed.

The influence from NA is not as pronounced in 4-10X as it is in 4-10. The significant different in the hardness for the two groups in 4-10 is not observed in 4-10X. In contrast, slightly faster hardening behaviour observed in 4-10X which has NA for 5 min. Moreover samples after NA for 60 and 10080 min have a slightly higher hardness than without NA, although the time to reach peak-aged condition is longer.

4.2.3.2. TEM

Figure 4.16 are the BF TEM images showing the morphology of the precipitates in alloys 4-10 and 4-10X after NA for 60 min then AA for 240 min.

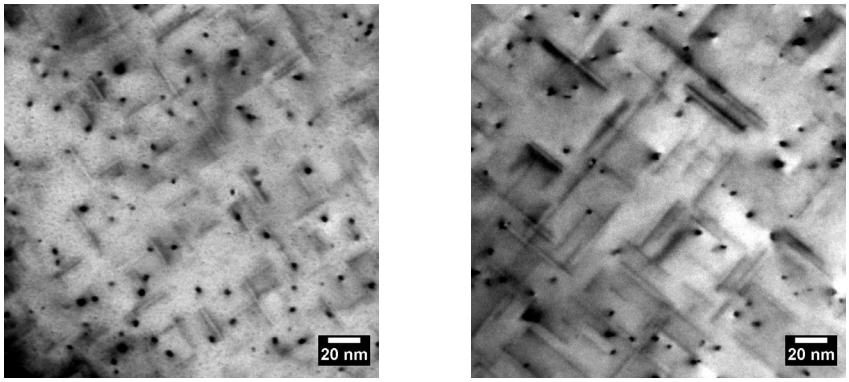

(a) *(b)*

Figure 4.16. BF images of (a) 4-10 and (b) 4-10X after firstly NA for 60 min then AA for 240 min. A decrease of the number density is observed in both alloys. The decrease in 4-10 is more obvious than in 4-10X. The size of the precipitates is larger in 4-10 but similar in 4-10X for NA.

From these images, the number density of the precipitates is significantly lower in 4-10 with NA comparing to the sample without NA, see Figures 4.16a and Figure 4.13c. The length of the precipitates is longer in sample without NA, with average value of 19.4 ± 5.2 nm. In 4-10X, the change of the number density of the precipitates is not as significant as in 4-10. Similar to 4-10, the average length of the precipitates increases with the average value of 35.1 ± 13.1 nm.

4.2.3.3. DSC

Figure 4.17 shows the DSC curves for 4-10 and 4-10X after different NA time in the temperature range of β" formation.

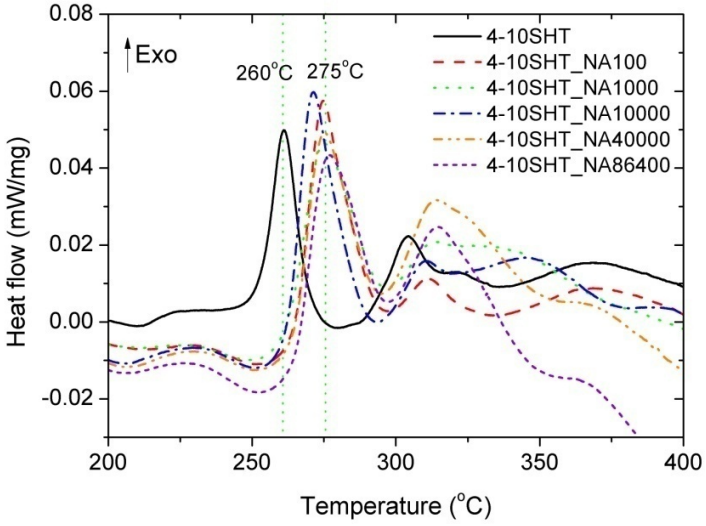

(a)

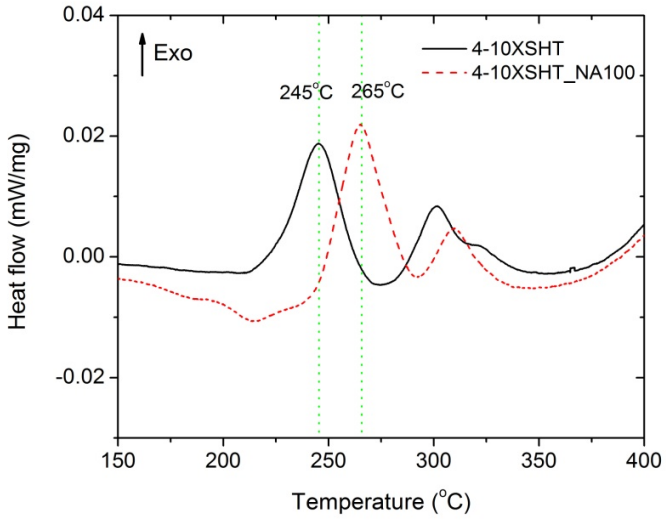

(b)

Figure 4.17. DSC curves for (a) 4-10 and (b) 4-10X after different NA times in the temperature range of β"formation. After NA for more than 100 min, the formation peak in 4-10 and 4-10X shifts from 260 °C to 275 °C and from 245 °C to 265 °C, respectively. Longer NA time only influences the height of the peak but does not affect on the peak position very much as shown in (a).

In 4-10, the position of the formation peak for β" shifts from 260 ^{o}C to 275 ^{o}C after NA for 100 min, see Figure 4.17a. Longer NA time does not influence the position of the formation peak for β" very much. It is noted that the formation peak shifts back a little bit to the lower temperature for sample NA for 10000 min. On the other hand, longer NA time influences the shape of the formation peak. With longer NA time, peak becomes wider but with lower height. In 4-10X, the β" formation peak temperature is 20 K higher in sample NA for 100 min compared to the sample without NA, as shown in Figure 4.17b.

4.3. Effect of Other Additional Trace Elements on Intermetallics, Clustering and Precipitation

0.01 wt.% Cr or 0.04 wt.% Cu was added as additional trace elements to alloys 4-10 and 4-10X, and are designated as 4-10(X)Cr and 4-10(X)Cu respectively. The morphology of the intermetallics when Cr or Cu is added is shown in Figure 4.18. The composition of the intermetallics as measured by micro probe is given in Table 4.4. Another alloy which both 0.01 wt.% Cr and 0.04 wt.% Cu are added in alloy 4-10X (4-10XCrCu) is also tested but showing no difference with 4-10XCu, therefore the result of 4-10XCrCu is not shown in this work.

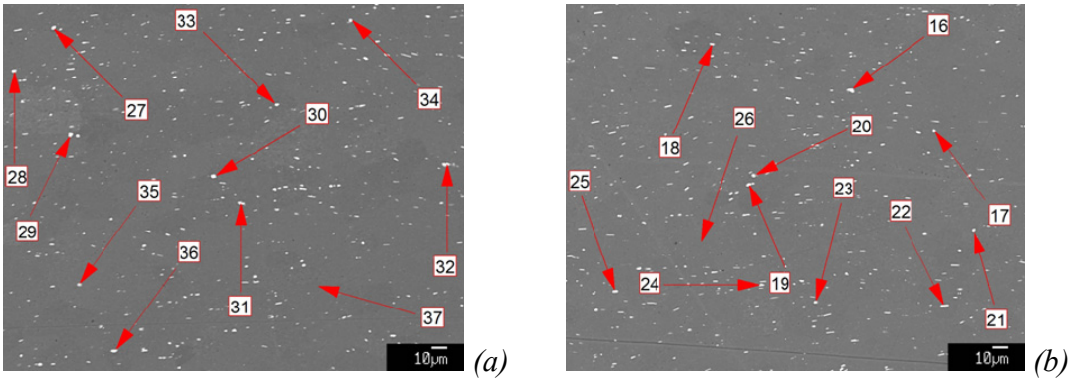

Figure 4.18. Light microscopy showing the morphology of the intermetallics in (a) 4-10XCr and (b) 4-10XCu. The composition on the intermetallics marked with numbers is given in Table 4.4.

Table 4.4. Composition in at. % on the intermetallics in 4-10XCr and 4-10XCu

Label	Mg	Si	Mn	Fe	Cr	Cu
27	0.2	11.3	0.8	8.5	-	-
28	0.1	8.7	4.2	9.3	0.3	-
29	0.2	8.6	2.4	7.8	0.2	-
30	0.2	9.0	1.8	11.4	0.1	-
31	0.2	14.3	0.6	11.7	-	-
32	0.1	8.0	4.0	8.7	0.4	-
16	0.2	15.2	0.7	11.6	-	-
18	0.2	7.5	3.2	7.6	-	0.1
19	0.2	8.0	3.8	8.7	-	0.1
20	0.3	8.2	0.4	5.7	-	-
21	0.2	7.6	3.6	8.8	-	0.1
24	0.1	8.5	4.0	9.4	-	0.1

Fine Fe-rich intermetallics with similar size as in 4-10X dispersed in the matrix are found for both alloys, as shown in Figure 4.10a and b. It is also found that Cr or Cu is present in Mn-containing intermetallics α-Al(Fe, Mn)Si.

Figure 4.19 shows the DSC curves for all the alloys directly after SHT at a constant heating rate of 10 K/min.

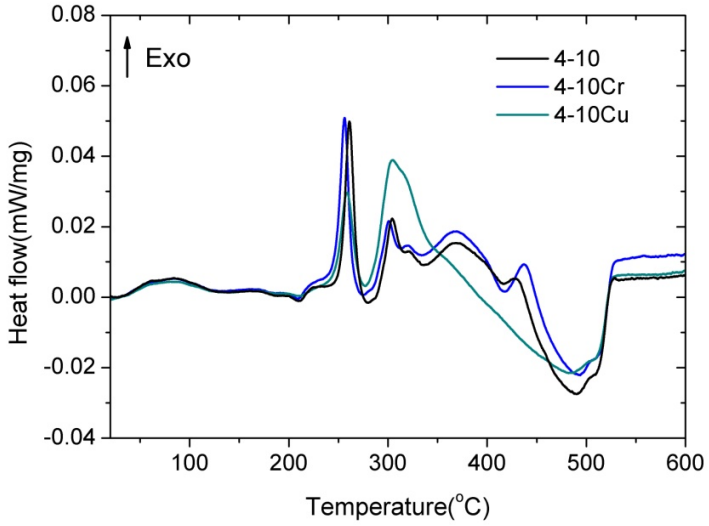

(a)

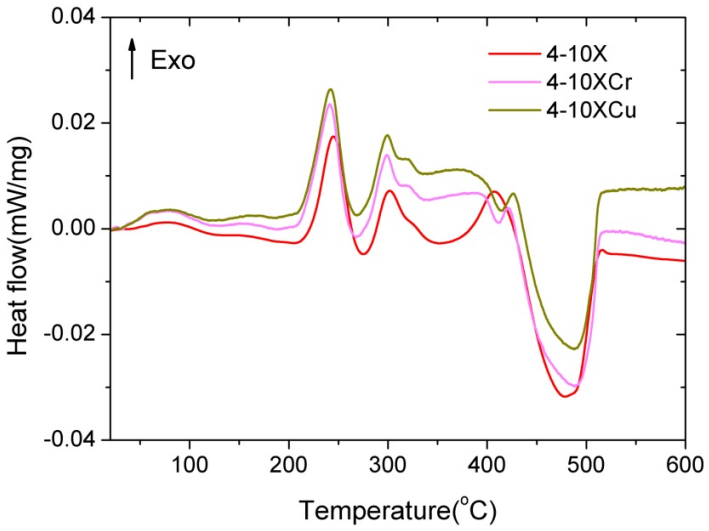

(b)

Figure 4.19. DSC curves of alloys directly after SHT with different additional elements in the (a) 4-10 and (b) 4-10X groups. Cu lowers the magnitude of the formation peak of β", while it increases the magnitude of the formation peak of β′ in 4-10. Cr shows no notable influence. On the other hand, Cu and Cr only change the magnitude and position of the precipitate formation peak of β".

When Cr is present in 4-10, no notable changes are observed in the DSC signal as shown in Figure 4.19a. The β" peak temperature only slightly shifts to lower temperature. Significant changes in the formation peaks are found in Cu-containing 4-10: the β" peak is smaller with its maximum heat flow only up to ~0.03 mW/mg, while a much larger β' peak with its maximum

heat flow up to 0.038 mW/mg is observed. Dissolution starts much earlier at 350 °C. The effect of the additional Cr and Cu on precipitation is similar in 4-10X, as shown in Figure 4.19b: Larger clustering peaks and the shift of the peak temperature of β" to lower temperature are observed.

Figure 4.20 shows a comparison of the clustering reaction obtained by DSC in all alloys.

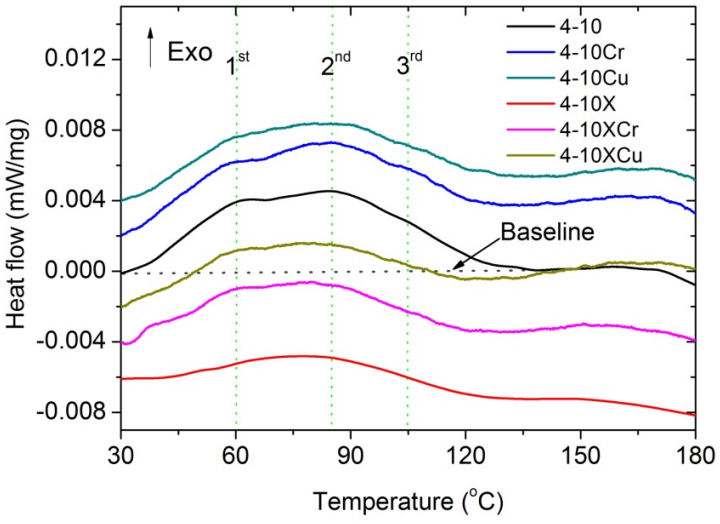

(a)

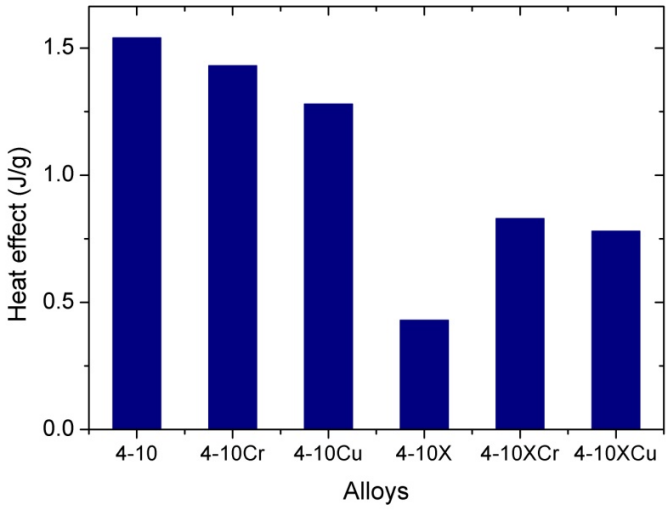

(b)

Figure 4.20. Comparison of clustering reaction measured by DSC in all alloys: (a) DSC signals and (b) heat effect under the DSC curves. In the 4-10 group, both of Cr and Cu lower the clustering effect. The effect from Cu is more significant. On the other hand, in the 4-10X group, Cr and Cu both increase the heat effect of clustering.

As three clustering stages in the 4-10 group and two clustering stages in the 4-10X group are observed, addition of Cr/Cu does not influence the general clustering stages, see Figure 4.20a. However, the 1st clustering peak is not obvious when Cu is added to 4-10, while the feature of the two overlapping clustering reaction peaks is more obvious when Cr/Cu is added to 4-10X.

In order to compare the total heat effect q for clustering within the alloys, q is defined as

$$q = \int_{T_{c0}}^{T_{ce}} (H - H_0) dT \quad (4.1)$$

where H and H_0 are the heat flows measured and the baseline of the heat flow, as indicated by the arrow in Figure 4.20a, T_{c0} and T_{ce} is the onset and end temperature for the clustering reaction, respectively.

Figure 4.20b shows the heat effect calculated from equation 4.1 for all alloys. It is found that the alloys in the 4-10 group have a larger heat effect compared to those of the 4-10X group. In the 4-10 group, both addition of Cr and Cu lower the clustering heat effect, while the effect is more pronounced in the Cu containing alloy, which is 0.2 J/g lower. However, addition of both Cr and Cu increases the clustering heat effect in the 4-10X group.

Figure 4.21 shows the evolution of hardness in the alloys during AA directly after SHT. In the 4-10 group, similar hardening behaviour is obtained in all three alloys. The only difference is that the decrease in hardness during over ageing is faster in Cr and Cu containing alloys. In the 4-10X group, lower hardness in the initial stage of AA for 4-10XCr and 4-10XCu is observed, see Figure 4.21b. After AA for 15 min, a faster hardening response is found in Cr and Cu containing alloys and the time to reach the peak-aged condition is shorter (~60 min) than in 4-10X (~120 min). Moreover, they possess ~10 HV higher peak hardness than 4-10X. However over-ageing comes faster than in 4-10X.

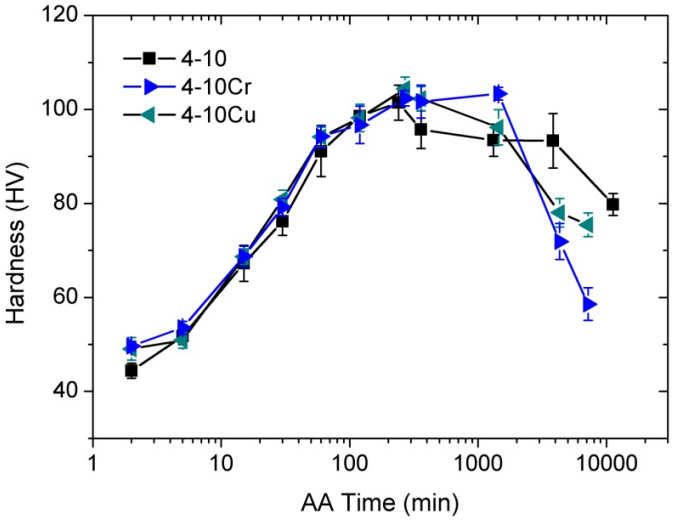

(a)

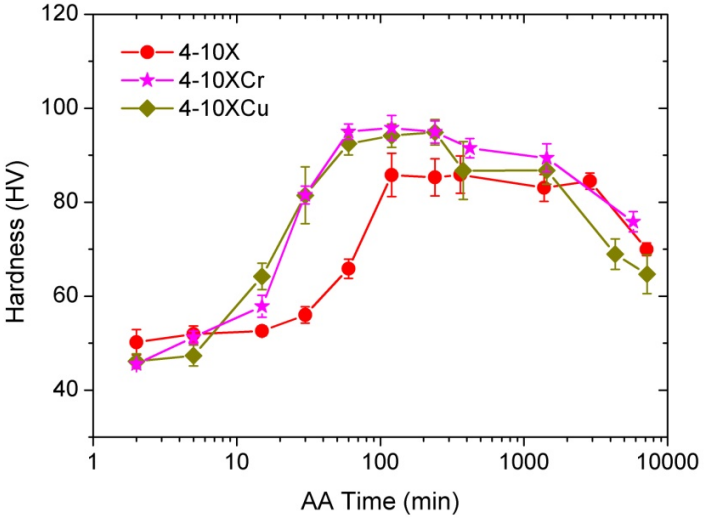

(b)

Figure 4.21. Evolution of hardness during AA in: (a) 4-10 and (b) 4-10X groups showing the effect on Cr and Cu. Direct ageing after quenching.

Figure 4.22 shows TEM BF images of alloys containing Cr or Cu in the 4-10 and 4-10X groups after AA for 240 min.

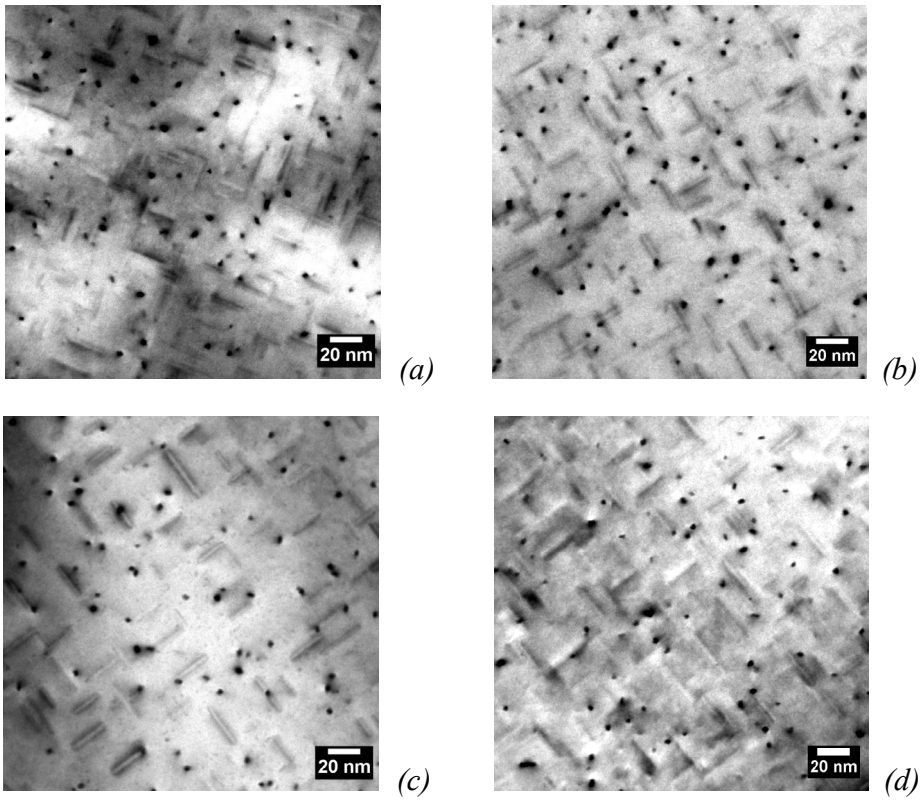

Figure 4.22. BF images of (a) 4-10Cr, (b) 4-10Cu, (c) 4-10XCr and (d) 4-10XCu after AA for 240 min showing only a slight difference in the precipitates' morphology in the 4-10 group, while higher number density and shorter precipitates are found in the 4-10X group.

The morphology of the precipitates after AA is not changed when small amounts of Cr and Cu are added. When Fe is not present, i.e. in the 4-10 group, no notable difference in the number density and length of the precipitates is found in the Cr and Cu-containing alloys. On the other hand, in the 4-10X group, a higher number density of shorter precipitates is observed.

Figure 4.23 shows the evolution of the hardness for alloys containing Cr/Cu. Two groups of hardness courses are found as in 4-10 and 4-10X alloys. The negative strength response is already established within 60 min of NA. The negative strength response of alloys in the 4-10 group is more significant than in the 4-10X group. When Cu is added the negative strength response is less both in 4-10Cu and 4-10XCu. Also, after NA for 5 min, a slight positive strength response for the successive AA is observed in 4-10XCr and 4-10XCu, where higher hardness is found.

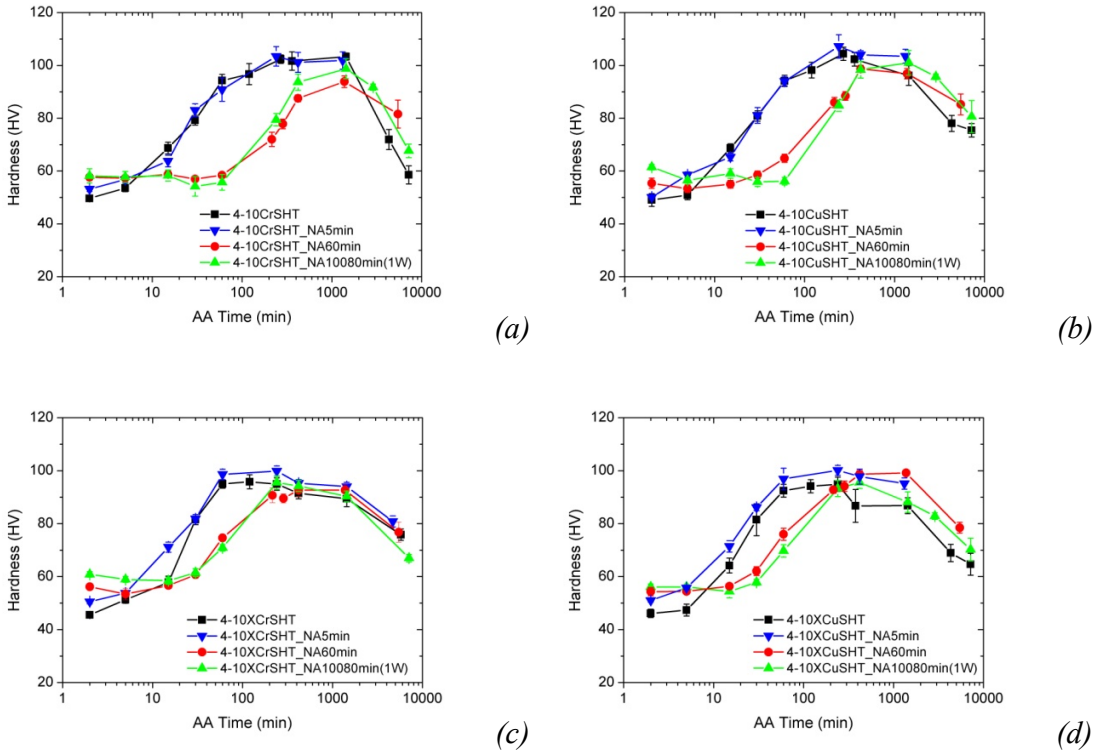

Figure 4.23. Evolution of hardness in (a) 4-10Cr, (b) 4-10Cu, (c) 4-10XCr and (d) 4-10XCu for different NA times before AA. The general trend on the negative effect does not changed, but when Cu is added, 4-10 and 4-10X shows less negative effect.

4.4. Summary of Chapter 4

In this chapter the main results are:

1) During SHT at 540 ^{o}C, the samples are partially and full recrystallised within 2 min of SHT in alloys 4-10 and 4-10X, during which Si-rich precipitates are formed. After 5 min, the formed secondary Si-rich precipitates have dissolved together with the fine Si-rich intermetallics, and grain growth is observed in 4-10. After SHT for 60 min, extensive grain growth has taken place in 4-10, unlike 4-10X, where no notable grain growth is observed.

2) Similar precipitation reactions during DSC runs are observed for both 4-10 and 4-10X, but a larger heat effect of clustering and a sharper formation peak of β" located at a higher temperature is found in 4-10. A higher number density of precipitates with smaller average length is observed in 4-10. Its volume fraction is larger than in 4-10X.

3) Different stages of clustering during NA are found for both alloys. Clustering within the first 100 min contributes most to the negative effect.

4) Cu directly affects the precipitation sequence with a smaller formation peak of β" but larger β'. A smaller 1st clustering peak is found in alloy 4-10Cu. This smaller heat effect corresponds to weaker negative strength response.

5) Cr and Cu both increase the clustering reaction in the Fe-containing alloy and a stronger negative effect is found than in base 4-10X. A higher number density with smaller average length of the precipitates is observed in both 4-10XCr and 4-10XCu.

5. Results of Kinetic Monte Carlo Simulation

5.1. Visualisation of Clusters

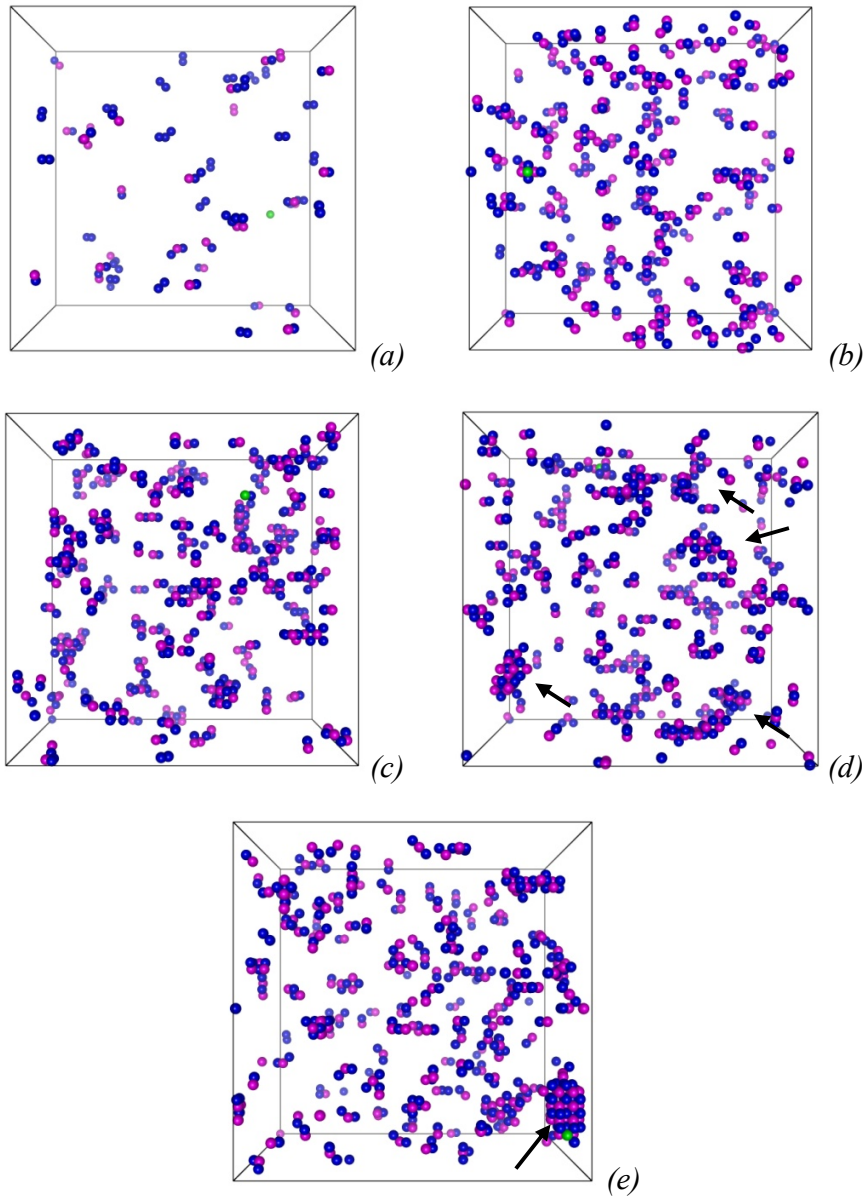

Figure 5.1. Simulated atom distributions at the (a) initial state, (b) t=1 min, (c) t=10 min, (d) t=100 min, (e) t=1000 min for 4-10. Purple: Mg, blue: Si and green: vacancy. Al atoms and isolated Mg/Si atoms are not shown. Dimers and trimers exist in the initial stage already and rapidly develop during NA. In the final stage, small and big clusters coexist in the system.

In the simulation, clusters are defined to be any configuration of two or more neighbouring solute atoms. Visualisation of the clusters is done by a free visualization software Vesta [87] for image reconstruction.

Figure 5.1 shows the reconstructed 3D mapping of clusters together with the position of the vacancy for different NA times obtained by the KMC simulation. As shown in Figure 5.1a, at the initial stage, dimers and trimers exist in the random computer-generated system. The vacancy is randomly located at a position which is only surrounded by Al atoms. A marked increase of the number density of clusters is found after NA for 1 min, Figure 5.1b. Clusters are small and most of them contain only few atoms. Dimers and trimers are easily identified. At this time, the vacancy has diffused to the position next to one of the small clusters and is attached to the solutes. No significant changes of the number density are visible after NA for 10 min, see Figure 5.1c. The size of some of the clusters increases: several solute chains and bigger clusters with a loose structure appear. The vacancy has diffused to another position and is still attached to a solute which belongs to a dimer in the upper right corner. In Figure 5.1d, clusters with more than 10 atoms are observed after NA for 100 min in certain positions of the simulated box. Some clusters arrange to a relatively condensed structure as indicated by arrows in Figure 5.1d. The vacancy is now trapped inside one of the clusters in the upper position of the simulated box. In the final stage of the simulation, fewer of clusters are observed, while several big and condensed clusters are found, see Figure 5.1e. The biggest cluster at the lower right corner of the simulated box containing more than 50 atoms shows an ordered arrangement of solute atoms, where Si and Mg atoms are aligned layer by layer. Meanwhile, the vacancy has been trapped in the biggest cluster.

5.2. Stages of Clustering

Figure 5.2 shows the calculated cluster density and fraction of solutes in clusters as a function of NA time.

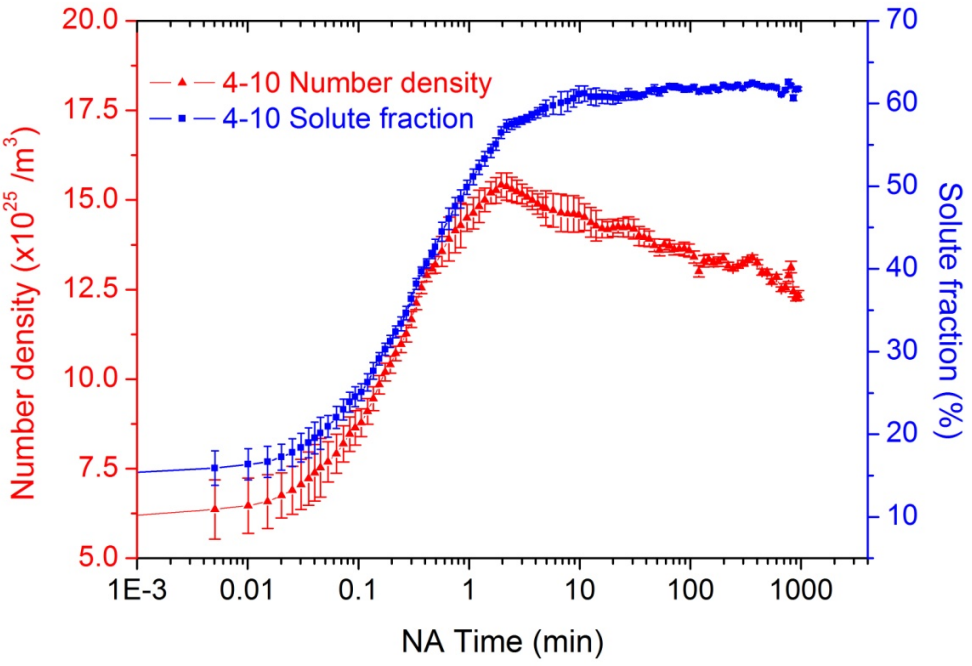

Figure 5.2. Calculated cluster density and fraction of solutes in clusters as a function of NA time. Both the number density and fraction of solutes in clusters increase before the first 2 min of NA. The number density then decreases while the fraction of solutes in the cluster still increases. In the final stage of the simulation, the fraction of solutes in the cluster is saturated while the number density of the cluster continues to decrease.

Three stages are identified by judging the changes of the number density and solute fraction in the clusters:

Stage 1 (0–2 min): Clustering starts from pre-existing clusters which have ~6×10^{25} /m^3 in number density and contain ~18 % of all the solute. Correlated with Figure 5.1a, it is known that these are mainly dimers and trimers. After a slow period of increase, both number density and solute fraction increase simultaneously and rapidly for 2 min, when the number density finds its maximum value of ~1.6×10^{26} /m^3 and the solute fraction is now ~58 %.

Stage 2 (2–10 min): After 2 min, the number density of clusters starts to decrease while the solute fraction still continuously increases. The fact that more solutes is bound in the clusters shows that the average size of the clusters increases while some clusters vanish. Correlated with Figure 5.1b and c, growth of some clusters by consuming individual solute atoms and other clusters already formed in their surrounding is found.

Stage 3 (10–1000 min): The fraction of solute levels off at, which is ~60 %, while the number density of clusters continuously decreases till the end of the simulation. This indicates that there is an equilibrium between solute atoms attaching to a cluster and leaving a cluster during this process, while the change of the number of clusters is caused by coalescence among clusters.

5.3. Size Distribution of Clusters

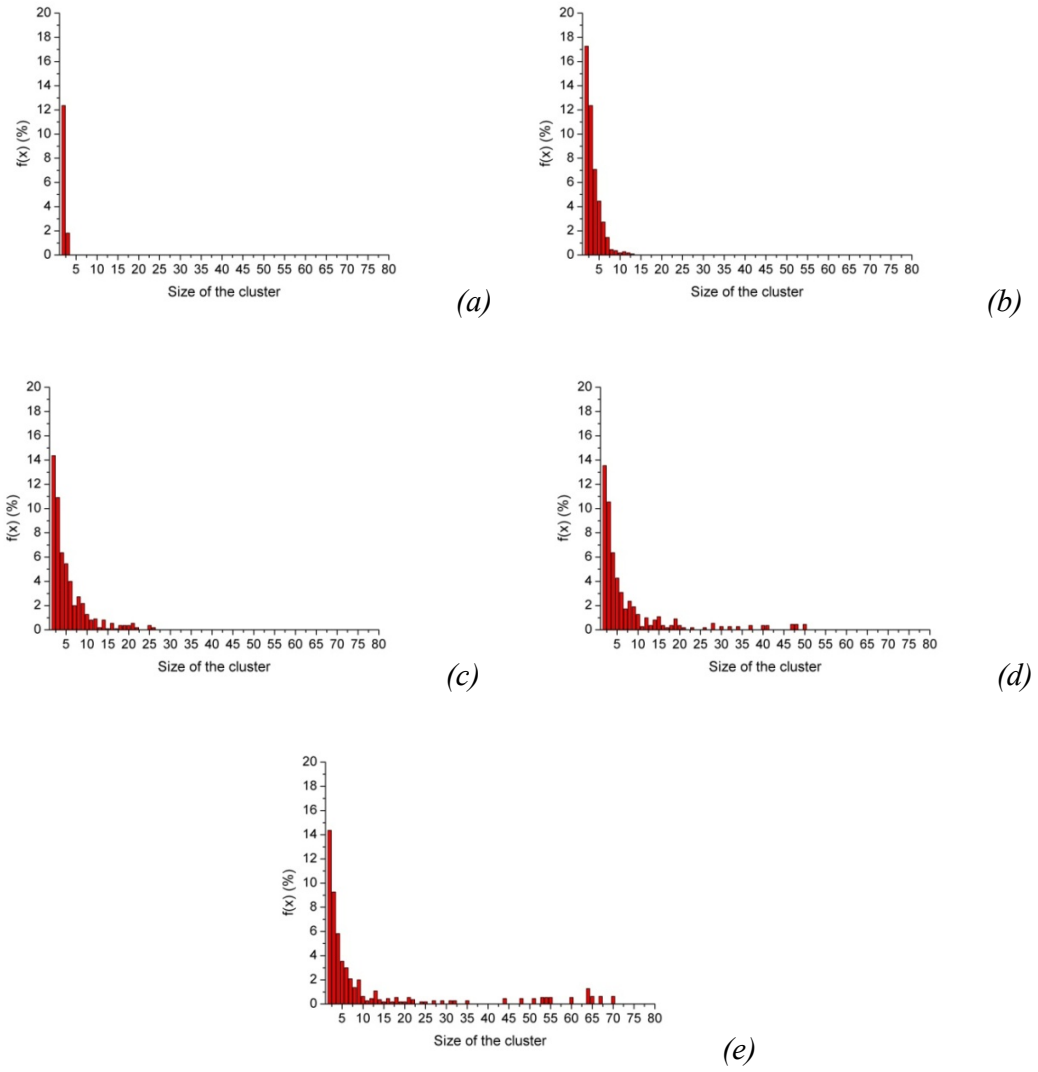

Figure 5.3. Size distributions of clusters after different NA times: (a) initial stage, (b) t=1min, (c) t=10 min, (d) t=100 min and (e) t=1000 min. Smaller clusters (< 15 atom) develop in the first 2 min of NA while in the later stage, a population of big clusters gradually develops.

The size distribution function $f(x)$ of clusters is defined as:

$$f(x) = \frac{N_x x}{N_{total}} \times 100\% \quad (5.1)$$

where N_x is the number of clusters containing x solutes and N_{total} is the total number of solutes in al cluster. $f(x)$ corresponding to the same times selected for 3D mapping in Figure 5.1 is plotted in Figure 5.3. Corresponding to Figure 5.1a, it can be shown in Figure 5.3a that only dimers and trimers contribute to the size distribution. The contribution of dimers and trimers is 12 % and 2 %, respectively. After NA for 1 min, the contribution from dimers increases to ~17 % while for trimers is ~12 %. The main population are clusters with less than 5 atoms, see Figure 5.3b. Clusters with more than 10 atoms also appear but their contribution is negligible. The cluster size distribution has broadened with its tail reaching to about 25 atoms after NA for 10 min, see Figure 5.3c. The contribution from dimers and trimers has decreased to 14 % and 11 %, showing that some of the dimers and trimers merge with each other or are adjacent to bigger clusters and are not counted as small clusters anymore. Another population of size distribution located in the range of 15 to 30 atoms appears but is still not significant. The population of the bigger continuous to develop and is more prominent, see Figure 5.3d. In the final stage of the simulation, Figure 5.3e, the contribution from the small clusters (less than 10 atoms) further decreases, while a clear population of big clusters with its peak contribution located at around 65 solute atoms is found. A cluster corresponding with this size is that shown in the lower right corner in Figure 5.1e.

5.4. Vacancy Movement during Clustering

During cluster evolution, the vacancy can be in various environment that can be categorised as follow: 1) in the matrix, Figure 5.4a; 2) binding with a single solute, Figure 5.4b; 3) bound to with a cluster and located on its surface, Figure 5.4c; 4) trapped and located inside a cluster, Figure 5.4d.

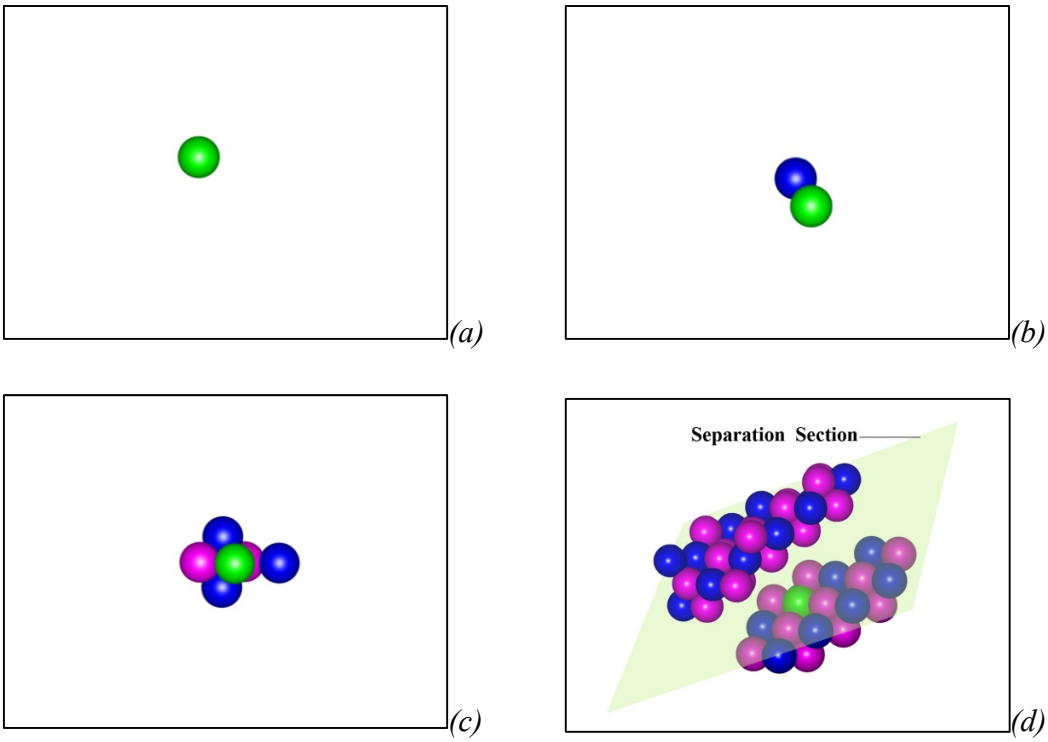

Figure 5.4. Typical example for the different environments of the vacancy (mapping from the simulation data at a certain time): (a) i =1: with 12 Al atoms (Al atom is invisible), (b) i =2: binding with one single solute (Mg or Si), (c) i =3: binding with a cluster (on the interface between cluster and Al matrix) and (d) i =4: located inside a cluster that has been pulled apart perpendicular to a plane.

The definition of the fraction of time $g_i(t)$ that the vacancy stays in a specific environments i as shown in Figure 5.4, is:

$$g_i(t) = \frac{t_i}{t}, \tag{5.2}$$

where t_i is the time the vacancy spends in the i^{th} environment (i = 1: in the matrix, 2: binding with a single solute, 3: binding with a cluster, 4: trapped inside a cluster). A vacancy is considered trapped in a cluster if at least 3 pairs of solute atoms can be identified, where the vacancy lies in the line connecting the atoms of each pair.

Figure 5.5 shows the fraction of time that the vacancy spends in a specific environment. In the initial stage, the vacancy spends most of its time either in the Al matrix or with one single solute atom. As clustering proceeds, the fraction of time for the vacancy in such environments decreases and drops to close to 0 till the end of the simulation. On the other hand, the fraction of time for vacancy binding with a cluster, though it starts with a lower value of ~0.27, increases

until NA for 3 min and becomes the most frequent configuration with the value of ~0.45. After 3 min, this frequency stays relatively constant till the time reaches 8 min. Then it decreases till the end of the simulation. The first 1 min sees no significant change of the time the vacancy spends inside a cluster. After 1 min, this time starts to increase. After 30 min, when the value exceeds the value for vacancy binding to the surface of a cluster, the vacancy is mostly trapped inside a cluster.

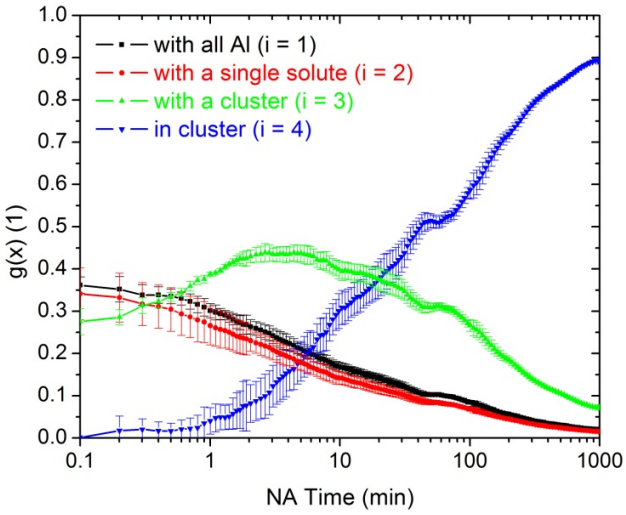

Figure 5.5. Frequency of the vacancy in specific environments. In the initial stage, vacancy either associates in all Al atoms or binds with a single solute while after longer NA time, the vacancy prefers to bind with a cluster or stay inside a cluster.

5.5. Position Changes between Vacancy and Atoms

During clustering, the vacancy diffuses by changing its position with one of its NNB atoms, which can be Al, Mg or Si. The fraction of time the vacancy changes its position with Mg, Si or Al is studied by using the same fraction function (Eq. 5.2) with i = 1: vacancy changing position with Si, i = 2: with Mg site and i = 3: with Al site, see Figure 5.6. Note that the vacancy always changes its sites in each step of the simulation, see Sec. 3.2.2.

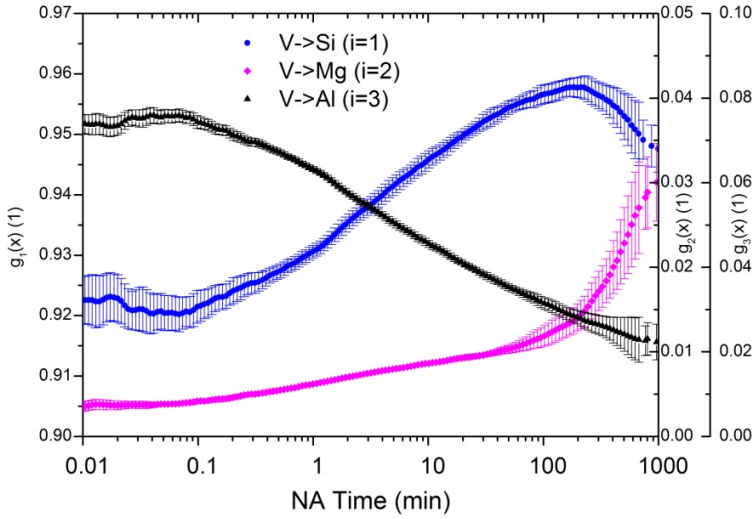

Figure 5.6. Frequency of the vacancy changing position with Si, Mg or Al. There is a high probability for the vacancy changing with the Si site. The probability of changing site with Mg increases after NA for 100 min. On the other hand, the probability of the vacancy changing site with Al monotonically decreases.

It is found that the vacancy changes its position mostly with Si, having a much higher time fraction than with Mg or Al. Although the Si/Mg ratio is 2.5 in 4-10, the probability of changing with Si is always 30 times higher than with Mg. This fraction starts to increase after it has passed a stage with a relatively constant value from the beginning to 0.1 min. The increase lasts for about 200 min and the fraction ends up with a decrease stage from 200 min to 1000 min. The fraction of time for the vacancy changing position with Mg is very low. It starts with a value of 0.005 and increase to 0.01 till 100 min of NA. However, after 100 min, a rapid increase of the frequency is found. At the end of the simulation, up to 0.035 of its time the vacancy changes position with Mg. In this final stage, the fraction of time the vacancy changes its position with one of the solutes (Mg, Si) has reached 0.99. In contrast, the time fraction the vacancy changes position with Al starts with the value of 0.08 and keeps constant till 0.1 min. A monotonic decrease of the probability is found till the end of the simulation showing that after long NA the vacancy rarely stays in the matrix.

5.6. Limitation of the Simulation on Clustering

The results of the simulation are given by the 12 input parameters listed in Table 3.4 and 3.5 that have been taken from literature. When these parameters vary, changes of the simulation

results are possible. For example, the vacancy formation energy (enthalpy and entropy) influences the physical time assigned to each Monte Carlo Step and also the jump frequency of atoms. The values varies between different sources, and in extreme cases, the physical time can expand or shrink by 2 orders of magnitude by changing the jump frequency of the atom. On the other hand, the size and composition of the clusters strongly depends on the interaction energies, see Eq. 3.5. A repulsive binding between vacancy and Mg with a different absolute value is found in Ref. 88, which would slow down the diffusion of Mg is accepted. Therefore in the simulation, in order to avoid an eclectic choice of parameters, all parameters were taken from two well-documented sources. Several studies [89, 90] speculate that in the early stage of clustering, Si clusters and Mg clusters develop firstly, after which they further evolve to Mg and Si co-clusters. However, this is not observed in this simulation because both Mg-Mg and Si-Si interaction energies are repulsive. As mentioned in Ref. 51, if the stress field influencing the mechanism of solute diffusion at the beginning is considered, Mg and Si clusters could form in earlier stage. This has not been implanted into the diffusion model yet.

5.7. Summary of Chapter 5

Through simulation, clustering stages have been observed during NA, those are:

Stage 1): From 0 to 2 min, fast formation of small clusters and a rapid increase of the solute fraction in clusters is observed. During this period, the vacancy spends most of its time in the Al matrix or with a single solute. When it changes its site, it prefers to change with Si, meaning that Si drives the kinetics of clustering in this stage.

Stage 2): From 2 min to 10 min, the increase of solute fraction slows down while the number density of cluster decreases. Big cluster starts to develop by consuming single solute or smaller clusters. The vacancy starts to be bind with clusters or is even sometimes temporarily trapped inside clusters.

Stage 3): From 10 min to 1000 min, the solute fraction is saturated while the number density of clusters decreases. Big clusters continue to develop, among which some of them have more than 60 solute atoms. The vacancy is mostly trapped inside the clusters and changes of position with Mg atoms become more frequent.

6. Discussion: Thermal Analysis

6.1. Kinetic Model of Clustering and Precipitation Process based on DSC Data

Thermal analysis based on DSC measurements provides information on macroscopic kinetics [54]. In order to understand the different stages of clustering and their effect on subsequent precipitation, the kinetics of clustering and precipitation in the alloy system has to be studied. In this work, isochronal DSC measurements at different heating rates were performed. A model-free method is first applied to obtain the effective activation energies, after which a specific reaction model is selected. Finally, the model is applied to obtain all the kinetics parameters.

Model-free analysis starts with the assumption that the transformation rate of a certain reaction is a product of two functions: one depends on the temperature T and the other on the transformation fraction α [54, 91]

$$\frac{d\alpha}{dt} = K(T)f(\alpha) \tag{6.1}$$

where $K(T) = K_0 \exp\left(-\frac{Q}{RT}\right)$ (6.2)

where K_0 is a constant with the unit s^{-1} and Q is the effective activation energy. The term "effective" used here expresses that Q a value derived from α, which, however, could be caused by various ractions. A range of $f(\alpha)$ have been proposed for different specific reaction functions [54, 91, 92]. Some are listed in Table 6.1. Among them, D1, D2 and D3 represent the functions for different dimensional diffusion in both solid and liquid, while R1, R2 and R3 refer to phase boundary controlled reactions. F1 or E1 are used for random nucleation with delay or chemical reaction, respectively. The most frequently function used for solid phase transformations is the Avrami-Erofeev equation (An), which can be incorporated with Johnson–Mehl–Avrami–Kolmogorov (JMAK) kinetics and is defined as

$$f(a) = n[-\ln(1-\alpha)]^{\frac{n-1}{n}}(1-\alpha) \tag{6.3}$$

Once Q, K_0 and $f(\alpha)$ or n in the JMAK kinetics have been obtained, the kinetics of the transformation can be fully described.

Table 6.1. Expressions of $f(\alpha)$ for some selected common mechanisms in solid-state reactions.

Mechanism	Symbol	$f(\alpha)$	Ref.
Reaction order model	Fn	$(1-\alpha)^n$	91, 92
Random nucleation and growth of nuclei (Avrami-Erofeev equation)	An	$n[-ln(1-\alpha)]^{\frac{n-1}{n}}(1-\alpha)$	93
1D diffusion (parabolic law)	D1	$\frac{1}{2\alpha}$	92, 93
2D diffusion (bidimensional particle shape)	D2	$\frac{1}{[-\ln(1-\alpha)]}$	92, 93
3D diffusion (tridimensional particle shape) Jander equation	D3	$\frac{3(1-\alpha)^{2/3}}{2[1-(1-\alpha)^{1/3}]}$	92, 93
3D diffusion (tridimensional particle shape) Ginstein-Brouhnstein equation	D4	$\frac{3}{2[(1-\alpha)^{-\frac{1}{3}}-1]}$	92, 93
Phase boundary controlled reaction (1st order)	R1	1	91
Phase boundary controlled reaction (2nd order: contracting cylinder)	R2	$(1-\alpha)^2$	91
Phase boundary controlled reaction (3rd order)	R3	$(1-\alpha)^{2/3}$	91
Exponential law	E1	α	91

6.1.1. Determination of the Effective Activation Energy Q

The analysis normally starts by obtaining the effective activation energy Q, as generally $f(\alpha)$ is unknown at the onset of the analysis. K_0 can only be obtained if Q and $f(\alpha)$ are determined. In general, two approaches are applied to obtain Q, the rate isoconversion and integration isoconversion methods. The different approaches in obtaining Q by these two methods are shown below.

a) Rate isoconversion method:

The rate isoconversion method involves first inserting Eq. 6.2 into Eq. 6.1 and taking the natural logarithm on both sides,

$$\ln\left(\frac{d\alpha}{dt}\right) = -\frac{Q}{RT_f} + \ln\left(f(\alpha)K_0\right), \tag{6.4}$$

where T_f is the temperature at which the transformed volume reaches a fixed fraction. When experiments with constant heating rate Φ are performed, Q can be obtained from the slope of $\ln(d\alpha/dt)$ versus $1/T_f$ by inserting Φ and rewriting Eq. 6.4 as

$$\ln\left(\frac{d\alpha}{dT}\Phi\right) = -\frac{Q}{RT_f} + \ln\left(f(\alpha)K_0\right). \tag{6.5}$$

b) Integration isoconversion method:

The integration isoconversion method is also called as generalized Kissinger method [91]. In this method, Eq. 6.2 is also inserted into Eq. 6.1 and but then integrates by separation of variables:

$$\int_0^\alpha \frac{d\alpha}{f(\alpha)} = \frac{K_0}{\Phi}\int_0^{T_f} exp\left(-\frac{Q}{RT}\right)dT = \frac{K_0 Q}{\Phi R}\int_{y_f}^{\infty}\frac{\exp(-y)}{y^2}dy, \tag{6.6}$$

where $y = Q/RT$, and $\mathrm{y_f} = \mathrm{Q/RT_f}$. By assuming $\mathrm{y}_f \gg 1$, the integral part $p(y)$ in Eq. 6.6 can be approximated as

$$p(y) \cong \frac{\exp(-y)}{y^2}. \tag{6.7}$$

Putting Eq. 6.7 into Eq. 6.6 and taking the natural logarithm on both sides,

$$\ln\int_0^\alpha \frac{d\alpha}{f(\alpha)} = \ln\left(\frac{K_0 Q}{R}\right) + \ln\left(\frac{1}{\Phi y_f^2}\right) - y_f. \tag{6.8}$$

Therefore, at a fixed fraction of transformation, Eq. 6.8 becomes,

$$\ln\left(\frac{\Phi}{T_f^2}\right) = -\frac{Q}{RT_f} + C_2, \tag{6.9}$$

where C_2 is a parameter that is independent of T and Φ. It should be noted that when using the temperature at maximum transformation rate T_p instead of T_f, Eq. 6.9 yields the original Kissinger method [94].

Before Q is obtained by the two methods, the volume fraction α is determined by

$$\alpha = \frac{\int_{T_0}^{T_s}(H-H_0)dT}{\int_{T_0}^{T_e}(H-H_0)dT}, \tag{6.10}$$

where $\int_{T_0}^{T_s}(H-H_0)dT$ is then the heat effect from the onset temperature T_0 up to a given temperature T_s and $\int_{T_0}^{T_e}(H-H_0)dT$ is the total heat effect of the whole reaction during the DSC run.

6.1.1.1. Effective Activation Energy Q for clustering

After obtaining α, both methods are then applied to obtain Q for the clustering peaks of 4-10 directly after SHT. The corresponding analysis is shown in Figure 6.2. From the slopes of the linear fit, Q at different fractions of transformation is obtained for alloy 4-10 after SHT and is given in Figure 6.3.

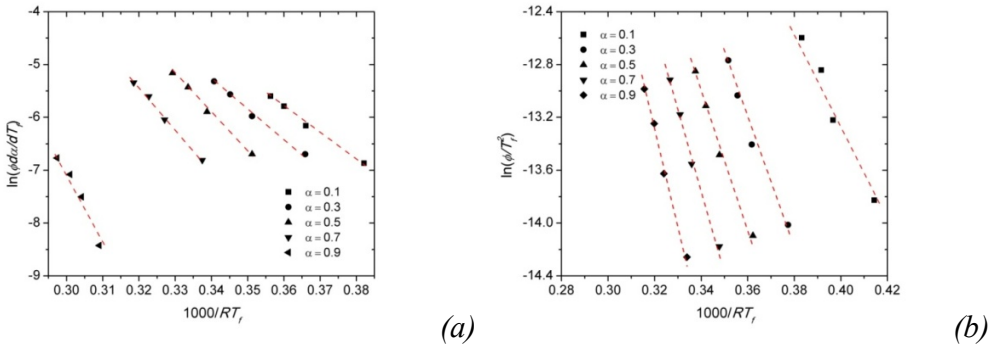

(a) *(b)*

Figure 6.2. Examples of plots of (a) $\ln\left(\frac{d\alpha}{dT_f}\right)$ *vs.* $1000/RT_f$ *and (b)* $\ln\left(\frac{\Phi}{T_f^2}\right)$ *vs.* $1000/RT_f$ *to obtain* Q *by the rate isoconversion and integration isoconversion methods, respectively.*

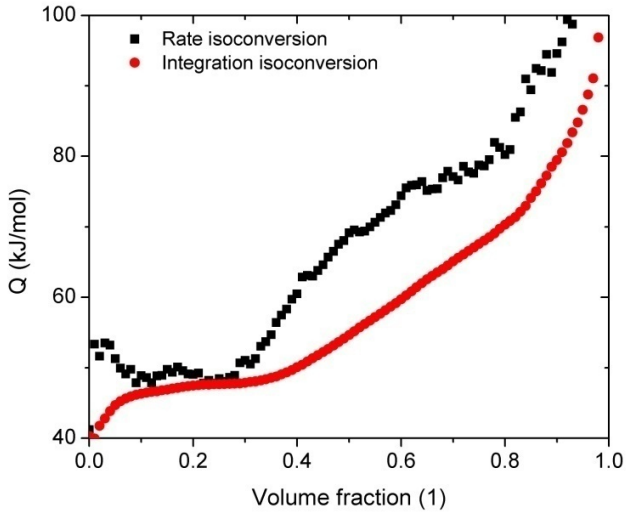

Figure 6.3. Q for clustering after SHT in alloy 4-10 obtained by different methods. It shows that by both methods, an increase of Q is found.

Both methods predict that Q starts with a low value of ~50 kJ/mol. No pronounced change of the value of Q is observed till the clusters have transformed to ~0.3 fraction. Then Q increases rapidly in both methods and ends with a value of ~100 kJ/mol. However, the Q values obtained by the rate isocoversion method fluctuate more, especially at the beginning and in the end of the transformation. Moreover, after the transformation has reached 0.3, the value of Q obtained by the rate isocoversion method are about 5 –10 kJ/mol higher than by the integration isocoversion method at the same fixed transformed fraction. Though the rate isoconversion method avoids mathematical approximation, the value of $\mathrm{d}\alpha/\mathrm{dt}$ is very sensitive to the baseline as the slope of the baseline of the heat flow is also counted during linear fitting from which the slope yields to Q. This could be the reason for the fluctuation and the higher values of Q. On the other hand, the integration isocoversion method brings other possible error. For example, when $y = Q/RT < 20$, which is for the onset of the clustering reaction T=303.15K, meaning Q < 48 kJ/mol, the error caused by the approximation of the integral will be markedly increased [94].

As both methods provides Q in the same range while the results fluctuate less in the integration isocoversion method, only the latter will be used and discussed in the following study. Q is shown only for the volume fraction ranging from 0.1 to 0.8 due to the fact that outside this range the inaccuracy on Q cannot be neglected [95]. The clustering reaction in 4-10 and 4-10X is similar, but 4-10X shows a smaller heat effect, as shown in Figure 4.10. The weak DSC signal for

4-10X would bring significant error for the kinetics study. Therefore, only DSC results for 4-10 is used for the analysis.

The increasing Q according to the volume fraction of clustering, see Figure 6.3, indicates that several parallel reactions are involved [96]. Thus, the Q for clustering in 4-10 after SHT without NA, with NA for 100 min and 1000 min is calculated and given in Figure 6.4.

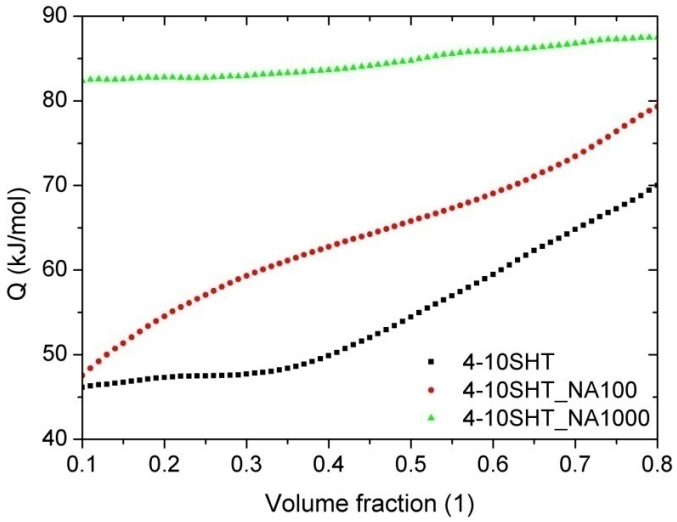

Figure 6.4. Changes of Q for clustering as a function of volume fraction in alloy 4-10 after SHT without and with prior NA for 100 min and 1000 min. The result for sample directly after SHT is taken from Figure 6.3.

Recall from Figure 4.10 and from Figure 6.4, that the sample without NA shows three clustering peaks and its Q value starts from a low value of ~50 kJ/mol and keeps fairly stable until the fraction of cluster transformation is 0.3. After this, Q increases to ~70 kJ/mol until the volume fraction reaches 0.8. When the sample is NA for 100 min, the 1st clustering peak has become very weak and the other 2 peaks are more significant. In this case, Q starts with a slightly higher initial value than the sample without NA. No constant value for Q is observed but a continuous increase until Q reaches 80 kJ/mol. Only the 2nd and 3rd peaks are observed in the sample NA for 1000 min, as shown in Figure 4.10. The Q value corresponding to 2nd and 3rd peak is stable with only a slight increase from 82.5 kJ/mol to 86 kJ/mol. Therefore, from the above results, the 1st clustering process is a process with a low Q while the 2nd and 3rd are processes with a high and similar Q.

6.1.1.2. Effective Activation Energy Q for β" formation

As shown in Figure 4.6, the formation peak of β" in 4-10 exhibits a shoulder which could be caused by either an alternative diffusion path during β" formation or by the formation of other kind of precipitate. In order to obtain Q by using the integration isoconversion method that has been used previously for clustering and due to the uncertainty on the reaction type of the shoulder position, the β" reaction including the shoulder is deconvoluted into two Gaussian functions within the temperature range from 200 ^{o}C to 280 ^{o}C by using the program Peak Analyzer in Origin pro 8.5. The procedure is demonstrated in Figure 6.5.

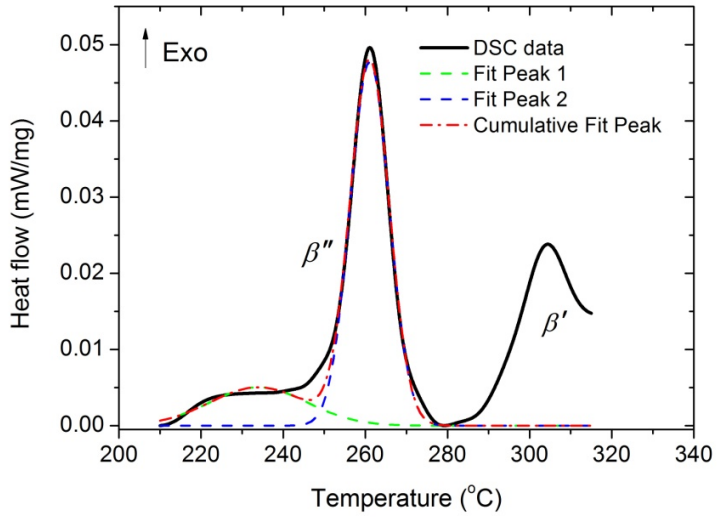

Figure 6.5. Gaussian fitting for the overlapping precipitation peaks in alloy 4-10 in the DSC trace obtained directly after SHT. Part of the β′ peak is also shown.

The fitted peak 2, as shown in Figure 6.5, is then used for calculating Q for the formation of β". The calculated Q for β" formation of 4-10 and 4-10X after SHT is given in Figure 6.6.

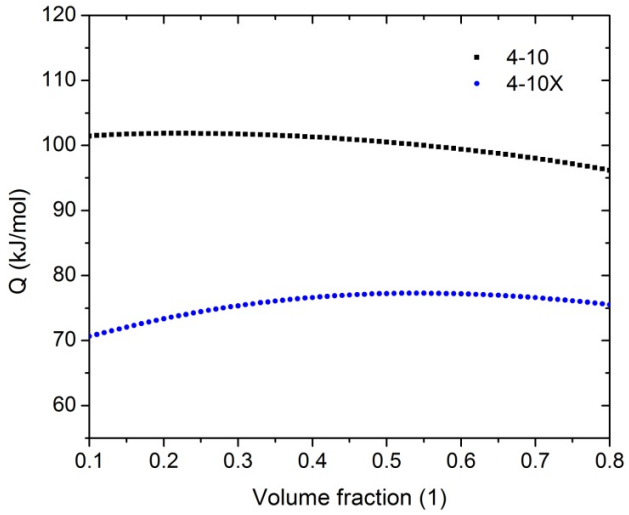

Figure 6.6. Q for the formation of β" in alloys 4-10 and 4-10X directly after SHT. 4-10 always has higher Q than 4-10X. The change of Q with volume fraction in both alloys are not significant.

The calculated Q values for the β" formation is significantly different in both alloys, which is ~125 kJ/mol in 4-10 and ~74 kJ/mol in 4-10X. This indicates that the formation kinetics of β" in these two alloys is different, though they have the same Mg and Si content. Compared with Q for clustering, it is found that the Q values for β" are very stable during the whole transformation, i.e. only with a slight decrease of ~5 kJ/mol in 4-10. Therefore a single Q value obtained by the original Kissinger method, i.e. only considering the maximum transformation rate is enough to be representable for the whole process. The value of Q at the maximum transformation rate for 4-10 and 4-10X without NA and with NA for 100 min is given in Table 6.2. Compared to the sample without NA, no significant influence on the Q is found in both alloys after NA for 100 min, though shifting of the peak temperature T_p is found, see Figure 4.17.

Table 6.2. Q for β" at the maximum transformation rate for 4-10 and 4-10X, with and with NA.

Alloy	Q (kJ/mol)
4-10SHT	105 ± 6
4-10SHT_NA100	113 ± 7
4-10XSHT	75 ± 1.6
4-10XSHT_NA100	77 ± 1.5

6.1.2. Determination of $f(\alpha)$

The JMAK equation (An) as shown in Eq. 6.3 is most popular in describing the precipitation process in Al alloys [97, 98]. Specifically for β", the n value in the JMAK equation is often found to be between 2 and 2.5 [30, 69]. However the $f(\alpha)$ for the clustering process is rarely discussed. Gupta and Lloyd [14] have used $f(\alpha) = 1 - \alpha$, which corresponds to the case of n =1 in the JMAK equation, but without further explanation. Therefore, two tasks are involved in this section: 1) to determine $f(\alpha)$ for clustering, 2) to determine the n value for the formation of β" and clustering, if clustering can also be described by the JMAK equation.

By the rate isoconversion method, the intercept of the linear fit for obtaining Q according to Eq. 6.5 is equal to $\ln(f(\alpha)K_0)$. Once $f(\alpha)$ has been determined, the corresponding K_0 is obtained from the y-intercept shown in Figure 6.2a. Hence, if the kinetics triplets Q, $f(\alpha)$ and K_0 are known, the fraction transformed as a function of time t or temperature T is described by Eq. 6.1. The required Δt_i for the change of the discretised volume fraction from α_{i-1} to α_i ($i \geq 1$) can be obtained by converting Eq. 6.1 to,

$$\Delta t_i = \frac{\alpha_i - \alpha_{i-1}}{K(T_i) f(\alpha_i)}. \quad (6.11)$$

Therefore, the time t_i required for the volume fraction reaches α_i from 0 is,

$$t_i = \sum_{j=1}^{j=i} \Delta t_j. \quad (6.12)$$

Different functions $f(\alpha)$ are chosen to check their suitability to describe the clustering reaction, namely 1) the Avrami-Erofeev equation (code: An), with n starting from 1 to 3 in steps of 0.1; 2) The 2D diffusion Jander Equation (two-dimensional particle shape) (code: D2); 3) 3D diffusion Jander Equation (three-dimensional particle shape) (code: D3) and 4) 3D diffusion Ginsten-Brouhnstein Equation (three-dimensional particle shape) (code: D4). Then K_0 is obtained from the y-intercept as shown in Figure 6.2a and Q is obtained by the from rate isoconversion method. By using Eq. 6.12, the time t for different α during clustering at RT (e.g. =25 ^{o}C) for alloy 4-10 after SHT is calculated and shown in Figure 6.7.

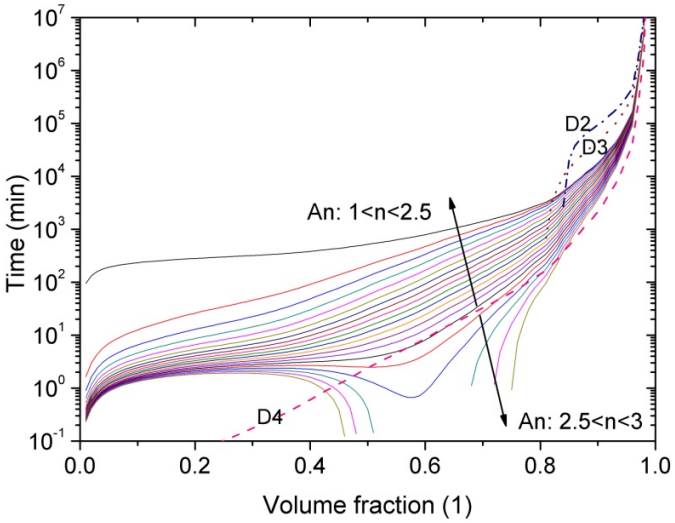

Figure 6.7. Relationship between volume fraction α and time t at T="RT" for the clustering process of 4-10 directly after SHT using different f(a). Q and K_0 are obtained from experimental values. Solid lines are An with the directions of the two arrows indicating increasing/decreasing n value in the ranges of 1< n <2.5 and 2.5 <n <3. D2, D3 and D4 and are presented by the dash-dotted, dotted and dashed lines, respectively.

When $\alpha < 0.8$ no positive value of K_0 can be obtained by using D2 and D3 for $f(\alpha)$. Therefore the corresponding α-t relationship cannot be obtained. This is also true when using D4 for $\alpha <$ 0.25. Therefore D2, D3 and D4 cannot be used to describe the clustering kinetics in this case. The JMAK kinetics shows sigmoidal behaviour and the full α - t relationship with α ranging from 0 to 1. Therefore, it is reasonable to use An with $n \leq 2.5$ to describe the clustering kinetics. When $n > 2.5$, t decreases with increasing α when α is in the range of 0.4 – 0.8, which is unphysical. This is because K_0 is also negative when $0.4 < \alpha < 0.8$. Therefore it is concluded that only JMAK kinetics with $n \leq 2.5$ can express the clustering kinetics in our system.

The next question is which n value should be chosen to describe the clustering and precipitation reaction. The JMAK kinetics starts from [54]

$$\alpha = 1 - \exp(-\omega^n), \tag{6.13}$$

where in the isothermal reaction:

$$\omega = K(T)t \tag{6.14}$$

and in the isochronal reaction:

$$\omega = \int K(T)dt. \tag{6.15}$$

Combining Eq. 6.13 and Eq. 6.1 yields,

$$\frac{d\alpha}{dt} = K(T)n\omega^{n-1}\exp(-\omega^n) = K(T)n[-\ln(1-\alpha)]^{\frac{n-1}{n}}(1-\alpha) \tag{6.16}$$

Eq. 6.16 is equivalent to inserting Eq. 6.3 into 6.1.

Eq. 6.13 becomes

$$-\ln(1-\alpha) = \omega^n \tag{6.17}$$

then further convert to

$$\ln(-\ln(1-\alpha)) = n\ln\big(K(T)\big) + n\ln t. \tag{6.18}$$

In a single process, both $K(T)$ and n are constant, therefore n can be obtained by the slope of the straight line when plotting $\ln(-\ln(1-\alpha))$ as a function of $\ln t$ as [99]:

$$\frac{d(-\ln(-\ln(1-\alpha)))}{d\ln t} = n. \tag{6.19}$$

In a reaction which involves more than one process, n changes with $\alpha(T)$. By the approximation methods for obtaining n [100], Eq. 6.18 becomes:

$$\frac{d(-\ln(-\ln(1-\alpha_{\Phi}(T))))}{d(\ln(\Phi))} = n(T). \tag{6.20}$$

$\alpha_{\Phi}(T)$ is the volume fraction at a specific temperature (T=95 ^{o}C) under a certain heating rates Φ (5, 10, 15 and 20 K/min). By Eq. 6.20, n is obtained by the value of the slope from of $-\ln(-\ln(1-\alpha(T)))$ versus $\ln(\Phi)$, as shown in Figure 6.8.

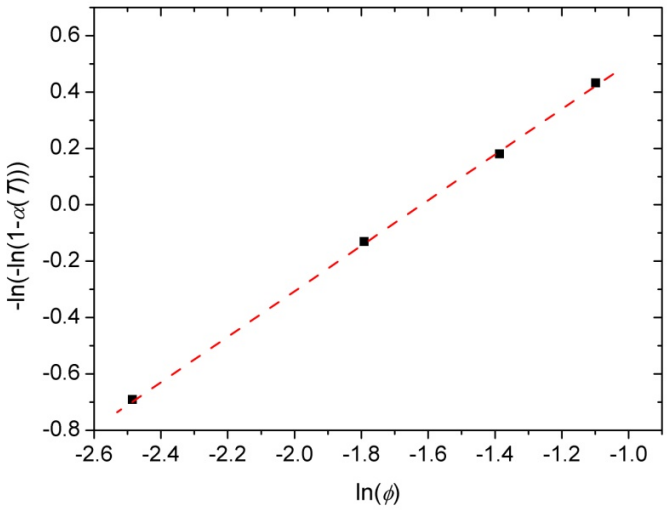

Figure 6.8. Example of the plot of $-ln(-ln(1-\alpha(T)))$ vs. $ln(\Phi)$. The experimental data shows a linear relationship and n can be obtained from the slope of the straight line. In this case, $n = 0.8$.

The n values obtained from Eq. 6.20 for the formation of clusters in 4-10 and β" in 4-10 and 4-10X directly after SHT, are given in Figure 6.9.

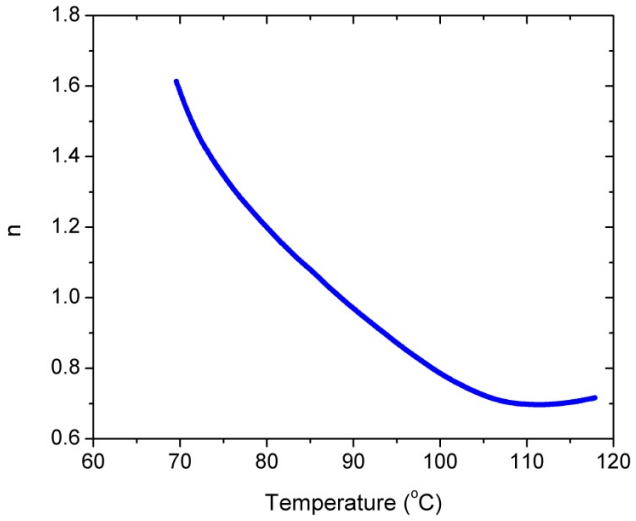

(a)

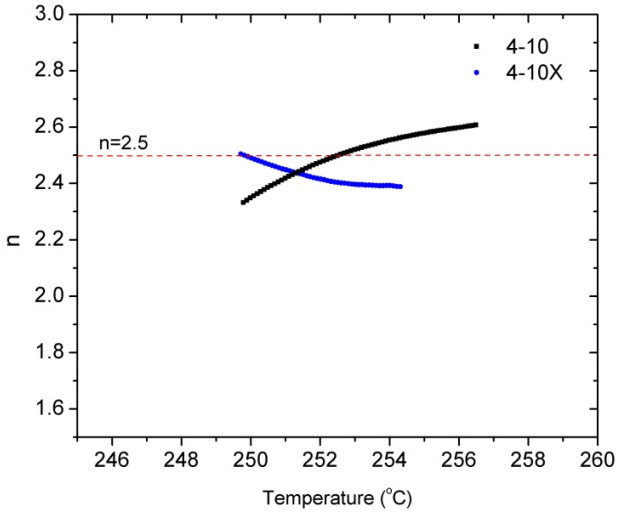

(b)

Figure 6.9. n obtained as a function of temperature from Eq. 6.20 for (a) clustering in 4-10 and (b) formation of β" in 4-10 and 4-10X directly after SHT. n decreases with T when $0.8 < n < 1.6$ for clustering, while it stays close to ~2.5 for the formation of β".

As can be seen from the figure, there is only a limited range of T where n can be determined, although the clustering or β" formation peaks cover a much wider range in the experimental data. This is because the formation peaks during isochronal measurements shifted to higher temperatures with increasing heating rates, and only the T range with $f(T)$ not too close to 0 or 1

for all the heating rates can be used to obtain n. Therefore, although the temperature range covered by the clustering peak is much broader, the value of n for clustering can only be obtained from 70 to 120 ^{o}C, as revealed in Figure 6.9a. Nevertheless, n starts from ~1.6 and decreases to ~0.8 with increasing T. For the formation of β", as the shift of the peak during isochronal measurements is more pronounced, n can only be obtained in a narrow T range of 250 to 258 ^{o}C for both alloys and it lies in the range of 2.3 to 2.6.

Table 6.3 shows the correspondence of n values to different mechanism as discussed in the literature. The n values for clustering obtained from above analysis first matches the mechanism of nucleation with pre-existing nuclei and decreasing rate and later the mechanism of particle growth of appreciable initial volume. In contrast for β", the n values are very close to that for the typical mechanism of continuous nucleation and growth (2.5) [99, 101]. From the above analysis the ranges of n for clustering and β" formation are known. However as the n values obtained do not cover the whole temperature range of the reaction for different heating rates, therefore the n values here can only be used as reference value for the following modelling analysis.

Table 6.3. Correspondence between n and mechanism found in the literature [99, 101]

Mechanism	n
All shapes growing from small dimensions, increasing nucleation rate	$> 2\frac{1}{2}$
All shapes growing from small dimensions, constant nucleation rate	$2\frac{1}{2}$
All shapes growing from small dimensions, pre-nuclei + decreasing nucleation rate	$1\frac{1}{2} - 2\frac{1}{2}$
All shapes growing from small dimensions, site saturation, zero nucleation rate	$1\frac{1}{2}$
Growth of particles of appreciable initial volume	$1 - 1\frac{1}{2}$
Needles and plates of finite long dimensions, small in comparison with their separation	1
Thickening of long cylinders (needles) (e.g. after complete end impingement)	1
Thickening of very large plates (e.g. after complete edge impingement)	$\frac{1}{2}$
Precipitation on dislocations (very early stages)	$\sim\frac{2}{3}$

6.1.3. Summary

From generalised the Kissinger method, Q for clustering and formation of β" are obtained. The Avrami-Erofeev model (JMAK model) is chosen for describing $f(\alpha)$ for both clustering and formation of β". According to the JMAK model, n has found to be in the range of 0.8-1.6 and 2.0-2.6 for clustering and formation of β", respectively. Until now a precise description of the formation kinetics of clustering and β" has not established because the values of n and K_0 according to the changes of the volume fraction α were unknown. Nevertheless, by the information obtained above (knowing the range of Q, n and K_0), modelling the kinetics by appropriate selection of a set of equations becomes possible.

6.2. Kinetic Parameters obtained by Modelling

6.2.1. Introduction of the Kinetic Model

If a transformation can follow the kinetics of random nucleation and isotropic growth to dimension m (m =1, 2, 3), then the volume fraction $\alpha(t)$ is defined as [102]:

$$\alpha(t) = 1 - \exp[-\int_0^t v(t,\tau)\, I(\tau) d\tau]. \quad (6.21)$$

The argument of the exponential function is the so-called extended volume $\alpha_{ext}(t)$, which consists of an integral for all the nucleation times τ from 0 to t. The integral is a product of the nucleation rate $I(\tau)$ and the volume caused by the growth of the nucleation sites $v(t,\tau)$ formed. When m -dimensional growth is assumed, $v(t,\tau)$ is defined as [102]:

$$v(t,\tau) = g[\int_\tau^t Y(\mu)\, d\mu]^m, \quad (6.22)$$

where g is the geometric factor which relates to the shape of the particle, $Y(\mu)$ means the growth rate at time μ of all the m dimensions. Both the nucleation rate $I(t)$ and growth rate $Y(t)$ are assumed to follow an Arrhenius dependence:

$$I(t) = I_0 \exp\left(-\frac{Q_n}{RT}\right) \text{ and} \quad (6.23)$$

$$Y(t) = Y_0 \exp\left(-\frac{Q_g}{RT}\right), \quad (6.24)$$

where I_0 and Y_0 are the nucleation and growth constants respectively, $Q_n$and Q_g are the activation energies for nucleation and growth, respectively.

6.2.1.1. Isothermal Kinetics

For the isothermal case, Eq. 6.21 yields [102, 103]:

$$\alpha(t) = 1 - \exp\{-[K(T)t]^n\} \tag{6.25}$$

with $n = m + 1$, (6.26)

$$K(T) = K_{eff}\exp\left(-\frac{Q_{eff}}{RT}\right), \tag{6.27}$$

$$K_{eff} = \left(\frac{g}{m+1}Y_0^m I_0\right)^{\frac{1}{m+1}}, \tag{6.28}$$

with the effective activation energy Q_{eff} given as:

$$Q_{eff} = \frac{mQ_g+Q_n}{m+1} \tag{6.29}$$

6.2.1.2. Isochronal Kinetics

When a constant heating rate Φ is applied, the expression for $\alpha(t)$ can be rewritten to [103]:

$$\alpha(t(T)) = 1 - \exp\{-[\frac{K_{eff}}{\Phi}\int_0^{T(t)}\exp\left(-\frac{Q_{eff}}{RT'}\right)dT']^n\}. \tag{6.30}$$

Similar to the approximation used in the integration isoconversion method, Eq. 6.30 finally yields [103]:

$$\alpha(T) = 1 - \exp\{-[\frac{K_{eff}Texp(-\frac{Q_{eff}}{RT})}{\Phi\frac{Q_{eff}}{RT}}]^n\}. \tag{6.31}$$

Therefore $\alpha_{ext}(T)$ becomes:

$$\alpha_{ext}(T) = \left(\frac{K_{eff}Texp\left(-\frac{Q_{eff}}{RT}\right)}{\Phi\frac{Q_{eff}}{RT}}\right)^n. \tag{6.32}$$

6.2.1.3. Impingement for Isochronal Measurements

The JMAK kinetics is valid only in: 1) randomly distributed phases with independent growth of different phases; 2) isotropic linear or parabolic growth; 3) constant equilibrium state [104]. When a part of the transformation (though it is under the mechanism of nucleation and grow) is not fully described by JMAK kinetics, an impingement expression should be applied, which improves the better description together with JMAK kinetics. Now, $\alpha(T)$ with impingement becomes [104]:

$$\alpha(T) = 1-(\frac{\alpha_{ext}(T)}{\eta} + 1)^{-\eta}, \quad (6.33)$$

where η is so-called the impingement factor.

6.2.1.4. Adaptation of Multiple Processes or Overlapping Reactions into the Model

As shown in Figure 6.4, increasing Q with α for the clustering reaction is observed in the samples without NA and NA up to 1000 min. This indicates that multiple processes occur simultaneously during NA leading to a mixing product of Q for the different processes [105]. From Figure 4.6, the formation of β" first starts with a shoulder in 4-10. Also, the overlap of the β" and β' peaks become more severe when samples are after NA, see Figure 4.17a. Therefore, multiple processes or overlapping transformations have to be considered in the model.

a) Multiple Processes (Clustering)

Assuming that the processes in clustering occur in parallel with each other and their interactions are negligible, an elementary model which combines z processes is applied [106], in isochronal:

$$\alpha(T) = \sum_{i=1}^{i=z} c_i a_i(T), \quad (6.34)$$

while in isothermal:

$$\alpha(t) = \sum_{i=1}^{i=z} c_i a_i(t), \quad (6.35)$$

where c_i is the contribution factor of the i^{th} process and satisfies $0 \leq c_i \leq 1$ and $\sum_{i=1}^{i=z} c_i = 1$.

b) Overlapping reactions (β" formation):

The measured heat flow H at T for a single formation is given as:

$$H(T) = A\frac{d\alpha(T)}{dT}, \tag{6.36}$$

where A is a constant related to heat flow. Therefore, if k formations involved during the DSC run, $H(T)$, is expressed as:

$$H(T) = \sum_{i=1}^{i=k} A_i \frac{d\alpha_i(T)}{dT}. \tag{6.37}$$

It should be noted that Eq. 6.34 can be converted to 6.37 by differentiation and introducing A for each process. However, due to the fact that clustering are processes which have the same enthalpy per unit, using Eq. 6.33 instead of 6.36 can reduce the number of fitting parameter by one.

6.2.1.5. Fitting Procedure for Modelling

In general, Q_{eff}, K_{eff} and n are obtained by the best fit from Eq. 6.34 for clustering and Eq. 6.37 for β" formation, using the experimental data measured under different heating rates Φ. The fitting procedure starts with the initial values of Q_{eff}, K_{eff} and n. The initial value of Q_{eff} is taken from that calculated by the integration isoconversion method and is allowed to accommodate within a given range of Q ± 20 kJ/mol. The aim is to find the smallest mean square error e for the volume fraction $\alpha(T)$ in clustering or the heat flow $H(T)$ in β" formation for all heating rates Φ. The mean square error e in fitting is defined as:

$$e = \sum_{i=1}^{i=4} \sum_{all\ datapoints} \left(\frac{\alpha_{DSC}(T_i) - \alpha_{model}(T_i)}{\alpha_{DSC}(T_i)}\right)^2 \tag{6.38}$$

and

$$e = \sum_{i=1}^{i=4} \sum_{all\ datapoints} \left(\frac{H_{DSC}(T_i) - H_{model}(T_i)}{H_{DSC}(T_i)}\right)^2 \tag{6.39}$$

for clustering and β" formation, respectively and i = 1, 2, 3 and 4 correspond to the heating rate Φ of 5, 10, 15 and 20 K/min.

Due to the fact that, the impingement factor η is mostly considered an adjustable parameter but no theoretical justification can be provided [104, 107, 108, 109], η is fixed to 2 for all the fitting. In this work this represents a weak impingement factor [104].

6.2.2. Modelling Results

6.2.2.1. Clustering

Although three processes are observed in the DSC curves as shown in Figure 4.10, only two processes are considered in this model. This is because when the 1st process is finished, see Figure 6.4, the Q values for 2nd and 3rd reactions are very stable with increasing α, which means that they can share one set of kinetic parameters. By this simplified treatment, fewer fitting parameters are introduced in the model. Figure 6.10 shows the fitting results for alloy 4-10 after different NA time by using Eq. 6.32, 6.33 and 6.34. It can be calculated from the quality of the fitting that the model is appropriate to describe the clustering processes. The fitted parameters are listed in Table 6.3

Table 6.3. Kinetic parameters of clustering from the model after fitting. The numbers highlighted in grey are fixed when fitting samples which have been NA.

Alloy	1st clustering			2nd +3rd clustering			
	Q_{eff}^1 (kJ/mol)	K_{eff}^1 ($\times 10^5$ s^{-1})	n_1	Q_{eff}^2 (kJ/mol)	K_{eff}^2 ($\times 10^8 s^{-1}$)	n_2	c_1
4-10	50	7	1.8	79	9.1	1.1	0.67
4-10NA 100	50	7	1.8	79	9.1	1.1	0.08
4-10NA 1000	-	-	-	79	9.1	1.1	0

The kinetics of clustering is now fully described by the parameters. Considering results from 4-10 which was without NA, clustering starts with a low Q_{eff} value of 50 kJ/mol. n for the 1st process is found to be 1.8, which lies into the range for the corresponding mechanism of continuous nucleation plus some pre-existing nuclei [99, 100]. This agrees with the KMC simulation results that a large amount of dimers already exist in the randomly generated system due to the high concentration of solutes, as shown in Figure 5.1a and b. For the 2nd and 3rd clustering processes, Q_{eff} increases to 79 kJ/mol and n = 1.1, indicating that the process is slow and the corresponding n value is similar to that for particles growth [99]. In the KMC simulation, big clusters are formed by coagulation in the later stage of clustering. This process is slow and, again, agreement with the kinetic parameters found from DSC modelling is found.

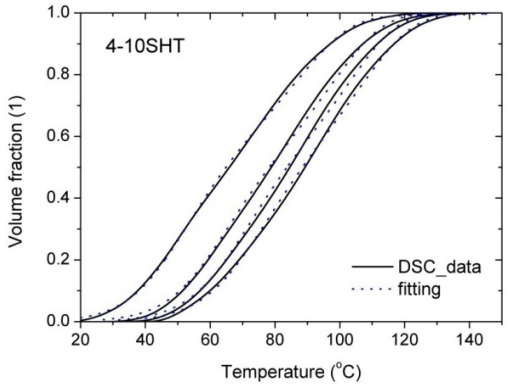

(a)

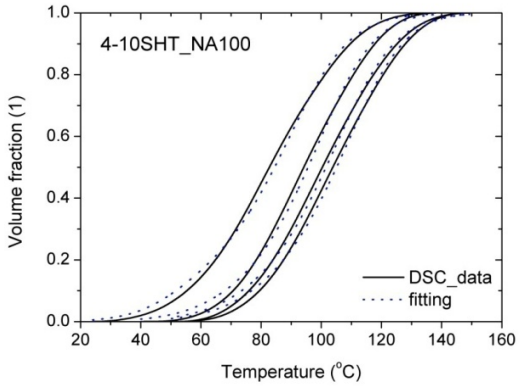

(b)

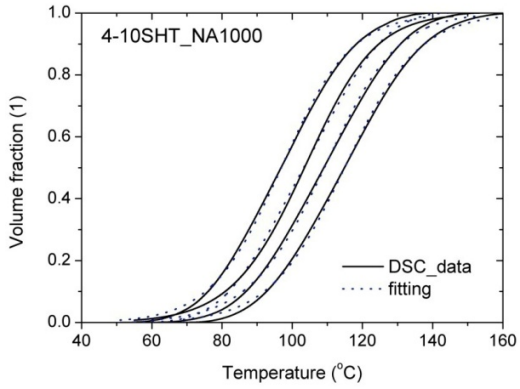

(c)

Figure 6.10. Fitting of $\alpha(T)$ vs. T for the clustering reaction in alloy 4-10 (a) without NA, (b) after NA for 100 min and (c) after NA for 1000 min. The experimental data and the fitted results are shown for different heating rates (heating rates from left to right: 5, 10, 15 and 20 K/min).

When fitting the results for samples with NA, Q_{eff}, K_{eff} and n are fixed and set to be the same as that of the sample without NA and they are highlighted in grey in Table 6.3. Therefore, only c_1, which corresponds to the contribution of the 1st clustering process, is allowed to vary. After NA

for 100 min, c_1 decreases to a value of 0.08, showing that the contribution of the 1st clustering process has become very weak. This indicates that the process has largely been accomplished at this time.

6.2.2.2. Formation of β"

The fitted results for the formation of β" using Eq. 6.32, 6.33 and 6.37 together with its neighbouring precipitation reaction(s) are plotted in Figure 6.11. The kinetics parameters for the formation of β" obtained after fitting is given in Table 6.4.

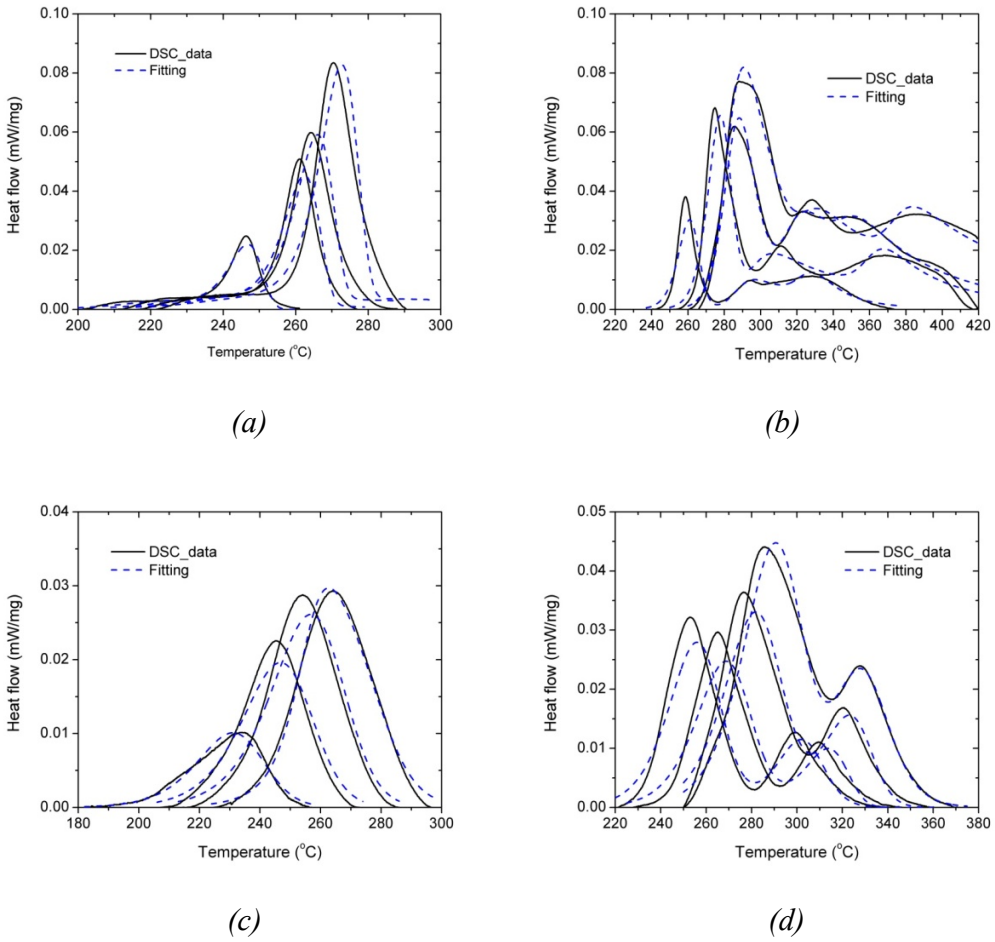

Figure 6.11. H vs. T curves for the formation of β"of (a) alloy 4-10 without NA,(b) 4-10 NA for 100 min, (c) 4-10X without NA and (d) 4-10X NA for 100 min. The experimental data and the fitted results are plotted together with different heating rates (from left to right: 5, 10, 15 and 20 K/min).

Table 6.4. Kinetics Parameters for the formation of β"obtained by fitting.

Sample	Q_{eff} (kJ/mol)	K_{eff} (s^{-1})	n
4-10	120	1.8×10^{10}	2.5
4-10NA100	118	3.1×10^{9}	2.5
4-10X	85	1.3×10^{6}	2.5
4-10XNA100	85	5.3×10^{5}	2.5

Though 4-10 and 4-10X have the same nominal Mg and Si compositions, the kinetic parameters for the formation of β" are different. First of all, n is found to be 2.5 for all samples, indicating that continuous nucleation and diffusion controlled growth is the major mechanism governing the formation of β" no matter clusters exist or not. Second, the Q_{eff} and $K_{eff}$of 4-10 directly after SHT are 120 kJ/mol and $1.8\text{x}10^{10}$ s^{-1} respectively, which are higher than in 4-10X in the same condition. When comparing the morphology of the precipitates shown in Figure 4.13, the higher Q_{eff} and K_{eff} are related to a higher number density of precipitates but with a slower growth rate. After NA for 100 min, no significant changes of Q_{eff} in both alloys is found, but K_{eff} is lowered by one order of magnitude, indicating that the energy required for the reaction is similar but the formation rate is slower.

6.3. Summary of Chapter 6

In this chapter, the kinetic parameters required to fully describe both clustering and formation of β" are determined by a kinetic model. Two major parallel processes occurred during clustering: (1) the 1st clustering process has low Q_{eff} (50 kJ/mol) and K_{eff} (7×10^{5} s^{-1}) values and n = 1.8, expressing that the mechanism of this process is similar to that for site saturation and continuous nucleation. The process is attributed to a fast process which is easily stimulated; (2) combined 2nd + 3rd clustering process has higher Q_{eff} and K_{eff} values and n = 1.1, which points at the that the mechanism similar as particle growth. This process is much slower than the 1st process. Although the mechanism for the formation of β" in 4-10 and 4-10X is the same, as n obtained for both alloys is 2.5 (i.e. constant nucleation without site saturation), the values of Q_{eff} and K_{eff} in 4-10 are higher than 4-10X. No significant change of the value of Q_{eff} is found in the samples after

NA, but K_{eff} decreases in both alloys. Also, NA does not influence the mechanism of β" formation.

7. Discussion: All Results

7.1. Mechanism of Clustering during NA

7.1.1. Role of Vacancies during Clustering

As a sample is quenched from an elevated temperature, a large amount of vacancies are retained so the number of vacancies exceeds the equilibrium value at the final temperature. Still, the concentration of the vacancies is two or more orders of magnitude lower than that of the solute atoms in the alloy. When comparing the number of clusters to that of the solutes and vacancies, the question of the mechansim of vacancy diffusion must be raised. Girifalco et al. [110] have introduced the vacancy pump model to describe the role of vacancies during GP zone formation. In their model, the formation of GP zones is first assisted by diffusion of a vacancy-solute complex to a GP zone, after which the vacancy diffuses back into the matrix because of the change of the vacancy gradient. The next cycle starts again by formation of a new vacancy-solute complex.

The clustering process in 6xxx Al alloys is believed to be driven by the diffusion of quenched-in vacancies [40, 41, 48, 53]. In alloy 4-10, the solute concentration in the SSSS is $\sim 1.4\times10^{-2}$. However, the vacancy concentration calculated from Eq. 3.8 is only 1.41×10^{-4}, which is two orders of magnitude less than the solute concentration. Only one vancay is present in the KMC simulation. At the beginning of the KMC simulation, ~0.35 of the vacancies bind with one single solute and ~0.27 are staying at the interface between cluster and matrix, see Figure 5.5. Later, the fraction of solutes in the clusters increases significantly, see Figure 5.2. For this to happen, vacancies have to diffuse back into the matrix either to form more clusters or to bring more solutes into the clusters. This is supported by the high fraction of free vacancies or vacancy-cluster complexes, each ~0.35. The consequence is that the fraction of solutes in clusters increases up to ~58% as shown in Figure 5.2. The mechanism of what is observed in the initial stage of the KMC simulation is in accordance with the vacancy pump model.

Through the clustering process, more and more clusters are formed and therefore more solutes are now in the clusters. This also means that the solute concentration in the matrix is reduced. Keeping in mind that the interactions of vacancy–Mg and vacancy–Si are attractive, see Table 3.4, the clusters formed can act as vacancy sinks because there more direct neighbours of

solutes exist to which vacancies can bind with. Meanwhile, vacancy "pumping" back to the matrix becomes more difficult. Therefore, at this stage, some of the vacancies are likely to be 'trapped' by bigger clusters for a longer time rather than performing the "pump" effect to transfer single solute from the matrix. Here, 'trapping' means that diffusion occurs either at the interface or inside the clusters. This is reflected by Figure 5.5 because, after a short period of NA time, the frequency of vacancies staying at the matrix-cluster interface increases up to ~45%, while the frequency of vacancy-solute complex or vacancy in the matrix decreases. This opens up a new possibility of further reducing the system energy by moving the whole clusters, consuming either other isolated solutes or clusters, since when the vacancy is next to the cluster or in the cluster, the mobility of the cluster increases. When clustering proceeds in this way, coagulation will occur [56, 58, 111].

In order to check whether coagulation happens during the later stages of clustering, the average diameter (d of clusters with more than 15 atoms and assuming spherical shape are calculated and plotted on a logarithmic scale as a function of the logarithm of time, as shown in Figure 7.1. Linear fitting is applied to the results and a time exponent obtained with a value of 0.15, i.e. $d \propto t^{0.15}$, which is very close to that obtained for coagulation (1/6) [56, 58, 111] of clusters in a binary system. Therefore, it is plausible that coagulation is the dominant mechanism during the stage when clusters increase their size and this is governed by the promotion of movement of clusters by 'trapped' vacancies.

Zurob and his co-worker [112] proposed another mechanism that the growth rate of the clusters depends on the probability of the vacancies which are previously 'trapped' in the clusters, escaping back to the matrix bringing additional new atoms. The growth rate relationship they have proposed is $N \propto \ln(t)$, where N is the average number of atoms in cluster. The average number of atoms in the clusters with more than 15 atoms is plotted as a function of $\ln(t)$ in Figure 7.2. Linear fitting is then performed. The simulated results also shows an agreement with the relationship, which indicates tha$t$ $N \propto \ln(t)$ can also represent the kinetics of cluster growth on the basis that the trapped cluster escapes during the later stage of NA. However, the mean square error of fitting is 0.99 which is higher than the fitting error for the coagulation model (0.91). Therefore, the coagulation relationship $d \propto t^{0.15}$ is slightly better for describing the mechanism during this stage but the differences are too small to distinguish between the models.

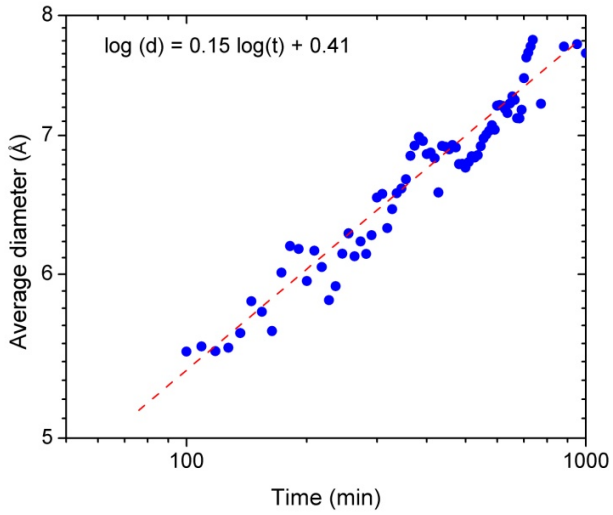

Figure 7.1. Fitting of power law to the average diameter of clusters for bigger clusters after NA for 100 min. The relationship $d \propto t^{0.15}$ *is found.*

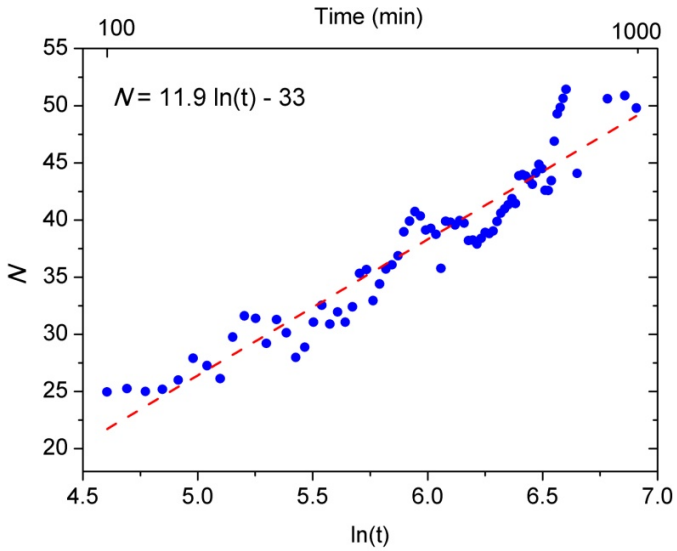

Figure 7.2. Fitting of average number of solutes in clusters with >15 atoms by with data $N \propto \ln(t)$ *from the KMC simulation after NA for 100 min.*

7.1.2. Stages of Clustering during NA

Different clustering stages are found by using different methods and again summarised here. In PALS, 4 stages are observed: Stage 1) $0 < t < 10$ min, a short initial stage of constant average lifetime, Stage 2) $10 < t < 70$ min, the average lifetime continuously decreases, Stage 3) $70 < t <$

400 min, the average lifetime increases, Stage 4) t > 400 min, finally the average lifetime becomes stable.

In hardness, two stages are observed: Stage 1) 10 < t < ~ 20,000 min, hardness increases; Stage 2) t > 20,000 min, no further significant increase in hardness.

In thermal kinetic modelling, mainly two parallel clustering processes are found: 1) 1st clustering process, lower Q_{eff}, lower K_{eff} with higher n, 2) 2nd + 3rd clustering process, higher Q_{eff}, higher K_{eff} with lower n. Using Eq. 6.13, the change of α at T=20 °C is simulated. 1) for 1st clustering process 1 min < t < 100 min; 2) for combined 2nd + 3rd clustering process, 10 < t < ~ 40,000 min.

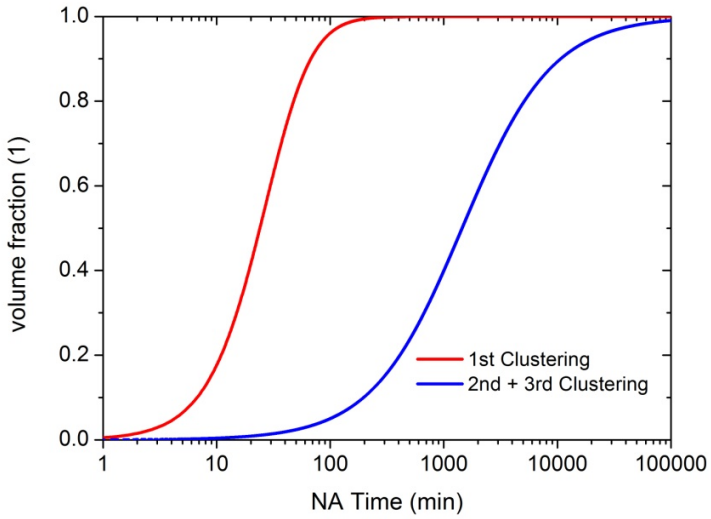

Figure 7.3. The simulated change of α as a function of time t for 1st and combined 2nd + 3rd clustering processes obtained by the kinetic model with the fitted parameters given in Table 6.3 at 20 °C by using Eq. 6.13.

In KMC simulation, 3 stages are categorized: Stage 1) 0 < t < 2 min, fast increase of the number density of the clusters together with the increase of solute fraction in clusters. The size of the clusters is small (< 15 atoms). Vacancies diffuse back to the matrix either to form more clusters or to bring more solutes into the clusters, Stage 2) 2 < t < 10 min, a transition period in which the number density of the clusters decreases with still increasing of solute fraction in the clusters, Stage 3) 10< t < 1000 min, decrease of the number density of clusters with saturated

solute fraction in the clusters. The vacancy is often trapped by clusters and big clusters are formed by coagulation.

One should keep in mind that the time scale obtained in the simulation relates strongly with the concentration of the quenched-in vacancy that enters Eq. 3.7. However, how many vacancies are lost during quenching and NA in a real system is difficult to determine. Vacancy losses would stretch the time axis of the simulation. Time-dependent losses (e.g. by diffusion of permanent sinks) would distort the time axis accordingly. Therefore, the time sections from simulation are difficult to be directly related to the real time scale from the experimental results or DSC modelling. However, when compared with the experimental results, Stage 1 of the KMC simulation is more proper to describe the process before t < 100 min while Stage 3 is for t > 400 min.

The change of the volume fraction α of clustering during NA (T = 20 °C) as a function of time is simulated by introducing c_1 =0.69 and the change of volume fractions α as given in Figure 7.3 to Eq. 6.35. The results are plotted together with the PALS and hardness measurements, see Figure 7.4.

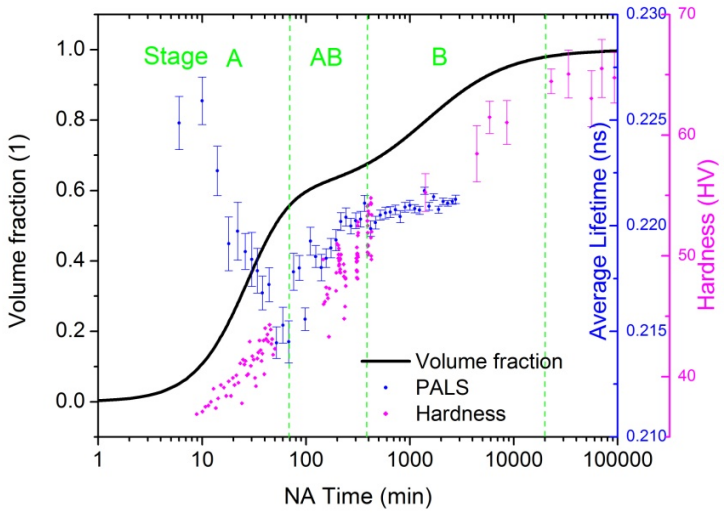

Figure 7.4. The simulated change of α as a function of time t obtained by the kinetic model with the fitted parameters given in Table 6.3 at 20 °C, PALS and hardness results of 4-10 are plotted together for comparison. The green dashed line represents the significant changes of stages during clustering.

A two-step increase of α with different increasing rates is found from the kinetic model. The 1st clustering process develops rapidly after NA for 3 min till 70 min. Then, a transition period from the 1st clustering to the combined 2nd + 3rd clustering processes is found between 70 and 400 min of NA. The combined 2nd + 3rd clustering process almost completes after NA for ~20,000 min. The most prominent feature (Stage 1) of the PALS measurement is the decrease of the average positron lifetime. This happens during 10 to 70 min of NA and coincides with the 1st clustering process. After the decrease, the positron lifetime increases again from ~70 min to ~400 min of NA which corresponds to the transition of the 1st to the 2nd + 3rd process. The increase of the positron lifetime slows down and the lifetime becomes stable after t > 400 min. At the same time, the 2nd + 3rd process continues. In this work only hardness measurements have been performed for longer NA, up to ~100,000 min. Constant hardness values are observed after NA ~20,000 min, thus supporting that the clustering process corresponds to the 2nd + 3rd process is largely completed after NA for ~20,000 min.

Therefore, all the different stages detected, modelled or simulated by different approaches can be summarised as the following two main stages:

Stage A (t < 70 min): First, vacancies diffuse fast and bind with solutes forming vacancy-solute complexes. These vacancy-solute complexes further diffuse to form clusters. More small clusters (< 15 atoms) are formed by vacancies diffusing back to the matrix. The self-diffusion activation energy of vacancies in pure Al which consists of the formation and migration activation term is 120-140 kJ/mol [113]. The formation enthalpy is found to be in the range of 60 - 74 kJ/mol [114], meaning that the migration energy of the vacancy is in between 46 and 80 kJ/mol. The Q_{eff} obtained for the 1st process is 50 kJ/mol, indicating that vacancy migration could be a dominant process at the beginning of clustering, giving a relatively low Q_{eff}. The initial value of the average positron lifetime in both alloys is ~230 ps, see Figure 7.3. This value lies between the lifetime for positron annihilated in fully annealed pure Al (160–170 ps) and vacancy sites (250 ps) that are found in the literature [115]. The prominent feature of lifetime decrease in the first 70 min is believed to be related to formation of Si-rich clusters [48]. KMC simulation that shows during this stage the vacancy spends most of its time in the matrix or with a single solute. The very high fraction (> 0.9) of time for vacancy to change its position with Si indicates a very high mobility of vacancy-Si complex, which makes the diffusion of Si controlling the kinetics of clustering in this

stage. A rapid development of small clusters is also found. The Avrami exponent n = 1.8 indicates that the mechanism is similar to continuous nucleation with some situated nucleation sites, while KMC shows that the system starts with some pre-existing dimers and trimers due to the high solute concentration and performs fast formation of small clusters.

Transition Stage AB (70 < t < 400 min): There is a transition period according to the clustering processes observed by the kinetic model, Figure 7.3. However, it should be noted that the positron lifetime increases again from its minimum. These rapid changes can only be observed in PALS experiment but not by other methods, e.g. in-situ resistivity [48], which shows a gradual change of slope within this time range. The reason for this increase is unclear. However, by comparing alloys with different compositions of Mg and Si, Banhart found that the alloy shows more significant feature of the lifetime increase if more Mg is presented, therefore it is speculated that the increase of the lifetime may be caused by Mg solutes [48].

Stage B (t > 400 min): As the number and size of the clusters increase, vacancies are now trapped by the clusters. The Q_{eff} of the 2nd+3rd clustering process gets higher possibly because when the vacancy is trapped, more energy is needed for the vacancy to change its site. The size of clusters further increases by coagulation, meanwhile the mobility of the clusters increases. Another population of bigger clusters (> 15 atom) develop in the KMC simulation at a later stage of clustering. Relatively small changes in the positron lifetime are found after 400 min of NA, which indicates that, the change of the environment around the vacancy and also the amount of vacancies in the system become stable. The mechanism in this stage is similar to particle growth (n = 1.1), and the process is slow as the process only finishes after NA for several weeks.

7.2. Negative Effect by Clustering

What NA brings to the sample is the negative effect, causing a decrease of the number density of β" and an increase of their length after AA, see Figure 4.13c and 4.16a or Figure 4.13f and 4.16b. Assisted by the quenched-in vacancies, clusters which consist of a small amount of atoms form first during NA and consume a large amount of solutes (~ 58%) according to KMC. The process is fast and largely occurs in the first 70 min of NA. During this period, negative strength response has mostly developed, see Figure 4.15 and 4.23. Most of the clusters formed have the size smaller than ~ 15 solute atoms. Such a small cluster would not have strong thermal

stability and is expected to dissolve during AA. The evidence comes from the DSC curve, Figure 4.11a, that after NA for 100 min, a significant continuous endothermic reaction for dissolution is found. This means that the clusters formed during NA are not stable and dissolve at elevated temperatures. Pashley et al. [7] have shown that there exists a critical size r_c of clusters formed during NA that determine whether clusters will dissolve or further grow during subsequent ageing or not. The average size of the clusters formed before 100 min of NA is expected to be much smaller than the critical size r_c for the clusters that can be survived at the elevated temperatures ($r \ll r_c$). Therefore instead of further growing, perhaps as nucleation sites for β", it is believed that these small clusters dissolve during AA. Another evidence is from the Arami exponent n = 2.5 obtained by the kinetic model for the formation of β" for samples after NA 100 min. The n values are the same for samples with and without NA, which means that continuous nucleation without pre-existing nuclei is the mechanism governing the formation of β". That clusters formed during NA have to dissolve first also implies that the amount of solutes available for the formation of β" is reduced markedly, at least at the beginning of AA when continuous dissolution of clusters and precipitation of β" occur simultaneously.

If the NA time is long enough vacancies will be trapped inside the clusters and the amount of the "free" vacancies available for the formation of β" will decrease, hindering the nucleation process for β". Therefore, fewer β" precipitates are is found in the sample with NA for 100 min, Figure 4.13c and 4.16a. Pogatscher et al. [53] have proposed that after NA for long time, vacancies are bound with co-clusters and are therefore caged in a 'prison' of solute atoms. Hence they have suggested that by AA at T < 210 ^{o}C it is difficult to release vacancies from clusters to assist the diffusion of solute to form precipitates [53]. Also, from this work, trapping of vacancies inside clusters dominates Stage B of clustering, which is after 400 min of NA. Therefore this might be another reason leading to the negative effect. When fewer nuclei of β" are present, the diffusion field for solute transport to the individual β" will be less overlapped, leading to a possibility of larger size of β", see Figure 4.13c and f and Figure 4.16a and b. Also, the solutes which are dissolved from the clusters are now available for further growth of β".

Serizawa et al. explained the negative effect by the thermally stable cluster (1) which forms during NA [11]. Cluster (1) is only associated with the low temperature clustering peak in the DSC run which is identical as the 1st clustering process in this work and considered to be stable

during the successive AA [11]. As shown in Figure 7.3, all the clustering processes corresponding to the cluster peaks can occur at RT. Moreover, the sample with NA shows a continuous dissolution endothermic reaction in the DSC run, see Figure 4.11a. This indicates that the dissolution of formed cluster during NA occurs at the elevated temperature, i.e. temperature for AA. Therefore, their explanation on the negative effect is hardly true.

7.3. Influence of Intermetallics

There are many factors affecting recrystallisation during annealing or SHT, e.g. initial grain size before rolling, rolling microstructures, rolling textures, presence of intermetallics, etc. After cold rolling, intermetallics are found in both of the alloys, Figure 4.3. Despite the fact that Si-rich dispersoids form during the first 2 min of SHT, recrystallisation is more promoted in 4-10X due to the presence of more big intermetallics which could increase recrystallisation events by particle stimulated nucleation (PSN) [116]. The presence of dispersoids will hinder the recrystallisation nuclei to grow out from the dislocation substructures or grain growth anyway by Zener drag in both alloys [117]. However, in 4-10X due to the higher number of recrystallised grains formed already at early SHT times, evidence from Figure 4.2, these grains grow further at a time the dispersoid has already dissolved. Their boundaries touch each other and grain growth will slow down. On the other hand, due to fewer recrystallisation grains which can be formed in 4-10, once the dispersoids are dissolved, these grains can grow to larger size than 4-10X.

After SHT, the Fe-rich intermetallics in 4-10X which have a certain amount of Si retained, see Table 4.1. This lowers the Si concentration in the matrix. As the clustering kinetics is considered to be driven by the diffusion of Si, the rate of clustering is lowered, at least during Stage A. This is revealed by the rate of increase of hardness during NA, figure 4.8. Another reason could be that the boundary of the intermetallics act as vacancy sinks and certain amount of quenched-in vacancies get trapped at the boundary instead of binding with solutes. This lowers the concentration of the quenched-in vacancies in the matrix and hence the rate of clustering. Also, lowering the Si concentration in the matrix means reducing the extent of clustering. From simulation results of another alloy (6-8) which contains 0.67 at.% Mg and 0.77 at.% Si [75], the solute fraction in clusters can be as high as ~70 %, which is even higher than for 4-10. Of course this is related to the interaction energies of Mg and Si which have been put into the simulation. However, from another DSC study on the effect of Mg/Si ratio on clustering [55], we know that

the alloy which has the Mg/Si ratio closest to 1 possesses the largest clustering peak. Hence Mg and Si are both important 'ingredients' for the clusters and therefore the heat effect for clustering in all the Fe and Mn containing alloys should be lowered, which is true and is shown in Figure 4.20b.

The Fe-rich intermetallics are already present after casting [118] and transform into eutectoid after homogenisation [118]. After homogenisation, the Fe-rich intermetallics are spherodised, and dispersoids are formed, mainly during cooling. At this stage, dispersoid-free zone (DFZ) is already formed around the intermetallics. Researchers attributed the reason to the transformation and formation of intermetallics during homogenisation [118]. Anyhow, this DFZ, which is depleted in solutes remains and the alloy then goes through several thermo-mechanical processes before AA. The intermetallics are aligned along the RD and fragmented during rolling, see Figure 4.3, and then the alloy is SHT. Still this DFZ remains and are clearly shows in Figure 4.4. Therefore, this leads to the presence of PFZ around the intermetallics, see Figure 4.14.

The value of K_{eff} for β" formation is lower in the presence of intermetallics. Similar to the case of clustering, this is related to the lowering of Si concentration in the matrix, which lowers the reaction frequency of β" and leads to a reduction of the volume fraction of the precipitates, see Table 4.3. On the other hand, the presence of intermetallics lowers the value of Q_{eff} for the formation of β". As it has been mentioned above, the presence of Fe and Mn promotes the formation of intermetallics after homogenisation. These intermetallics transform and deform through the thermo-mechanical processes and in the end increases the fluctuation of the solute content in the matrix. It can be seen clearly in Figure 4.4 that the dispersoids formed during SHT are not homogenously distributed and when they then dissolved, a non-uniform solute concentration throughout the alloy is expected. This fluctuation increases the diffusion gradient of the solutes which would lower the activation energy for the formation of β".

7.4. Effect of Trace Elements (Cr and Cu)

No significant effect of Cr on clustering in the pure ternary alloy is found, while the presence of Cu lowers the 1st clustering peak, see Figure 4.20b. Assuming that Cu remains as solute in the matrix, as Cu and a vacancy have attractive binding [77, 79], they would possibly bind together and lower the number of vacancy-Si complexes, therefore, slow down the clustering kinetics and

in the end lower the amount of clusters formed. This would reduce the negative effect caused by NA, as revealed by Figure 4.23b. From the DSC and hardness results, Figures 4.19a and 4.21a, Cr shows no significant effect on the kinetics of precipitate formation. However, from DSC, the presence of Cu reduces the magnitude of the β" formation peak, but increases the magnitude of the formation peaks in the temperature range of the formation peak of β'. In alloys containing more of Cu [33, 119], Q' or L' phases are found in the peak-aged condition. TEM has been performed on the Cu-containing alloy at peak-aged condition, see Figure 4.19, but no Q' or L' phases can be found. Either volume fraction is too small or they form at higher temperatures during AA.

When Fe is present in the base alloy (4-10X group), both Cr and Cu increase the heat effect of clustering, Figure 4.20b. The intermetallics found in Cr and Cu-containing alloys are finer and the Si content is lower compared to 4-10X, see Table 4.4. Therefore, intermetallics are easier to break down and to dissolve during SHT, providing more Si in the matrix for further NA or AA. Still, the Cu solutes which remain in the matrix hinder the clustering process and therefore a higher heat effect is found in 4-10XCr than in 4-10XCu. Faster hardening response and higher peak hardness are also found in 4-10XCr and 4-10XCu than in 4-10X, see Figure 4.21. Comparing Figure 4.13f to 4.22c and d, a higher number density but smaller precipitates in 4-10XCr and 4-10XCu than in 4-10X are observed. Correspondingly, an earlier formation peak of β" with a larger heat effect is observed in 4-10XCr and 4-10XCu, see Figure 4.19. By using the same kinetic model introduced in Chapter 6, the kinetic parameters for 4-10XCr and 4-10XCu are obtained and their values are given in Table 7.6.

Table 7.6. The kinetic parameters for the formation of β".

Sample	Q_{eff} (kJ/mol)	K_{eff} (s^{-1})	n
4-10XCr	88	2.8×10^{6}	2.5
4-10XCu	90	3.1×10^{6}	2.5

Higher Q_{eff} and K_{eff} values are obtained in 4-10XCr and 4-10Cu as compared to those found in 4-10X, see Table 6.4. This confirms that a higher number density but smaller size of the precipitates is associated to higher Q_{eff} and K_{eff}. Furthermore, higher Q_{eff} and K_{eff} lead to

faster kinetics in 4-10 compared to 4-10X, as shown by the evolution of hardness during AA, see Figure 4.21. The kinetic parameters found in the 4-10X group are all in the same magnitude. Therefore, Cr and Cu show an indirect effect on clustering and precipitation when intermetallics are present. They refine the intermetllics and lower the Si concentration in the Fe-rich intermetallics so that a higher concentration of Si is available in the matrix for further clustering and precipitation.

8. Conclusions

The mechanism and kinetics of clustering and precipitation in 6xxx series alloys have been studied and the relationship between clustering and precipitation, including the influence by other elements has been investigated.

The main findings are:

1) During SHT, 6xxx series alloys undergo recrystallisation and precipitation of Si-rich precipitates within a short SHT time. Afterwards, dissolution of previously formed precipitates as well as grain growth occurs simultaneously. The SSSS stage can only be obtained after SHT at 540 ^{o}C for at least 5 min.

2) Two main processes occur during clustering at RT. During the first, solutes diffuse fast mediated by quenched-in vacancies and form small clusters. As the solute concentration in the matrix is reduced, vacancies are increasingly trapped by the clusters. This process has a low effective activation energy Q_{eff} and shows a fast kinetics, which usually finishes within the first 70 min of NA. An Avrami exponent n = 1.8 indicates that the mechanism is similar to continuous nucleation with pre-existing nuclei. During the second process, bigger clusters are formed by coagulation of existing clusters. A higher effective activation energy Q_{eff} is obtained with an Avrami exponent n = 1.1, which indicates that the mechanism is similar to particle growth.

3) When NA is performed before AA, the number density of the precipitates formed during AA decreases while their size increases. This correlates with the lower value for the constant K_{eff} that is obtained by the thermal kinetic model and, in consequence, slows down the kinetics of β" formation.

4) The negative strength response during AA develops within the first 70 min of NA, for which the first clustering process is held responsible. Therefore, the main source of the negative effect is the formation of smaller clusters which lower the solute concentration in the matrix and capture the vacancies.

5) The presence of intermetallics stimulates recrystallisation and, in the end, finer grains can be obtained after SHT. However, the Fe-rich intermetallics cannot be dissolved completely during SHT and lower the Si concentration in the matrix. This reduces the volume fraction of both clusters and precipitates. Therefore, a lower number density of longer precipitates is found in the

Fe and Mn-containing alloy 4-10X. This corresponds to lower Q_{eff} and K_{eff} values obtained for the formation of β".

6) When 0.04 wt.% Cu is added to the pure ternary alloy, the 1st clustering process is impaired and the alloy has less negative strength response. The precipitation sequence is also affected, in which more heat released in a wide temperature range is observed after β" formation. The increased heat released is associated to the formation of Q' or L'. The magnitude of the formation of β" is also lowered. No notable influence of an addition of 0.01 wt.% Cr is found for both clustering and precipitation in pure ternary alloy.

Cr and Cu are found to be present in α-Al(Fe, Mn)Si intermetallics and the Si content in the intermetallics is reduced. Therefore, more clusters form during NA, while a higher number density of shorter precipitates is found during AA. The morphology of the precipitates is associated with higher Q_{eff} and K_{eff} values for the formation of β".

References

1 L.F. Mondolfo, *Aluminium Alloys: Structure and properties*, Butterworths, London, 1976.

2 C. Feneau, *Non-ferrous metals from Ag to Zn*, Umicore, Belgium, 2002.

3 J.E. Hatch, *Aluminium: properties and physical metallurgy*, American Society for Metals, Metals Park, Ohio, 1984.

4 J. Hirsch, *Automotive trends in aluminium - The European Perspective*, ICAA9, edited by .J.F.Nie, A.J.Morton, .C.Muddle, Materials Forum 28, 1 (2004), pp. 15-23.

5 J. Hirsch, *Aluminium Alloy for Automotive Application*, Materials Science Forum, 242 (1997), pp. 33-50.

6 I. Kovács, J. Lendvai, E. Nagy, *The mechanism of clustering in supersaturated solid solutions of Al-Mg2Si alloys,* Acta Metallurgica, 20 (1972), pp. 975-983.

7 D. W. Pashley, M. H. Jacobs, J. T. Vietz, *The basic processes affecting two-step ageing in an Al-Mg-Si alloy*, Philosophical Magazine, 16 (1967), pp. 51-76.

8 Y. Birol, *Pre-aging to improve bake hardening in a twin-roll cast Al–Mg–Si alloy*, Materials Science and Engineering A, 391 (2005), pp. 175–180.

9 M. Saga, Y. Sasaki, M. Kikuchi, Z. Yan, M. Matsuo, *Effect of pre-aging temperature on the behavior in the early stage of aging at high temperature for Al-Mg-Si alloy*, Material Science Forum, 217-222 (1996), pp. 821-826.

10 M. Murayama, K. Hono, *Pre-precipitate clusters and precipitation processes in Al–Mg–Si alloys*, Acta Materialia, 47 (1999), pp. 1537-1548.

11 A. Serizawa, S. Hirosawa, T.Sato, *Three-dimensional atom probe characterization of nanoclusters responsible for multistep aging behavior of an Al-Mg-Si alloy*, Metallurgical and Materials Transactions A, 39 (2008), pp. 243-251.

12 M. Torsæter, H.S. Hasting, W. Lefebvre, C.D. Marioara, J.C. Walmsley, S.J. Andersen, R. Holmestad*, The influence of composition and natural aging on clustering during preageing in Al-Mg-Si alloys*, Journal of Applied Physics, 108 (2010), 073527.

13 T. Abid, A. Boubertakh, S. Hamamda, *Effect of pre-aging and maturing on the precipitation hardening of an Al–Mg–Si alloy*, Journal of Alloys and Compounds, 490(2010), pp. 166-169.

14 A.K. Gupta, D.J. Lloyd, *Study of precipitation kinetics in a super purity Al-0.8 Pct Mg-0.9 Pct Si alloy using Differential Scanning Calorimetry*, Metallurgical and Materials Transactions A, 13 (1999), pp. 879-884.

15 A. K. Gupta , D. J. Lloyd, S. A. Court, *Precipitation hardening processes in an Al–0.4%Mg–1.3%Si–0.25%Fe aluminum alloy*, Materials Science and Engineering A, 301 (2001), pp. 140-146.

16 L. Zhen, W. D. Fei, S. B. Kang, H. W. Kim, *Precipitation behaviour of Al – Mg – Si alloys with high silicon content*, Journal of Materials Science, 32 (1997), pp. 1895-1907.

17 J. L. Cavazos, C. Rafael, *Precipitation in a heat-treatable aluminum alloy cooled at different rates*, Materials Characterization, 47 (2001), pp. 175-179.

18 K. Matsuda, T. Kawabata, Y. Uetani, T. Sato, A. Kamio, S. Ikeno, *HRTEM observation of G.P. zones and metastable phase in Al-Mg-Si alloys,* Materials Science Forum, 331-337 (2000), pp. 989-994.

19 C.D. Marioara, S.J. Andersen, J. Jansen, H.W. Zandbergen, *The influence of temperature and storage time at RT on nucleation of the β″ phase in a 6082 Al–Mg–Si alloy*, Acta Materialia, 51 (2003), pp. 789-796.

20 S.J. Andersen, H.W. Zandbergen, J. Jansen, U. Tundal, O. Reiso, *The crystal structure of the β″ phase in Al – Mg – Si alloys*, Acta Metallurgica, 46 (1998), pp. 3283-3298.

21 K. Matsuda, T. Naoi, K. Fujii, Y. Uetani, *Crystal structure of the β″ phase in an Al–l.0mass%Mg2Si–0.4mass%Si alloy*, Materials Science and Engineering A, 262 (1999), pp. 232-237.

22 S.J. Andersen, C D. Marioara, M Torsæter, R Bjørge, F.J.H Ehlers, R Holmestad, O. Reiso, J. Røyset, *Behind structure and relation of precipitates in Al-Mg-Si and related alloys*, Proceeding Proceedings of the 12th International Conference on Aluminium Alloys, September 5-9, 2010, Yokohama, Japan Aluminium Alloys, 2010, pp. 413-419.

23 J.P. Lynch, L.M. Brown, M.H. Jacobs, *Microanalysis of Age-hardening Precipitates in Aluminium Alloys*, Acta Metallurgica, 30 (1982), pp. 1389-1395.

24 F. De Geuser, W. Lefebvre, D. Blavette, *3D atom probe study of solute atoms clustering during natural ageing and pre-ageing of an Al-Mg-Si alloy*, Philosophical Magazine Letters, 86 (2006), pp. 227-234.

25 H.S. Hasting, A.G. Froseth, S.J. Andersen, R. Vissers, J.C. Walmsley, C. D. Marioara, F. Danoix, W. Lefebvre, R. Holmestad, *Composition of β″ precipitates in Al–Mg–Si alloys by atom probe tomography and first principles calculations*, Journal of Applied Physics, 106 (2009), pp. 12571-9.

References

26 M. H. Jacobs, *The structure of the metastable precipitates formed during ageing of an Al-Mg-Si alloy*, Philosophical Magazine, 26 (1972), pp. 1-3.

27 C.D. Marioara, H. Nordmark, S.J. Andersen, R. Holmestad, *Post-beta" phases and their influence on microstructure and hardness in 6xxx Al-Mg-Si alloys*, Journal of Materials Science, 41 (2006), pp. 471-478.

28 N. Maruyama, R. Uemori, N. Hashimoto, M. Saga, M. Kikuchi, *Effect of silicon addition on the composition structure of fine-scale precipitates in Al-Mg-Si alloys*, Acta Metallurgica, 36 (1997), pp. 89-93.

29 K. Matsuda, H. Gamada, K. Fujii, Y. Uetani, T. Sato, A. Kamio, S. Ikeno, *High-Resolution Electron microscopy on the structure of Gunier-Piston Zones in an Al-1.6 Mass Mg2Si alloy*, Metallurgical and Materials Transactions A, 29 (1998), pp. 1161-1167.

30 I. Dutta, S.M. Allen, J.L. Hafley, *Effect of reinforcement on the aging response of cast 6061 Al-Al_2O_3 particulate composites*, Metallurgical and Materials Transactions A, 22 (1991), pp. 2553-2563.

31 G. Edwards, K. Stiller, G. Dunlop and M. Couoper, *The precipitation sequence in Al-Mg-Si alloys*, Acta Materialia, 46 (1998), pp. 3893-3904.

32 S. Anderson, C. Marioara, A. FrØseth, R. Visser, H. W. Zandbergen, *Crystal structure of the orthorhombic U2-Al4Mg4Si4 precipitate in the Al－Mg－Si alloy system and its relation to the β′ and β" phases*, Materials Science and Engineering A, 390 (2005), pp. 127-138.

33 S. Esmaeili, X. Wang, D.J. Lloyd, W.J. Poole, *On the precipitation-hardening behavior of the Al-Mg-Si-Cu Alloy AA6111*, Metallurgical and Materials Transactions A, 34 (2003), pp. 751-763.

34 W.F. Miao, *D.E. Laughlin, Precipitation hardening in aluminum alloy 6022*, Scripta Materialia, 40(1999), pp. 873-878.

35 A. Gaber, M.A. Gaffar, M.S. Mostafa, E.F.A. Zeid, *Precipitation kinetics of Al–1.12 Mg2Si–0.35 Si and Al–1.07 Mg2Si–0.33 Cu alloys*, Journal of Alloys and Compounds, 429 (2007), pp. 167-175.

36 W.F. Miao, D.E. Laughlin, *Effects of Cu content and preaging on precipitation characteristics in aluminum alloy 6022*, Metallurgical and Materials Transactions A, 31 (2000), pp. 361-371.

37 M. Murayama, K. Hono, W.F. Miao, D.E. Laughlin, *The effect of Cu additions on the precipitation kinetics in an Al-Mg-Si alloy with excess Si*, Metallurgical and Materials Transactions A, 32 (2001), pp. 239-246.

38 C.D. Marioara, S. J. Andersen, T. N. Stene, H. Hasting, J. Walmsley, A.T.J. Van Helvoort, R. Holmestad, *The effect of Cu on precipitation in Al–Mg–Si alloys*, Philosophical Magazine, 87 (2007), pp. 3385-3413.

39 K. Matsuda, Y. Uetani, T. Sato, S. Ikeno, *Metastable phases in an Al-Mg-Si alloy containing copper*, Metallurgical and Materials Transactions A, 32(2001), pp. 1293-1299.

40 J. Banhart, C.S.T. Chang, Z. Liang, N. Wanderka, M.D.H. Lay, A.J. Hill, *Natural ageing in Al-Mg-Si alloy- A process of unexpected complexity*, Advanced Engineering Materials, 12 (2010), pp. 559-571.

41 J. Røyset, T. Stene, J.A. Sæter, O. Reiso, *The effect of intermediate storage temperature and time on the age hardening response of Al-Mg-Si alloys*, Materials Science Forum, 519 (2006), pp. 239-244.

42 H. Seyedrezai, D. Grebennikov, P. Mascher, H. S. Zurob, *Study of the early stages of clustering in Al–Mg–Si alloys using the electrical resistivity measurements*, Materials Science and Engineering A, 525 (2009), pp. 186-191.

43 S. Ceresara, E. Di Russo, P. Fiorini, A. Giarda, *Effect of Si excess on the ageing behaviour of Al-Mg_2Si 0.8% Alloy*, Materials Science and Engineering, 70 (1969), pp. 220-227.

44 C.S.T Chang and J. Banhart, *Low-temperature differential scanning calorimetry of an Al-Mg-Si alloy,* Metallurgical and Materials Transactions A 42 (2011), pp. 1960-1964.

45 J. Kim, E. Kobayashi, T. Sato, *Effect of Cu addtion on behavior of nanoclusters during multi-step aging in Al-Mg-Si alloys*, Materials Transcation, 52 (2011), pp. 906-913.

46 R. Krause, G. Dlubeck, O. Bruemmer, S. Skladnikiewitz, H. Daut, *Nucleation and precipitation in an Al-Si (1 at. %) alloy investigated by Positron Annihilation*, Crystal Research and Technology, 20 (1985), pp. 267-269.

47 H. Seyedrezai, *Early stages of ageing in Al-Mg-Si alloys*, Master thesis, McMaster University, 2007.

48 J Banhart, M D H Lay, C S T Chang, A J Hill, *The kinetics of natural ageing in Al-Mg-Si alloys by positron annihilation lifetime spectroscopy*, Physical Review B, 83 (2010), pp. 1-13.

49 A. Cerezo, P.H. Clifton, S. Lozano-Perez, P. Sergio, P. Panayi, G. Sha, G.D.W Smith, *Overview: Recent progress in three-dimensional atom probe instruments and applications*, Microscopy and microanalysis, 13 (2007), pp. 408-417.

50 D. Vaumousse, A. Cerezo, P.J. Warren, *A procedure for quantification of precipitate microstructures from three-dimensional atom probe data*, Ultramicroscopy, 95 (2003), pp. 215-221.

References

51 M. Torsæter, *Quantitative Studies of Clustering and Precipitation in Al-Mg-Si(Cu) alloys*, Doctoral thesis, NTNU, 2011:212.

52 Z. Liang, *Investigation on the Precipitation of Al-Mg-Si alloys with Different Heat Treatments*, Master thesis, South China University of Technology, 2009.

53 S. Pogatscher, H. Antrekowitsch, H. Leitner, T. Ebner, P.J Uggowitzer, *Mechanisms controlling the artificial aging of Al–Mg–Si Alloys*, Acta Materialia, 59 (2011), pp. 3352-3363.

54 M. E. BROWN. *Handbook of Thermal Analysis and Calormetry*, Elsevier, Amsterdam, 2008.

55 C.S.T Chang, Z. Liang, E. Schmidt, J. Banhart, *Influence of Mg/Si ratio on the clustering kinetics in Al—Mg—Si alloys,* International Journal of Materials Research, accepted.

56 K. Binder, *Theory for the dynamic of "cluster" II, Critical diffusion in binary systems and the kinetics of phase separation*, Physical Review B, 15 (1977), pp. 4425-4447.

57 K. Binder, D. Stauffer, H. Mueller-Krumbhaar, *Calculation of dynamic critical properties from a cluster-reaction theory*, Physical Review B, 10 (1974), pp. 3853-3857.

58 K. Binder, D. Stauffer, *Theory for the slowing down of the relaxation and spinodal decomposition of binary mixtures*, Physical Review Letters, 33 (1974), pp.1006-1009.

59 E. Clouet, C. Hin, D. Gendt, M. Nastar, F. Soisson, *Kinetic Monte Carlo Simulations of Precipitation*, Advanced Engineering Materials, 8 (2006), pp.1210-1214.

60 S. Hirosawa, T. Sato, *Monte Carlo computer simulation of the atomistic behaviour of microalloying elements in Al – Li alloys*, Modelling and Simulation in Materials Science and Engineering, 9 (2001), pp.129-141.

61 S. Hirosawa, T. Sato, J. Yokota, A. Kamio, *Comparison between resistivity changes and Monte Carlo simulation for GP zone formation in Al-Cu base ternary alloys*, Materials Transactions, JIM, 39 (1998), pp. 139-146.

62 G. Sha, A. Cerezo, *Kinetic Monte Carlo simulation of clustering in an Al-Zn-Mg-Cu alloy(7050)*, Acta Materialia, 53 (2005), pp.907-917.

63 L.C Doan, Y. Ohmori, K. Nakai, *Precipitation and dissolution reaction in a 6061 aluminum alloy*, Material Transactions, JIM, 41 (2000), pp. 300-305.

64 A. Gaber, A.M. Ali, K. Matsuda, T. Kawabata, T. Yamazaki, S. Ikeno, *Study of the developed precipitates in Al-0.63Mg-0.37Si-0.5Cu (wt.%) alloy by using DSC and TEM techniques*, Journal of Alloys and Compounds, 432 (2007), pp. 149-155.

65 A. Gaber, N. Afify, M. S. Mostafa, G. Abbady, *Effect of heat treatment on the precipitation in Al–1at.% Mg–xat.% Si (x=0.6, 1.0 and 1.6) alloys*, Journal of Alloys and Compounds, 477 (2009), pp. 295-300.

66 K. Matsuda, H. Gamada, K. Fujii, Y. Uetani, T. Sato, A. Kamio, S. Ikeno, *High-Resolution Electron Microscopy on the Structure of Guinier-Preston Zones in an Al-1.6 Mass Pct Mg2Si* Alloy, Materials Transactions A, 29A (1998), pp. 1161-1167.

67 N.Afify, A.Gaber, M.S. Mostafa, G. Abbady, *Influence of Si concentration on the precipitation in Al-1at.% Mg alloy*, Journal of Alloys and Compounds, 462 (2008), pp. 80-87.

68 I. Dutta, D.L. Bourell, *Influence of dislocation density and distribution on the aging behaviour of 6061 Al-SiC_w composites*, Acta Metallurgica et Materialia, 38 (1990), pp.2041-2049.

69 A. Borrego, G. Gonzalez-Doncel, *Calorimetric study of 6016-Al–15 vol.% SiC_w PM composites extruded at different temperatures*, Materials Science and Engineering A, 245 (1998), pp. 10-18.

70 M.J. Starink, *Comments on: 'Calorimetric study of 6016-Al–15 vol.% SiCw PM composites extruded at different temperatures, Mater'. Sci. Eng. A 245 (1998) 10,* Materials Science and Engineering A, 276 (2000), pp. 288-291.

71 A. Borrego, G. Gonzalez-Doncel, *Reply to comments on: 'Calorimetric study of 6016-Al–15 vol.% SiCw PM composites extruded at different temperatures' by A. Borrego, G. Gonzalez-Doncel, Mater. Sci. Eng. A 245 (1998) 10'*, Materials Science and Engineering A, 276 (2000), pp. 292-295.

72 J. Kansy, *Microcomputer Program for Analysis of Positron Annihilation Lifetime Spectra*, Nuclear Instruments and Methods in Physics Research Section A: Accelerators, Spectrometers, Detectors and Associated Equipment, 374 (1996), pp. 235.

73 D. Brandon, W.D. Kaplan, *Microstructural Characterization of Materials*, Wiley 2nd edition, UK, 1984.

74 C.D. Marioara, S.J. Andersen, H.W. Zandbergen, R. Holmestad, *The influence of alloy composition on precipitates of the Al-Mg-Si system*, Metallurgical and Materials Transactions A, 36 (2005), pp. 691-702.

75 Z. Liang, C.S.T Chang, C. Abromeit, J. Banhart, J. Hirsch, *The kinetics of clustering in Al–Mg–Si alloys studied by Monte Carlo simulation*, International Journal of Materials Research, accepted.

76 M. Mantina, Y. Yang, L.Q. Chen, Z.K. Liu, C. Wolverton, *First principles impurity diffusion coefficients*, Acta Materialia, 57 (2009), pp. 4102-4108.

References

77 S. Hirosawa, F. Nakamura, T. Sato, *First-principle calculation of interaction energies between solutes and/or vacancies for predicting atomistic behaviors of microalloying elements in aluminium alloys*, Materials Science Forum, 283 (2007), pp. 561-565.

78 T. Hoshino, R. Zeller, P.H. Dederichs, *Local-density-functional calculations for defect interactions in Al. Physical review B Condensed matter*, 53 (1996), pp. 8971-8974.

79 S. Hirosawa, F. Nakamura, T. Sato, T. Hoshino, *First-principles calculation of interaction energies between solutes and/or vacancies and the prediction of atomistic behaviors of microalloying elements in aluminium alloys*, Journal of Japan Institute of Light Metals, 56 (2006), pp. 621-628.

80 E. Clouet, C. Hin, D. Gendt, M. Nastar, F. Soisson. *Kinetic Monte Carlo Simulations of precipitation*, Advanced Engineering Materials, 8 (2006), pp. 1210-1214.

81 K.M. Carling, G. Wahnström, T.R. Mattsson, N. Sandberg, G. Grimvall, *Vacancy concentration in Al from combined first-principles in model potential calculations*, Physical Review B, 67 (2003), 054101.

82 P. Erhart, P. Jung, H. Schult, H. Ullmaier, in Atomic Defects in Metals, Springer-Verlag, Berlin, 1991.

83 M. Matsumoto, T. Nishimura, Mersenne Twister: *A 623-dimensionally equidistributed uniform pseudo-random number generator*, ACM Transactions on Modeling and Computer Simulation, 8 (1998), pp. 3-30.

84 F. Lasagni, A. Lasagni, C. Holzapfel, M. Engstler, F. Muecklich, *3D microstructural study of AlSi8Mg5 alloy by FIB-Tomography*, Practical Metallography, 47 (2010), pp. 487-499.

85 Y.L. Liu, S.B. Kang, *The solidification process of Al-Mg-Si alloys*, Journal of Materials Science 22 (1997), pp. 1443-1447.

86 M.J. Couper, B. Rinderer, J.Y. Yao, *Characterisation of AlFeSi intermetallics in 6000 series aluminium alloy extrusions*, Materials Science Forum, 519-521 (2009), pp. 303-308.

87 K. Momma, F. Izumi, *VESTA: a three-dimensional visualization system for electronic and structural analysis*, Journal of Applied Crystallography, 41 (2008), pp. 653.

88 C. Wolverton, *Solute-vacancy binding in aluminium*, Acta Materialia, 55 (2007), pp. 5867-5872.

89 G.A. Edwards, M.J. Couper, and G.L. Dunlop, in *Aluminum alloys: Their physical and mechanical properties*, ICAA4, T.H. Sanders, Jr.and E.A. Starke, Jr., The Georgia Institute of Technology, Atlanta, GA (1994), pp. 620-627.

90 L. Zhen, W.D. Fei, S.B. Kang, H.W. Kim, *Precipitation behaviour of Al-Mg-Si alloys with high silicon content*, Journal of Materials Science, 32 (1997), pp. 1895-902.

91 M. J. Starink. *Analysis of aluminium based alloys by calorimetry: quantitative analysis of reactions and reaction kinetics*, International Materials Reviews, 49 (2004), pp. 191-226.

92 S. Vyazovkin, C.A. Wight, *Isothermal and non-isothermal kinetics of thermally stimulated reactions of solids*, International Reviews in Physical Chemistry, 17 (1998), pp. 407-433.

93 P. Budrugeac, E. Segal, *Some methodological problems concerning nonisothermal kinetic analysis of heterogeneous solid-gas reactions*, International Journal of Chemical Kinetics, 33 (2001), pp. 564-573.

94 M. J. Starink, *The determination of activation energy from linear heating rate experiments: a comparison of the accuracy of isoconversion methods*, Thermochimica Acta, 401 (2003), pp. 163-176.

95 G.O. Piloyan, D. Ryabchikov, O.S. Novikova, *Determination of activation energies of chemical reactions by differential thermal analysis*, Nature, 212 (1966), pp. 1229.

96 S.V. Vyazovkin, A. I. Lesnikovich, *An approach to the solution of the inverse kinetics problem in the case of complex processes. Part 1. Methods employing a series of thermoanalytical curves*", Thermochimica Acta, 165(1990), pp. 273-280.

97 A. K. Jena, A. K. Kupta, M. C. Chaturvedi, *A differential scanning calorimetric investigation of precipitation kinetics in the Al-1.53 wt% Cu-0.79 wt% Mg alloy*, Acta Metallurgica, 37 (1989), pp. 885-895.

98 M. J. Starink, A. M. Zahra, *Determination of the transformation exponent s from experiments at constant heating rate*, Thermochimica Acta 298(1997), pp. 179-189.

99 J. W. Christian, *The theory of transformation in metals and alloys*, Pergamon Press, Oxford, 2002.

100 F. Liu, C. Sommer, C. Bos, E. J. Mittemeijer, *Analysis of solid state phase transformation kinetics: models and recipes*, International Materials Reviews, 52 (2007), pp. 193-212.

101 F. Liu, F. Sommer, E.J. Mittemeijer, *An analytical model for isothermal and isochronal transformation kinetics*, Journal of Materials Science, 39 (2004), pp. 1621-1634.

102 E. Woldt, *The relationship between isothermal and non-isothermal description of Johnson-Mehl-Avrami-Kolmogorov kinetics*, Journal of Physics and Chemistry of Solids, 53 (1992), pp. 521-527.

References

103 P. Krüger, *On the relationship between non-isothermal and isothermal Kolmogorov-Johnson-Mehl-Avrami crystallization kinetics*, Journal of Physics and Chemistry of Solids, 54 (1993), pp. 1549-1555.

104 M. J. Starink, *On the meaning of the impingement parameter in kinetics equations for nucleation and growth reactions*, Journal of Materials Science, 36 (2001), pp. 4433-4441.

105 T. Ozawa, *Kinetic analysis of derivative curves in thermal analysis, Journal of Thermal Analysis*, 2 (1970), pp. 301-304.

106 S.V. Vyazovkin, V.I. Goryachko, A.I. Lesnikovich, *An approach to the solution of the inverse kinetic problem in the case of complex process. Part III. Parallel independent reactions*, Thermochimica Acta,197 (1992), pp 41-51.

107 M.J. Starink, A.-M. Zahra, *Kinetics of isothermal and non-isothermal precipitation in an Al-6 at.% Si alloy*, Philosophical Magazine A, 77 (2009), pp. 197-199.

108 M.J. Starink, A.-M. Zahra, *Mechanism of combined GP zone and θ' precipitation in an Al-Cu alloy*, Journal of Materials Science Letter, 16 (1997), pp. 1613-1615.

109 M.J. Starink, N. Gao, L. Davin, J. Yan, A. Cerezo, *Room temperature precipitation in quenched Al-Cu-Mg alloys: a model for the reaction kinetics and yield strength development*, Philosophical Magazine, 85 (2005), pp. 1395-1417.

110 A. Girifalco, H. Herman, *A model for the growth of Guinier-Preston Zones- The vacancy pump*, Acta Metallurgica, 13 (1965), pp. 583-590.

111 P. Fratzl, O. Penrose, *Competing mechanisms for precipitate coarsening in phase separation with vacancy dynamics*, Physical Review B, 55 (1997), pp. 6101-6104.

112 H.S. Zurob, H. Seyedrezai, *A model for the growth of solute clusters based on vacancy trapping*, Scripta Materialia, 61 (2009), pp. 141-144.

113 H. Mehrer, N. Stolica, and N. A. Solwijk, *In diffusion in solid Metals and Alloys*, Landolt-Bornstein, New Series, Group III, 26, Springer, Berlin, 1990.

114 H.Wollenberger, *Physical Metallurgy*, edited by R. W. Cahn and P. Haasen , North-Holland, Amsterdam, 1983.

115 A. Seeger and F. Banhart, *On the Systematics of Positron Lifetimes in Metals*, Physica Status Solidi (a) A, 102(1987), pp. 171.

116 F.J. Humphreys, D.J. Jensen, *Structure and texture evolution during recrystallization of particle containing materials,* Proceedings of the 7th Risø International Symposium, 1986, pp. 93-106.

117 F J Humphreys, M. Hatherly, Recrystallization and related annealing phenomena, Elsevier, Oxford, UK, 2004.

118 L. Lodgaard, Nils Ryum, *Precipitation of dispersoids containing Mn and/or Cr in Al-Mg-Si alloys*, Materials Science and Engineering, A283 (2000), pp. 144-152.

119 M. Torsæter, W. Lefebvre, C.D. Maioara, S.J. Andersen, J.C. Walmsley, R. Holmestad, *Study of intergrown L and Q' precipitates in Al-Mg-Si-Cu alloys*, Scripta Materialia, 64 (2011), pp. 817-820.